Understanding the Elevated Temperature Properties of Niobium-Based Alloys Relevant to Aerospace Applications

---

A Thesis

Presented to

The Faculty of the School of Engineering and Applied Science

University of Virginia

In Partial Fulfillment

Of the Requirements for the Degree of

Master of Science (Materials Science and Engineering)

By

Lauren S. Bowling

May 2023

Distribution Statement A

Distribution Statement A

Approval Sheet

This Thesis

is Submitted In Partial Fulfillment

Of the Requirements for the Degree of

Master of Science (Materials Science and Engineering)

Author: Lauren S. Bowling

This Thesis has been read and approved by the examining committee:

Advisor: Dr. Sean Agnew

Committee Member: Dr. Elizabeth Opila

Committee Member: Dr. Haydn Wadley

Committee Member: Dr. Patrick Hopkins

Accepted for the School of Engineering and Applied Science:

Jennifer L. West, School of Engineering and Applied Science

May 2023

Distribution Statement A

Abstract

There is renewed interest in refractory alloys that possess higher service temperatures than incumbent Ni-based superalloys (e.g., ≳1100°C). The focus of this thesis can be divided into two distinct sections, with the first section providing a review of the high-temperature constitutive responses of Nb-alloys measured over a wide range of temperatures (≈860°C < T < ≈1760°C) and strain rates ($\approx 10^{-9}$ $s^{-1} < \dot{\varepsilon} < \approx 10^{-1}$ s^{-1}). Nevertheless, the extant data is sparse and informed materials selection decisions require constitutive expressions to interpolate and reliably extrapolate. The Larson-Miller parameter approach to describe creep-life provides a conservative estimate of material response at the highest temperatures and lowest strain rates, whereas the Sellars-Tegart model describes both steady-state creep and high-temperature tensile test data with a single, universal equation. A minimum flow stress based on the combination of these two models is proposed for design considerations to address the overprediction of strength that can arise from applying one or the other independently. This effort highlights the fact that refractory alloys exhibit strain rate sensitive flow strengths in the temperature range of interest for applications. The roles of alloying, thermomechanical processing, and impurity levels are discussed, and highlight the fact that these advanced Nb-alloys evidence Class 1 (Class A) solute drag controlled creep behavior, except the carbide precipitation strengthened alloy, D-43. In addition, the high-temperature strengths are confirmed to be strongly correlated with alloy melting point.

The second section of this thesis provides available thermophysical property data for a number of Nb-alloys and demonstrates their use within a performance index such that informed materials selection decisions can be made. Comparisons with Ni-superalloys and other refractory-metal based alloys give context for the provided design data. Physically based models are provided that describe the temperature dependencies of the Young's modulus, coefficient of thermal expansion and density, thermal conductivity, and specific heat capacity. The results highlight some critical uncertainties and gaps in existing experimental data in the literature. New data are provided for two Hf-containing alloys. Elastic modulus, thermal expansion, thermal conductivity, and heat capacity are presented for one of the only currently available commercial Nb-alloys, C103 (Nb-10Hf-1Ti wt%), and new thermal conductivity data is provided for the higher strength Nb-alloy, WC-3009 (Nb-30Hf-9W wt%), which has yet to be fully commercialized. A performance index for ranking materials for use in lightweight panel-shaped applications subjected to sharp thermal transients or steep thermal gradients is employed to demonstrate the utility of the data. The results highlight the relative value of current alloy C103, comparisons to WC-3009, as well as the promise of specific Nb-W-Zr alloys.

Acknowledgements

I would like to acknowledge the numerous people for their guidance and support throughout my Master's thesis. First and foremost, I would like to thank Dr. Sean Agnew for continuing to push me to seek to advance this field of research. I would like to thank all of the collaborators working on this joint project, who never ceased asking inquisitive and guiding questions; Dr. Noah Philips, ATI, Dr. Daniel Matejczyk, L3 Harris, Dr. Calvin Mikler, Air Force Research Lab, Dr. Jim Fitz-Gerald and Dr. Chris Goyne, UVA.

I would also be remiss to not thank all of the Agnew group members, past and present, who have helped me throughout this journey. Specifically, I would like to acknowledge those that worked closely with me: Dr. Jonathan Skelton for his guidance and mentorship throughout this work; Claire Kent and Alex Wang for wading through decades of literature with me; and Doyle Weishar for helping out when math got hard.

Most importantly, I would like to thank my friends and family for their continuous and unwavering support throughout my studies. Without you, I would not be in this position; this is as much of an accomplishment for me, as it is for you.

Effort sponsored by the U.S. Government under the Other Transaction number HQ0034219CA04 between PSAH and the Government. The U.S. Government is authorized to reproduce and distribute reprints for Governmental purposes notwithstanding any copyright notation thereon.

The views and conclusions contained herein are those of the authors and should not be interpreted as necessarily representing the official policies or endorsements, either expressed or implied, of the U.S. Government.

Table of Contents

Abstract i

Acknowledgements ii

List of Figures vi

List of Tables ix

Chapter 1: Introduction 1

Chapter 2: Background 5

2.1 Refractory Metals 5

2.2 Creep 6

2.3 Selected Properties to Investigate 9

Chapter 3: A Unified Model of Tensile and Creep Deformation for use in Niobium-Alloy Materials Selection and Design for High-Temperature Applications 12

3.1 Analytical and Experimental Methods and Sources of Data 13

3.1.1 Larson-Miller Parameter 13

3.1.2 Sellars-Tegart Model 15

3.1.3 Melting Points 17

3.2 Results 17

3.2.1 Larson-Miller Parameter 17

3.2.2 Sellars-Tegart Model 19

3.2.3 Melting Points 23

3.3 Discussion 24

3.3.1 Mechanistic Observations 24

3.3.2 Effect of Heat Treatment on Flow Strength of Nb-Alloys 27

3.3.3 Rationale for a Minimum Flow Stress Model 29

3.4 Conclusions 35

Chapter 4: Thermophysical Modeling of Niobium-Alloys Informs Materials Selection and Design for High-Temperature Applications 37

4.1 Analytical and Experimental Methods and Sources of Data 38

4.1.1 Specific Heat Capacity 38

4.1.2 Thermal Conductivity 39

4.1.3 Elastic Modulus 40

4.1.4 Linear Coefficient of Thermal Expansion 42

4.2 Results 43

4.2.1 Specific Heat Capacity 43

4.2.2 Thermal Conductivity 44

4.2.3 Elastic Modulus 46

4.2.4 Linear Coefficient of Thermal Expansion 50

4.3 Discussion 51

4.3.1 Trends in Elastic Modulus 51

4.3.2 Application of Strain Rate Sensitivity 53

4.3.3 Combination of Thermal Properties 55

4.4 Conclusions 57

Chapter 5: Conclusions 59

Chapter 6: Future Work 61

Appendix A: Applicability of Modified Larson-Miller Parameter 64

Appendix B: Summary of New Data Reported in this Thesis 67

Appendix C: Summary of Literature Data Used in this Thesis 72

C.1 Creep-Life Data 72

C.2 Tensile Testing Data 102

C.3 Steady-State Creep Rate Data 114

C.4 Specific Heat Capacity Data 129

C.5 Thermal Conductivity Data 144

C.6 Elastic Modulus 153

C.7 Linear Coefficient of Thermal Expansion 157

Appendix D: Sellars-Tegart Modeling of Ni-, Mo-, and Ta-based Alloys 163

Appendix E: Elemental Thermophysical Properties 164

Appendix F: Density Calculations 166

Appendix G: Comparison of WC-3009 and D-43's Temperature and Strain Rate Sensitivities 169

Appendix H: Minimum Flow Stress Model Results for Ni-, Mo-, and Ta-based Alloys 171

Appendix I: Supplemental TDTR Methods and Analysis 174

References 176

List of Figures

Figure 2.1. *Deformation mechanism map of pure Nb with a 100 μm grain size. The relative boundaries for deformation mechanisms and strain rate contours are labeled to inform engineers on possible dominant creep mechanisms* [46]. 7

Figure 2.2. *Schematics of creep curves for Class 1 (Class A) and Class 2 (Class M) materials, adapted from* [49]*. The distinct regimes of primary, secondary, and tertiary creep are labeled for a Class 2 material, whereas a Class 1 material is expected to mainly exhibit tertiary creep. The creep rate relative to the duration of the creep test is also shown for both material types, illustrating the terms "steady-state", "accelerating", and "minimum" creep rate.* 8

Figure 2.3. *Schematic adapted from* [52] *demonstrating the origins of thermal expansion via the asymmetry of the interatomic potential energy well.* 10

Figure 3.1. *Representative tensile test data obtained from alloy C103 at 1649˚C, initially strained at* $3.3\cdot10^{-4}$ s^{-1} *and jumped to* $8.3\cdot10^{-3}$ s^{-1} *(an increase of 25×) after yield, demonstrating its high strain rate sensitivity. Note the self-similar behavior at the two strain rates which allows extraction of two independent data points for flow stress* 16

Figure 3.2. *Creep-life data for all Nb-alloys considered in this study (all data considered and presented was found in literature), including WC-3009 and C-129(Y), with a parenthetical note of the final heat treatment used for each alloy. All data collapses onto a single line for each alloy, indicating that LMP* is an appliable way to estimate creep strength for these alloys* 18

Figure 3.3. *Creep and tensile data for C103, WC-3009, C-129(Y), Cb-752, D-43, and FS-85 collapse onto a singular curve that is described through the ST equation, indicating it is an applicable model for estimating the strength of these alloys* 20

Figure 3.4. *ST predictions align well with experimental data for (a) FS-85 and (b) alloy WC-3009. It is noted that the predictions fail to perfectly describe the extreme conditions for FS-85, where the discrepancies are nonconservative at the lowest strain rates and conservative at the lowest temperatures. The onset of power-law breakdown occurs to the right of the dashed line, where behavior deviates from linearity on the log-log plot* 23

Figure 3.5. *For all alloys but D-43, all experimental creep stresses fall below the respective alloy's breakaway stress, informing that solute drag can occur at these conditions, and this correlates well with the ST stress exponents. D-43 appears not to be governed by solute drag due to its*

lower alloy content and presence of Zr-carbides, which deplete the matrix of Zr. As breakaway stress decreases, temperature increases relative to the data of each alloy 26

Figure 3.6. *Comparisons between LMP* and ST predicted strength at 10^{-7} s^{-1} for (a) WC-3009 and (b) FS-85. LMP* strength predictions are nonconservative at low temperatures due to extrapolating outside of the high-temperature power-law creep regime tested experimentally and into conditions described by lower activation energies and distinct rate dependencies. Conversely, the ST model is always nonconservative due to ignoring transient creep behaviors* 31

Figure 3.7. *Strain rate is important to consider when selecting a refractory alloy, as some are better suited than others for different rates (i.e., WC-3009 performs significantly better at (a) tensile rates than (b) creep rates). Extrapolations were determined via the bounds of experimental Zener-Holloman values and LMP*s* 32

Figure 3.8. *The transition temperature from the ST to LMP* model in the employed minimum strength prediction correlates strongly with alloy melting temperature. Lower melting point alloys begin rapidly losing strength with increasing temperature (i.e., transition to the LMP* model) at lower temperatures relative to higher melting point alloys. Failure to incorporate this transition when modeling the high-temperature strength of materials will result in nonconservatism and an incorrect ranking of materials at the higher temperatures* 33

Figure 3.9. *Specific strength indices relevant to the design of lightweight panels reveal that Nb-W-Zr alloys (Cb-752 and D-43) excel at both (a) tensile test and (b) creep-type rates. Extrapolations were determined via the bounds of experimental Zener-Holloman values and LMP*s* 35

Figure 4.1. *Heat capacities predicted by Thermo-Calc for all Nb-alloys are similar to those experimentally measured for alloys C103, C-129(Y), and Cb-752* 43

Figure 4.2. *The temperature dependence of the thermal conductivity of (a) Nb- and (b) Ni-, Mo-, and Ta-based alloys. Given the large uncertainty (5 – 20%) in these measurements, it is suggested that there is little composition dependence in the Nb-alloys examined. However, it does appear that WC-3009 has significantly lower thermal conductivity than the other Nb-alloys investigated* . 45

Figure 4.3. *Linear relationships were used to fit high-temperature elastic modulus data for (a) individual Nb-alloys, (b) Nb-alloys assuming the singular temperature dependence, and (c) Ni-, Ta-, and Mo-alloys. WC-3009 was assumed to demonstrate the same trend as C-129(Y) and Cb-752 was modeled with the trend of D-43*.. 49

Figure 4.4. *(a) Linear coefficients of thermal expansion predicted by Thermo-Calc for Nb-alloys are similar to those that have been measured experimentally, except for alloy WC-3009 where the experimental data are significantly higher, possible due to internal oxidation. (b) CTE values for competing alloys are both higher (Ni) and lower (Mo and Ta) than those of Nb-based alloys, respectively* 51

Figure 4.5. *WC-3009 exhibits a more severe stress relaxation than D-43 due to its larger strain rate sensitivity* 55

Figure 4.6. *Nb-W-Zr alloys perform best in this performance index at both (a) 10^{-4} s^{-1} and (b) 10^{-7} s^{-1} due to their relatively high strength, low density, and low CTEs* 57

List of Tables

Table 1.1. *Nb-Alloy Nominal Compositions in wt% (and at%)* 3

Table 1.2. *Ni-Superalloys Nominal Compositions in wt%* 4

Table 1.3. *Ta- and Mo-Based Comparison Alloys Nominal Compositions in wt%* 4

Table 3.1. *Summary of LMP* Model Parameters (Equation 3.7) for Nb-, Ni, Ta-, and Mo-Alloys* 19

Table 3.2. *Sources of Experimental Data used to Develop the Sellars-Tegart model in Figure 3.3* 20

Table 3.3. *Sellars-Tegart Model Parameters and their Respective Standard Deviations* 21

Table 3.4. *Pearson Correlation Coefficients (r) for Each Parameter Pairing in Equation 3.10* 22

Table 3.5. *Liquidus (T_L) and Solidus (T_S) Temperatures According to Thermo-Calc (HEA3 v.3.1 database) and Literature Reported Melting Points (T_m) of the Considered Nb-Alloys* 24

Table 4.1. *Liquidus (T_L) and Solidus (T_S) Temperatures According to Thermo-Calc (HEA3 v.3.1 database) and Literature Reported Melting Points (T_m) of the Considered Nb-Alloys* 39

Table 4.2. *Elastic Modulus Measurements of C103 at Room Temperature and 1093˚C* 41

Table 4.3. *One-Sample t-test Results Comparing Measured WC-3009 Thermal Conductivity Values and the Singular Nb-Alloy Thermal Conductivity Trend* 46

Table 4.4. *Equation 4.3 Parameters for the Nb-Alloys Collectively and WC-3009* 46

Table 4.5. *Alloy Fit Parameters for Equation 4.4* 50

Chapter 1: Introduction

The development of next-generation aerospace structures, such as land-based gas turbines or aeroengines, is driven by the need for improved efficiency [1], [2]. This efficiency is achieved through raising the temperature of certain structures within the engine, and with this increase in temperature, the structural materials are not only required to survive at the elevated temperatures ($\gtrapprox$1300˚C), but also maintain load bearing capability [3], [4], [5]. Current employed materials are Ni-superalloys, but their maximum operational temperature is approximately 1100˚C [2], [6], due to precipitate coarsening, dissolution, and henceforth, incipient melting [7], [8]; therefore, replacement materials are needed to break the temperature barrier Ni-superalloys impose. Of the possible candidates, refractory alloys are considered due to their high melting points (>2000˚C) [9]. Refractory alloys were previously studied for aerospace applications beginning in the mid-1950s, where they were considered for use in the nuclear reactor program [10], [11]. Soon after, their high melting points gained the attention for use in processes with aerothermal heating, such as high-velocity flight or re-entry vehicles. A majority of focus was spent on the development of Nb-based alloys for these applications, rather than Mo, W, or Ta-based ones, as the latter alloys had difficulties associated with their processing and fabrication in which the technology at the time could not accommodate. When welded, Mo-alloys have large grain size differences within the heat affected zone and when recrystallized, demonstrate oxygen embrittlement that additions of carbon have been known to combat [12], [13]; W-alloys experience similar setbacks with regards to their fabrication. It is admitted that all of these refractory metal alloys, including Nb-alloys, have limited oxidation resistance, which has limited their application to specific situations such as rocket engines used to carry payload and personnel into space [11]. However, Nb-based alloys do not exhibit as severe embrittlement, as Nb is the most ductile refractory metal at room temperature, which alleviates some of the complications associated with fabrication. Moreover, density is another important factor to consider when employing materials in aerospace applications, which further precludes W-alloys from their implementation ($\gtrapprox$19 g/cm^3 [14]) and also limits Ta-alloy usage in aeroengines ($\gtrapprox$16 g/cm^3 [15]), although they have been suggested as structural materials within high temperature gas-cooled nuclear reactors. Nb-alloys are also the least dense ($\gtrapprox$8 g/cm^3 [16], providing another reason for the interest in their development for applications in which weight plays an important role, such as the aforementioned aerospace applications.

Recent Nb-alloy development studies (summarized nicely in [5]) have focused on increasing strength, through additions of Re and Al to Nb-Ti-W alloys [17], or the density reducing effects of replacing W and Hf with Mo and Ti, respectively [18]. Although these alloys are promising, their specific yield strengths (strength/density) are typically similar to, or less than, that of WC-3009 (Nb-30Hf-9W wt%), a historical alloy with high tensile strength, at 1200˚C and 10^{-3} s^{-1}. Some Nb-Mo-Zr alloys with small volume fractions of second phase do have high specific yield strengths up to 1600˚C [19]. Refractory high-entropy alloys (RHEAs) or refractory complex concentrated alloys (RCCAs) have also been of interest due to their high strength; however, current RHEA studies have focused on understanding the temperature dependence of their thermophysical properties rather than improving strength. The thermophysical properties of these alloys are predicted through a variety of *ab initio*, CALPHAD, and rule-of-mixtures based techniques. Compared to Nb-alloys, RHEAs generally tend to have a lower thermal conductivity [20], higher coefficient of thermal expansion (CTE) [21], [22], [23], [24], larger specific heat capacity [21], [22], [24], and comparable, sometimes lower, densities [20], [22], [25]. In some applications, these properties are desired (i.e., a low thermal conductivity is ideal for self-healing and irradiation resistance [20], and a high CTE is preferred for thermostat applications [26]). However, in other applications, such as ones that require thermal shock resistance, these relative RHEA properties are unfavorable compared to Nb-alloys, regardless of their higher strength. In light of these current strides to advance modern refractory alloys, it must be acknowledged that the understanding of previously developed alloys is incomplete, specifically for their high-temperature strength and thermophysical properties. A better understanding would inform future Integrated Computational Materials Engineering (ICME) type alloy design efforts, hence the elevated temperature properties of historically developed Nb-alloys will be the focus of this thesis.

Although Nb-alloys have previously been considered as likely candidates for aerospace applications, only two Nb-alloys are currently commercially available, C103 and Nb-1Zr (Nb-1Zr wt%), and they are considered “low-strength” relative to other Nb-alloys, rendering easier fabrication [10]. In this work, five Nb-alloys, in addition to C103, were selected for investigation and their nominal compositions are listed in Table 1.1. The selected alloys include the ubiquitous, but relatively low strength Hf-containing alloy, C103; a higher strength Hf-alloy, WC-3009 that also contains significant W; C-129(Y), which is intermediate in composition between these two; two Hf-free alloys with very similar compositions, Cb-752 and D-43, in which D-43 includes C additions that gives rise to carbide precipitates; and finally, an alloy, FS-85 that contains a high fraction of refractory additions (namely Ta, in addition to W, which is also present in the other alloys). The main strengthening approach of these alloys is solid solution alloying, with the main solid solution additions being W and Ta. Group 4 elements Hf, Ti, and Zr are commonly added as getter-elements such that oxides or carbides preferentially form [27], which provides these alloys with precipitation strengthening as well. It should be noted that all alloys except for D-43 were intentionally designed to be single-phase, but all are commonly observed as multi-phase due to the aforementioned oxides/carbides.

Table 1.1. *Nb-Alloy Nominal Compositions in wt% (and at%)*

	Alloy \ **wt% (at%)**	**Nb**	**W**	**Zr**	**Hf**	**Ta**	**Ti**	**C**
[16]	C103	Balance	--	--	10 (5.4)	--	1 (2.0)	--
[16]	WC-3009	Balance	9 (5.6)	--	30 (19.2)	--	--	--
[28]	C-129(Y) *	Balance	10 (5.6)	≤0.5	10 (5.4)	≤0.5	–	–
[29]	Cb-752	Balance	10 (5.3)	2.5 (2.7)	--	--	--	--
[30]	D-43	Balance	10 (5.3)	1 (1.1)	--	--	--	0.1 (0.8)
[16]	FS-85	Balance	10 (6.2)	1 (1.3)	--	28 (17.7)	--	--

* C-129(Y) label denotes both C-129, which may contain up to 0.5 wt% Ta and 0.5 wt% Zr, and C-129Y, which also contains 0.1 wt% Y

Altogether, this thesis provides engineers with (i) a comprehensive collection of mechanical property and relevant thermophysical materials data, (ii) select data that was missing from the extant literature database (especially for alloys C103 and WC-3009), (iii) physics-based empirical rules for interpolation and extrapolation of existing materials data, (iv) an example of a materials selection process involving resistance to thermal transients and gradients, (v) particular instances where Nb-alloy performance is outstanding relative to other competing materials, and (vi) the thesis will highlight specific gaps in the literature that require further research. Throughout the thesis, the performance of Ni-based superalloys MAR-M247 [31] and Haynes 230 [32], Ta-based alloy ASTAR-811C [33], and the Mo-based alloy TZM [34] were employed for comparative purposes (compositions in Tables 1.2-1.3).

Table 1.2. *Ni-Superalloys Nominal Compositions in wt%*

	Alloy \ **wt%**	**Ni**	**Cr**	**Co**	**Mo**	**W**	**Al**	**Ti**	**Ta**	**Hf**	**C**	**Zr**
[31]	MAR-M247	Balance	8.4	10	0.7	10	5.5	1.05	3.1	1.4	0.15	0.05
		Ni	**Cr**	**Mo**	**W**	**Al**	**Mn**	**Si**	**Al**	**C**	**La**	Can include additions of Fe, Co, Nb, Ti, and B
[32]	Haynes 230	Balance	22	2	14	0.3	0.5	0.4	0.3	0.1	0.02	

Table 1.3. *Ta- and Mo-Based Comparison Alloys Nominal Compositions in wt%*

	Alloy \ **wt%**	**Ta**	**Mo**	**W**	**Hf**	**Re**	**Ti**	**Zr**	**C**
[35]	ASTAR-811C	Balance	--	8	0.7	1	--	--	0.025
[36]	TZM	--	Balance	--	--	--	0.5	0.08	0.03

Chapter 2: Background

2.1 Refractory Metals

Refractory metals are generally considered to consist of Group 5 and 6 elements and receive many of their notable characteristics from being transition metals. The hybridization and orbital structure of the partially full d-orbitals in these metals result in a covalent nature of the bonding, giving rise to their high melting points (>2000˚C) [37]. Tungsten may be the most recognized refractory metal, as it is commonly used as an electron source or in filaments due to its high melting point [38]; the other refractory metals include Nb, Ta, Mo, Cr, and Re (Group 7) [39]. Another linking characteristic between all refractory metals is their body-centered cubic (bcc) crystal structure, which aids in promoting complete solubility within one another at high-temperatures [40]. Group 4 metals, such as Hf, Zr, and Ti, may also broadly be considered refractory metals, but they possess hexagonal close packed structures and have significantly lower melting points than the Group 5 and 6 materials. Nonetheless, these enticing attributes of refractory metals are counterbalanced by the difficulties associated with their processing, which alludes to their namesake of "refractory". Most of these metals suffer from a severe lack of ductility at low-temperatures, which is a consequence of their covalent bonding and bcc structure (i.e., the presence of a ductile-to-brittle transition). This issue of ductility contributes to the difficulties associated with the post-processing of refractory materials, where tools are required to impart a high enough flow stress to deform the material, while avoiding cracking the specimen and itself [37]. Moreover, with respect to producing refractory alloys, common fabrication techniques, such as investment casting, have proven unsuccessful due to the affinity of refractory metals for impurities, especially oxygen [41], meaning that any elevated temperature processing of refractory material must be conducted under vacuum. However, their relatively low vapor pressures make them ideal candidates for purification via electron beam melting [42], these purified ingots are then commonly used within vacuum induction melting or vacuum arc melting processes [19], [37]. Of course, the low vapor pressure (i.e., high melting point) indicates that a significant energy input is required to purify and melt the materials, which instruments are currently able to meet, but were not able to in the past [16]. Electron beam melting and arc-casting were not introduced until the early 1960s, meaning that typical means of producing Nb-alloys included powder metallurgy, but such could only be done in small batches; it was not until the late 1960s when successful fabrication techniques were developed [10]. However, by this time, other material systems were selected for the applications refractory alloys were considered for, meaning that refractory alloy research halted [11]. Recent studies have demonstrated the success of additively manufacturing such materials [11], [43], where these advances in fabrication techniques reopen the door to refractory metal research, allowing for the further advancement of structural aerospace materials.

2.2 Creep

When employing a material in high-temperature applications, such as the aforementioned aerospace ones, one needs to be mindful of the tendency of the material to creep. Creep is the time-dependent deformation of a material and is typically observed at high homologous temperatures [44]. There are three main mechanisms that accommodate creep deformation: dislocation slip (or glide), dislocation climb, and diffusional flow [45]; dislocation slip is thermally enhanced dislocation motion within the glide plane, dislocation climb is thermally enhanced dislocation motion out of the glide plane which requires diffusion, and diffusional flow involves strain accommodation via mass flow itself, either along grain boundaries or within the lattice.

Deformation mechanism maps are commonly employed to determine which of these creep deformation mechanisms will be dominant at a given applied stress, temperature, or application strain rate; Figure 2.1 presents a map for pure Nb [46]. As far as the author is aware, there are no published deformation maps for Nb-alloys. Conventional thermally activated plasticity occurs at the highest stresses, whereas dislocation creep (also referred to as power-law creep) and diffusional flow regimes appear at high homologous temperatures ($\frac{Absolute\ Temperature}{Absolute\ Melting\ Point}$) and lower stresses. It is important to note that all creep mechanisms can occur simultaneously and contribute to deformation, but typically only one will dominate. Power-law creep is generally understood to be the result of dislocation climb and glide (Class 2 or Class M behavior) or solute drag-controlled dislocation glide (Class 1 or Class A behavior). As mentioned above, diffusional flow can occur along grain boundaries, referred to as Coble creep, or through the lattice, i.e., Nabarro-Herring creep. Therefore, the creep response of a material is not only dependent on its melting point, but also on various forms of diffusion and its sensitivity to applied strain rate or stress.

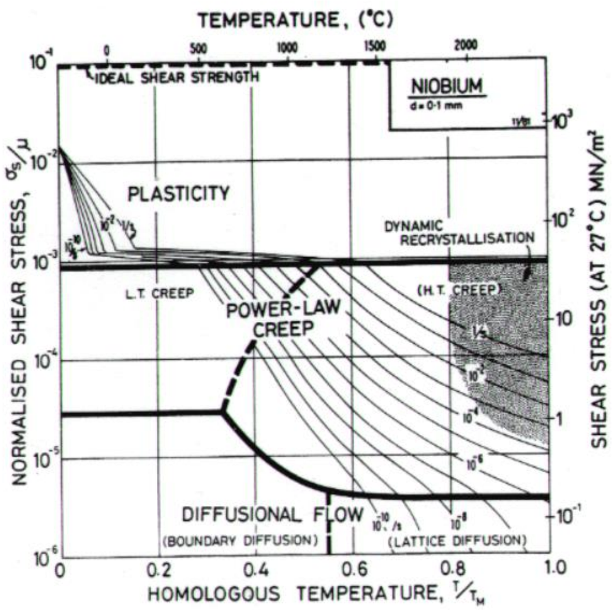

Figure 2.1. *Deformation mechanism map of pure Nb with a 100 μm grain size. The relative boundaries for deformation mechanisms and strain rate contours are labeled to inform engineers on possible dominant creep mechanisms* [46].

The high melting points of refractory alloys make them enticing for high-temperature applications, as they will have smaller homologous temperature relative to other commonly employed aerospace materials (e.g., Ni-based superalloys). This means that there may be a temperature region in which creep is not expected in refractory alloys but would be in other systems. However, when considering diffusion, face-centered cubic (fcc) materials are expected to have superior creep resistance relative to bcc materials (i.e., refractory metals) because the close-packed nature of the fcc structure reduces the ease of atomic mobility, inhibiting diffusion [47]. This is a reason that fcc Ni-superalloys are preferred for specific aerospace applications.

Another reason in which Nb-alloys should be used above the temperature capabilities of Ni-superalloys is because of their larger strain rate sensitivities relative to Ni-alloys. Strain rate sensitivity (*m*) is a property that quantifies the change in material strength when exposed to a different loading rate and can also be understood through a material's stress exponent (*n*), as they are inversely related (Equation 2.1). The physical basis of this property lies within the thermally activated nature of dislocations overcoming obstacles that inhibit deformation, as strain is the macroscopic representation of dislocation motion in response to applied stress [48]. A material with a large strain rate sensitivity (or small stress exponent) will experience a large change in flow stress when the strain rate is changed. Typically, solid solution alloys with large lattice mismatches (i.e., most Nb-alloys) are found to have high strain rate sensitivities

(~0.3) and are referred to as Class 1 or Class A materials, whereas Class 2 or Class M materials have smaller sensitivities (≲0.2). In addition to a distinct strain rate sensitivity, these Classes of materials also have creep curves with characteristic shapes. Class 1 (Class A) materials demonstrate limited primary and secondary (steady-state) creep, and exhibit mainly tertiary (accelerating) creep; whereas Class 2 (Class M) alloys are expected to demonstrate distinct regions of all three types (denoted in Figure 2.2).

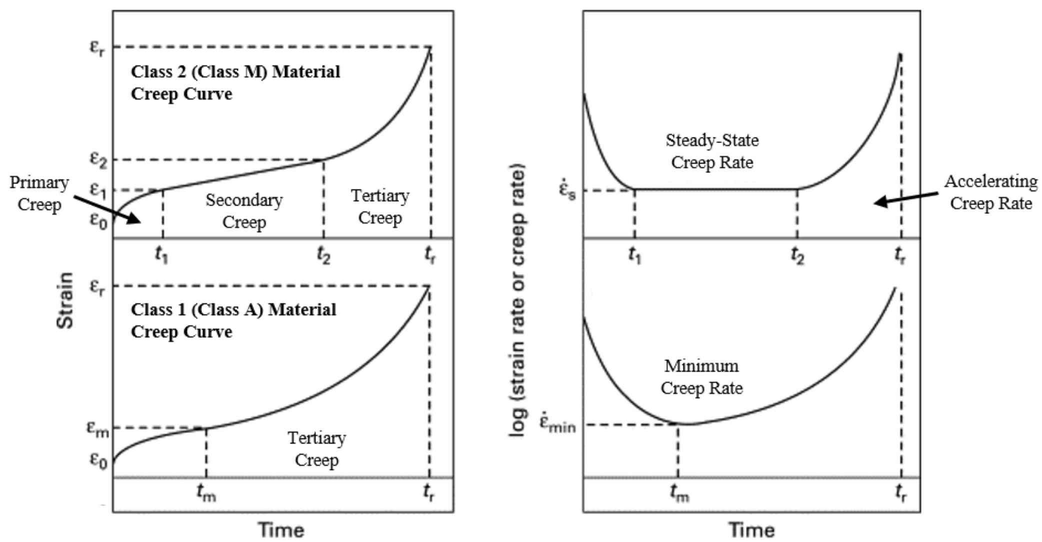

Figure 2.2. *Schematics of creep curves for Class 1 (Class A) and Class 2 (Class M) materials, adapted from* [49]. *The distinct regimes of primary, secondary, and tertiary creep are labeled for a Class 2 material, whereas a Class 1 material is expected to mainly exhibit tertiary creep. The creep rate relative to the duration of the creep test is also shown for both material types, illustrating the terms "steady-state", "accelerating", and "minimum" creep rate.*

As previously mentioned, a material's strain rate sensitivity can also inform on the dominant creep deformation mechanism at the given applied stress and temperature. For example, a stress exponent of *n*=3 (or strain rate sensitivity of ~0.3) indicates that the rate controlling mechanism is the dragging of either solute (i.e., solute drag) or precipitates within grains when the back stress is accounted for [50]. An exponent of *n*=5+ (or strain rate sensitivity ≲0.2) is indicative of dislocation climb and glide. As alluded to above, many factors contribute to the response of materials at high temperatures, therefore, a focus of this thesis is to understand the creep response of the selected Nb-alloys and provide approaches, models, and trends that can be employed by engineers to ensure the proper selection of a material for high-temperature applications.

$$m = \frac{\partial ln(\sigma)}{\partial ln(\dot{\varepsilon})} = \frac{1}{n} \qquad \text{Equation 2.1}$$

2.3 Selected Properties to Investigate

High-temperature strength is not the only property that must be considered when selecting materials for high-temperature applications. Another mechanical property that must be considered is the elastic modulus, which is a measure of a material's resistance to elastic deformation, and on the atomic scale, is a measurement of resistance to bond stretching. The elastic modulus is used to describe the magnitude of elastic stress in a corresponding direction of strain and in high-temperature applications, a lower elastic modulus is often preferred as this reduces the stress the material experiences at a given strain level [51]. A smaller stress is important at high temperatures because it will promote lower plastic strain rates. Along these lines, the coefficient of thermal expansion is also an important property to consider for high-temperature applications, as materials with larger CTEs will experience greater strains at a given change in temperature. Thermal expansion is physically derived from the asymmetry of the energy well of the interatomic potential of the material. As temperature increases, the vibrational amplitude of the atoms increases in an anharmonic manner, and this causes thermal expansion [52]. If the energy well were symmetric, the mean position of all the atoms would be constant at all temperatures, resulting in no thermal expansion (illustrated in Figure 2.3). Due to the d-orbitals within refractory metals, the bond energy of these materials is significantly larger than others, which leads to step energy wells (i.e., limited asymmetry), and therefore, lower coefficients of thermal expansion [52], especially when compared to Ni-alloys. The influence that thermal expansion and elastic modulus have on the performance of a material exposed to high temperatures is often considered in the context of thermal gradients and/or thermal transients (i.e., thermal shock). In this context, a lower CTE is preferred to reduce the strain of the material and when coupled with a low elastic modulus, the thermal stress that the material experiences is also reduced, which prolongs the life of the component.

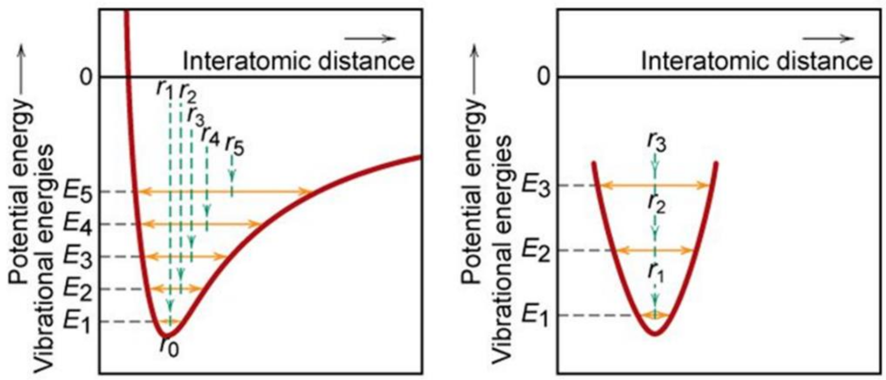

Figure 2.3. *Schematic adapted from* [52] *demonstrating the origins of thermal expansion via the asymmetry of the interatomic potential energy well.*

Another set of properties important to consider in high-temperature applications are those that allow the material to resist temperature change; these properties include specific heat capacity and thermal conductivity. Typically, bcc materials have lower thermal conductivity values than fcc alloys due to the increased packing density of the fcc crystal, which improves the material's efficiency of transferring heat [53]. Regarding refractory alloys specifically, their affinity for impurities can have a detrimental effect on thermal conductivity if the sample is not handled in proper environments. Generally, any feature within the lattice (i.e., solute atoms and crystal defects) can serve as a scatterer, meaning that any interstitial- or substitutional-solute strengthener can significantly decrease the thermal conductivity of the alloy relative to the pure material [54]. Therefore, in addition to having a bcc structure, the high alloying content within Nb-alloys and their affinity for impurities further reduces their thermal conductivities. Ni-superalloys also have poor conductivity as they contain significant amounts of various solute additions. A material with poor thermal conductivity employed in a high-temperature application can form hot spots, which are local increases in temperature that weaken that section of the component. Therefore, a high thermal conductivity is preferred, unless the material is serving in the capacity of a thermal barrier coating. Similarly, specific heat capacity affects the overall temperature of the material, as it is a measurement of the amount of energy needed for a unit of mass to increase one degree in temperature; it informs on the material's ability to absorb heat [52]. A large specific heat capacity means that it takes more energy for the material to increase in temperature. Although it is often assumed that elemental solids follow the Dulong-Petite law, which states that the heat capacity will eventually plateau at 3R in an ideal system, specific heat capacity continues to slowly increase with temperature due to anharmonicities within the lattice [55], [56]. To put thermal conductivity and specific heat capacity in the context of a component exposed to a thermal gradient, materials with large conductivities and heat capacities are preferred, as they will lessen the temperature gradient within the material. This thesis aims to not only present the thermophysical properties of Nb-alloys and their corresponding temperature dependencies, but to also understand the implications the combined properties set will have on alloy performance in hypothetical applications. This will be done through the use of performance indices that combine the properties in ways which are meaningful for a given application.

Chapter 3: A Unified Model of Tensile and Creep Deformation for use in Niobium-Alloy Materials Selection and Design for High-Temperature Applications

The work in this chapter is currently in preparation for publication. As the lead author, I performed the data collection from literature and analysis of data gathered (i.e., of those via literature and those provided by collaborators). As lead author, I also completed the writing, reviewing, and editing of this work. The additional contributing authors and their roles within this study are as described below:

i. Dr. Noah R. Philips (ATI Specialty Alloys & Components, Albany, OR) provided specific experimental data (i.e., high-temperature tensile tests of C103 and WC-3009 samples) that did not exist in literature prior to this work and were therefore used within subsequent analysis. Dr. Noah R. Philips also provided insights into results and modeling techniques, and reviewed and edited the paper.
ii. Dr. Daniel E. Matejczyk (Aerojet Rocketdyne, an L3 Harris company, Los Angeles, CA) provided guidance and insights with respect to results and modeling techniques.
iii. Dr. Jonathan M. Skelton (Materials Science and Engineering, University of Virginia, Charlottesville, VA) provided guidance with respect to results and modeling techniques,
iv. Dr. James M. Fitz-Gerald (Materials Science and Engineering, University of Virginia, Charlottesville, VA) served as the main Principal Investigator of the grant that funded this work.
v. Dr. Sean R. Agnew (Materials Science and Engineering, University of Virginia, Charlottesville, VA) assisted in the writing, reviewing, and editing of the paper, as well as provided guidance on the conceptualization of the study and analysis.

As application temperatures increase, the viscoplastic nature of metallic alloys becomes more significant, and using temperature-dependent yield strength as a design or materials selection metric to compare alloys becomes invalid. As a bare minimum, flow stresses must be measured and compared at the same strain rate, but more generally, the temperature-dependent strain rate sensitivity should also be considered. It is of interest to have simple constitutive descriptions that enable comparisons to be made amongst candidate materials across a wide range of possible strain rates and temperatures. Two classical approaches considered presently involve a Larson-Miller parameter (LMP) analysis of creep-life data and the Sellars-Tegart (ST) model, which is derived from steady-state material responses. Both empirical models experience limitations originating within their derivation, therefore, it is advantageous to explore both the general applicability of each model in the investigated conditions for Nb-alloys and compare their shortcomings.

3.1 Analytical and Experimental Methods and Sources of Data

3.1.1 Larson-Miller Parameter

The Larson-Miller parameter (LMP) is commonly employed as a means of collapsing stress rupture data obtained at various temperatures to a singular curve [57]. This parameter was originally developed by Hollomon and Jaffe [58] to relate annealing time and temperature to hardness, and implicitly assumes that the same deformation mechanism governs material response across all conditions modeled. With this assumption, the familiar Dorn power-law expression (Equation 3.1), coupled with an Arrhenius expression for temperature dependence, is rearranged to represent the log of stress as a function of rate ($\dot{\varepsilon}$), temperature (T), and various material constants (A, n, Q) (Equation 3.2). Equation 3.2 contains a precursor of the LMP within its square brackets; the Young's modulus term, *E(T)*, is typically ignored as the property weakly varies with temperature and is therefore assumed as a constant.

$$\dot{\varepsilon} = A\left(\frac{\sigma}{E(T)}\right)^{n} exp\left(\frac{-Q}{RT}\right) \qquad \text{Equation 3.1}$$

$$\log\sigma = -\frac{1}{n}\left[\log\left(A\,exp\left(\frac{-Q}{RT}\right)\right) - \log(\dot{\varepsilon})\right] + \log E(T) \qquad \text{Equation 3.2}$$

To express Equation 3.2 in terms of rupture time, Garofalo's equation that relates steady-state creep rate ($\dot{\varepsilon}$) to rupture time (t) (Equation 3.3) is substituted into Equation 3.2 [59]. In this relationship, Garofalo observes that creep curves tend to exhibit a parabolic shape, meaning that creep rate decreases with time. This substitution results in Equation 3.4 and through combining the non-time dependent terms within the square brackets into *C(T)*, the Larson-Miller parameter is obtained (Equation 3.5). Similar to *E(T)*, *C(T)* does not depend strongly on temperature, and it has been assumed constant with a value ranging from 15 to 20 in the literature. Equation 3.5 has been successfully employed to compare the times to rupture across many alloys and is commonly referred to as "temperature compensated time".

$$\dot{\varepsilon} = \left(\frac{B}{t}\right)^{\frac{1}{\alpha}} \qquad \text{Equation 3.3}$$

$$\log\sigma = -\frac{1}{n\alpha T}\left[\mathrm{T}\cdot\left\{\alpha\log\left(A\,exp\left(\frac{-Q}{RT}\right)\right) - \log B + \log(t)\right\}\right] + \log E(T) \qquad \text{Equation 3.4}$$

$$\text{LMP} = T(K) \cdot [C(T) + \log t] \cdot 10^{-3} \qquad \text{Equation 3.5}$$

Specifically for refractory alloys, some researchers have shown (without comment, [60], [61]) that creep data of various strain levels can be further collapsed onto a single curve if a modified Larson-Miller parameter is employed (Equation 3.6), which is readily derived from Equation 3.2. A *C'(T)*=15 is commonly used for refractory alloys [61], [62], [63], which is supported by a Stephenson study, [64], in which *C'(T)* was fit for each level of creep strain (i.e., 1%, 2%, etc.), and a constant of 15 resulted in the smallest error between experimental and predicted stresses.

$$LMP^{*} = T(K) \cdot [C'(T) - \log(\varepsilon(\%)/t(hr))] \cdot 10^{-3} \qquad \text{Equation 3.6}$$

Further collapse of creep-life data via LMP* is permitted for alloys that exhibit slowly accelerating creep behavior (tertiary creep) over most of their creep life. In such cases, the creep curves can be roughly described by a linear relationship with time (rather than the parabolic relationship suggested by Garofalo or Andrade [65]). Such a relationship allows any level of strain and corresponding time to determine the LMP* for a given stress and temperature (see Appendix A for an example demonstration). For alloys that exhibit all stages of creep (primary, secondary, and tertiary) with abrupt transitions between them, this additional collapse of the data is not possible (see Appendix A for a Ni-based superalloy which exemplifies this behavior). However, in the present context, this has a powerful effect of accounting for transient creep behavior by averaging the strain rate over the strain range of interest. This point is leveraged within the present assessments of various Nb-alloys, as discussed in the minimum flow stress modeling section below.

Data for the present LMP assessments were obtained from reported creep tests conducted at different stresses and temperatures, yielding the times associated with various strain levels, often 1%, 2%, 5% and 10% strain. The literature sources employed for each alloy are listed in subsequent sections. Caution must be taken when extrapolating to conditions outside of those that have been empirically tested, as it can possibly result in large errors due to a possible change in the underlying deformation mechanism, which would result in new parameters in Equation 3.1. For much of the data, an exponential relationship between stress and LMP* (Equation 3.7) enables fitting a linear regression (on a semi-log plot of stress and LMP*) to determine the parameters *a* and *b*.

$$\sigma_{LMP} = 10^{\,a+b\cdot LMP^{*}} \qquad \text{Equation 3.7}$$

3.1.2 Sellars-Tegart Model

In 1963, Garofalo suggested a hyperbolic sine function raised to a power to describe the stress dependence of steady-state (or minimum) creep rate (Equation 3.8) [66]. This function asymptotes to an exponential function at high stresses (typical of thermally activated plasticity) and a power function at low stresses (typical of climb- and glide- controlled creep). However, Garofalo acknowledged that his proposed equation was not fully validated through experimental work, as only a narrow range of test conditions had been reported in the literature at the time [67]. In 1966, Sellars and Tegart (ST) improved Garofalo's equation by introducing an Arrhenius term to better capture the temperature dependence of the steady-state strain rate, resulting in Equation 3.9; this was demonstrated using hot torsion data from steels and copper [68]. Their model effectively employs the Zener-Holloman parameter, *Z*, as a temperature-compensated strain rate (Equation 3.10); in these expressions, Q, A, n, and α are material parameters.

$$\dot{\varepsilon} = A \sinh^{n}(\alpha\sigma) \qquad \text{Equation 3.8}$$

$$\dot{\varepsilon} = A \sinh^{n}(\alpha\sigma)\exp\left(\frac{-Q}{RT}\right) \qquad \text{Equation 3.9}$$

$$Z = \dot{\varepsilon}\exp\left(\frac{Q}{RT}\right) = A \sinh^{n}(\alpha\sigma) \qquad \text{Equation 3.10}$$

It is important to note that the ST approach is inherently nonconservative since all transient behavior (strain hardening/softening or primary/tertiary creep) is ignored. This is important because Nb-based refractory alloys have been reported to exhibit what is known as Class 1 (or Class A) solute drag type creep behavior, which is characterized by minimal primary and secondary creep [69]. Generally, the minimum creep rate reported in literature was employed in developing the ST models (sources per alloy in future sections). It should be noted that the secondary creep rates reported for WC-3009 by Wadsworth et al. [69] are the same data measured by Hebsur in [62]. Wadsworth et al. normalized the strain rate data using a diffusivity at each temperature, which was determined by solving for the pre-exponential coefficient (D_0 = 1.17 cm^2/s) and assuming an activation energy of 295 kJ/mol.

Ultimate tensile stress (UTS) values reported at known tensile test strain rates were also used as representatives of steady-state flow stress. Similar to the minimum strain rate in a creep test, the UTS is the point at which strain hardening and geometrical softening are balanced. Rolled sheet coupons of Hf-containing Nb-alloys, C103 and WC-3009, were tensile tested in the fully recrystallized condition[1], in addition to additively manufactured WC-3009 samples tested in the as-printed condition [43], to extend the available flow stress data in the literature, with particular attention paid to filling gaps between existing tensile data and creep test data (see Appendix B for tabulated data). The test apparatus consisted of a radiatively heated, all-metal high-vacuum furnace within a 5988 Instron test frame, which provides feedback-controlled crosshead displacement in accordance with ASTM E8 and E21 [70], [71], at temperatures ranging from 1093˚C to 1649˚C. An initial crosshead velocity of 8.1×10^{-3} mm/s (0.02 in/min) was later increased to 0.20 mm/s (0.5 in/min). Given the initial gauge lengths of 25.4 mm (1 in), the corresponding strain rates were 3.3×10^{-4} and 8.3×10^{-3} s^{-1}. The representative data in Figure 3.1 shows how rate sensitive these alloys can be, with the UTS values indicated with stars. Results of these tests are differentiated by symbols in the presentation of ST models to distinguish them from the data obtained from the literature.

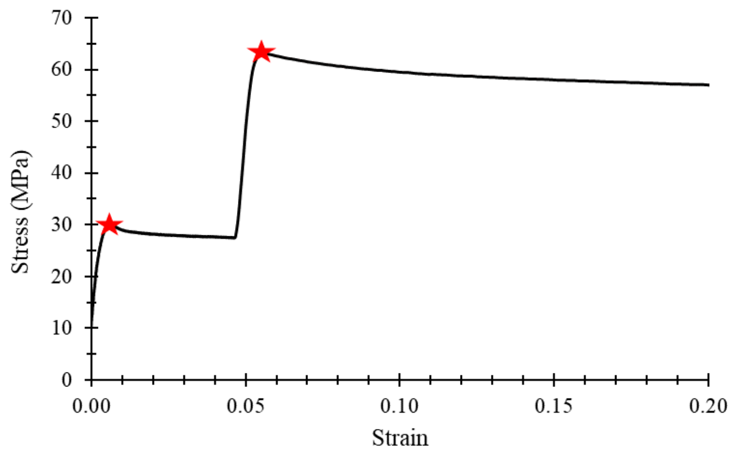

Figure 3.1. *Representative tensile test data obtained from alloy C103 at 1649˚C, initially strained at $3.3\cdot10^{-4}$ s^{-1} and jumped to $8.3\cdot10^{-3}$ s^{-1} (an increase of 25×) after yield, demonstrating its high strain rate sensitivity. Note the self-similar behavior at the two strain rates which allows extraction of two independent data points for flow stress.*

---

[1] No attempt was made in the heat treatment to optimize strength for a particular condition. Heat treatments were standard mill anneals, C103 samples were held at 1316°C for 1 hr and WC-3009 samples for 2 hr at 1260°C.

MATLAB's *MultiStart* nonlinear least squares regression tool[2] was used to fit *Q*, *A*, *n*, and α in Equation 3.10 for each alloy by randomly selecting 5,000 initial guesses from the input parameter space. Use of a *Mutlistart*-type fitting algorithm was required to find global minima in the sum-of-squared residuals between experimental and predicted flow stress (i.e., any software with a similar tool can be used, this analysis technique is not MATLAB specific). To address possible uncertainties within the data, bootstrapping was used to generate statistical uncertainties of the fitting parameters [72] (using MATLAB's *bootstrp*[3] and *fmincon*[4] tools), and literature values of *Q* and *n* for each alloy were used to guide the fitting process (reference values in: [62], [69], [73], [74], [75], [76], [77], [78], [79], [80], [81]). Bootstrapping was selected over other uncertainty analysis techniques, such as Monte Carlo or Pearson's chi-squared test because it does not assume a normal distribution and does not require knowledge on the degrees of freedom, which is difficult to determine in non-linear regressions [72]. In bootstrapping, a new set of data was generated by adding a randomly selected residual ($\sigma_{experimental} - \sigma_{ST}$) to each experimental value. Then, the parameters were refit to the new data; this was repeated 10,000 times and results were used to calculate standard deviations. The "goodness-of-fit" between the ST model and experimental data were evaluated both qualitatively and quantitatively, as discussed in subsequent sections.

3.1.3 Melting Points

Melting points were collected for the alloys from references [28], [30] and [82]. Liquidus (T_L) (i.e., when the first liquid forms) and solidus (i.e., when the material is comprised only of solids) temperatures (T_S) were estimated using Thermo-Calc, informed by the HEA3 v.3.1 database and the one-axis equilibrium template. For the alloys with more than three constituents, such as D-43 and FS-85, these single-axis equilibrium values are reported, whereas ternary phase diagrams were constructed for the ternary alloys (i.e., C103, WC-3009, Cb-752) to get more accurate estimates of the melting temperatures.

3.2 Results

3.2.1 Larson-Miller Parameter

Leonard [82] constructed LMP* plots for comparing Nb-alloys C103, FS-85, Cb-752, and D-43, but WC-3009 and C-129(Y) were not included in that review due to Hf content. R^2 values were used to inform on the "goodness-of-fit" of LMP* parameters for each alloy, as well as inform on possible uncertainties of the data; accepted fits and corresponding R^2 values are presented in Table 3.1; a level of uncertainty may

---

[2] https://www.mathworks.com/help/gads/multistart.html

[3] https://www.mathworks.com/help/stats/bootstrp.html

[4] https://www.mathworks.com/help/optim/ug/fmincon.html

exist within the D-43 data, which is attributed to the use of multiple data sources within the LMP* development of D-43. As shown in Figure 3.2, WC-3009 exhibits creep-life behavior similar to that of C103. The similar alloy C-129(Y) demonstrates improved creep resistance relative to the other Hf-containing alloys, which is correlated to its higher melting point, as addressed in subsequent sections. Various studies included different thermomechanical processing schedules, and heat treatment does affect the creep-life response of many alloys, including Cb-752, D-43, and FS-85. Therefore, in the presented LMP* plots and fits, only the data resulting from the optimal heat treatment for each alloy (when available) is presented. Thus, nonconservative estimates could result from the use of material processed by other routes. Further discussion of the effects of heat treatment is in the discussion section below. It should be noted that creep-life data from Wojcik's 1988 study on P/M processed WC-3009 [83] was used to develop the LMP* fit, even though the creep performance of WC-3009 in his later 1993 review [16] surpassed that of [83]; it was unclear how the data in the later paper was measured or derived from the previous data. Fitting parameters of the reference alloys and their sources analyzed are also reported in Table 3.1; fitting parameters of MAR-M247, Haynes 230, and ASTAR-811C were ultimately based off of data from: MAR-M247: [84], [85]; Haynes 230: [86]; and ASTAR-811C: [77].

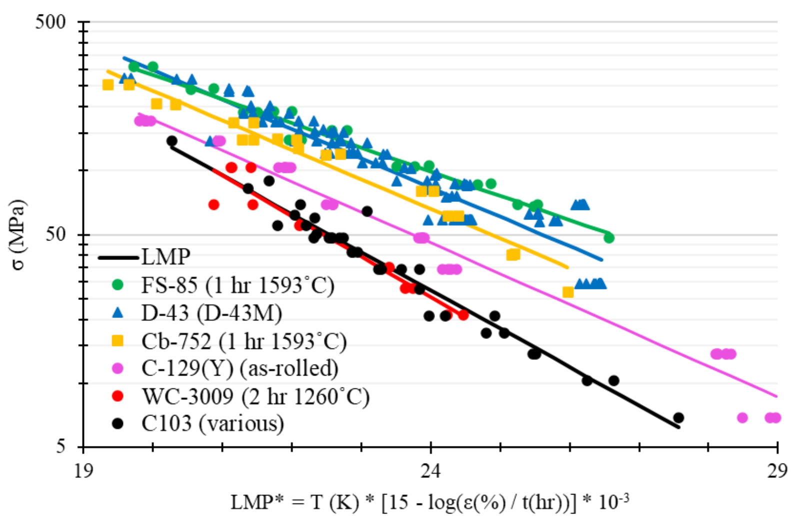

Figure 3.2. *Creep-life data for all Nb-alloys considered in this study (all data considered and presented was found in literature), including WC-3009 and C-129(Y), with a parenthetical note of the final heat treatment used for each alloy. All data collapses onto a single line for each alloy, indicating that LMP* is an appliable way to estimate creep strength for these alloys.*

Table 3.1. *Summary of LMP* Model Parameters (Equation 3.7) for Nb-, Ni, Ta-, and Mo-Alloys*

Alloy	***a***	***b***	**R^2**	**Sources Analyzed**
C103	5.80	-0.180	0.96	[16], [87]
WC-3009	5.98	-0.191	0.93	[16], [83]
C-129(Y)	5.14	-0.145	0.98	[28]
Cb-752	5.16	-0.139	0.96	[75], [88]
D-43	5.23	-0.138	0.86	[76], [88], [89]
FS-85	4.72	-0.114	0.97	[16], [75], [88]
ASTAR-811C	4.86	-0.107	0.75	[77], [90], [91]
TZM Stress Relieved	5.30	-0.133	0.89	[36]
TZM Recrystallized	4.64	-0.112	0.90	[36]
MAR-M247	5.09	-0.138	0.89	[84], [85]
Haynes 230	5.25	-0.181	0.96	[86]

3.2.2 Sellars-Tegart Model

Figure 3.3 demonstrates how well the ST model (Equation 3.10) represents experimentally measured data obtained from both creep (open symbol) and tensile test (close symbol) data (sources in Table 3.2) for a variety of Nb-alloys as functions of the Zener-Holloman parameter, *Z*. See Table 3.3 for Nb-alloy parameter values and Appendix D for a similar treatment of the representative Ni-, Mo-, and Ta-based alloys, which demonstrate the broad applicability of this approach. It is noted that the creep data used to develop the ST curve for the most common Nb-alloy, C103, originated from samples with oxygen concentrations ranging from 170 to 1500 ppm. All of the C103 data falls on a singular curve, and no oxygen concentration dependence in the flow strength was detected when comparing samples tested at similar strain rates and temperatures. Similarly, C-129 and C-129(Y) exhibit indistinguishable creep responses (small additions of Y in C-129Y were designed to improve weldability [28]).

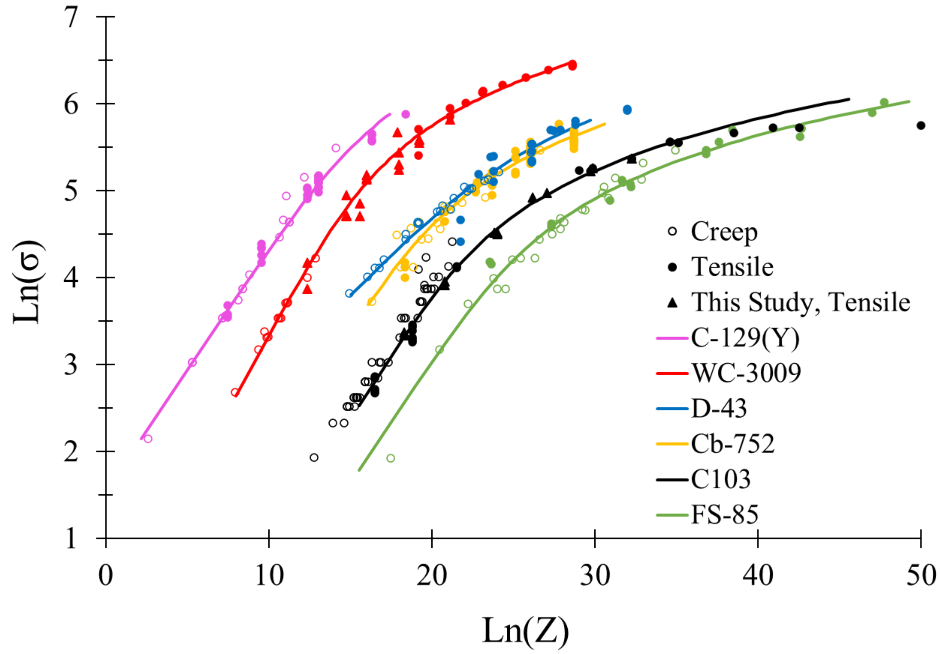

Figure 3.3. *Creep and tensile data for C103, WC-3009, C-129(Y), Cb-752, D-43, and FS-85 collapse onto a singular curve that is described through the ST equation, indicating it is an applicable model for estimating the strength of these alloys*.

Table 3.2. *Sources of Experimental Data used to Develop the Sellars-Tegart model in Figure 3.3*

Alloy	Sources Analyzed
C103	[73], [87], [92], [93], [94]
WC-3009	[62], [83]
C-129(Y)	[28], [95], [96]
Cb-752	[75], [96], [97], [98], [99], [100]
D-43	[89], [98], [100], [101]
FS-85	[75], [100], [101], [102]
ASTAR-811C	[77], [103]
TZM Stress Relieved	[36], [63], [104]
TZM Recrystallized	[36], [63], [78], [105]
MAR-M247	[81], [84]
Haynes 230	[80], [106]

There are limits to the applicability of the ST model. All alloys demonstrated a plateau of their flow stress at higher *Z* levels corresponding to lower temperatures and higher strain rates. This is presented in Figure 3.3 for alloy C103. These plateaus are suggestive of dynamic strain aging (DSA) effects, which can give rise to instability of plastic flow and can manifest as serrated flow over a range of rates and temperatures. DSA is associated with interactions between dislocations and solute atmospheres and has previously been reported in C103 at temperatures less than 900˚C at 10^{-2} s^{-1} [93], but has not been actively studied for the other alloys, which also demonstrate this plateau (not presented in Figure 3.3). The ST model is not able to describe this abrupt plateau (rate and temperature independence) in the flow stress. However, it is contended that this plateau region occurs at such low temperatures that Ni-based superalloys would typically be favored over refractory alloys. As such, the ST models were only fit to higher temperature data, and this is demonstrated by truncating the curves in Figure 3.3 near the start of these plateaus.

Table 3.3. *Sellars-Tegart Model Parameters and their Respective Standard Deviations*

Alloy	***Q* [kJ/mol]**	***n***	***n* Literature**	***α***	**Log(*A*) ***
C103	420 $\pm$ 10	3.3 $\pm$ 0.2	3.0 – 3.9 [73]	0.020 $\pm$ 0.002	8.7 $\pm$ 0.3
WC-3009	300 $\pm$ 100	2.9 $\pm$ 4	3 – 3.8 [62], [69]	0.01 $\pm$ 0.04	6 $\pm$ 1
C-129(Y)	280 $\pm$ 10	3.8 $\pm$ 0.4	3 [69]	0.008 $\pm$ 0.001	5.4 $\pm$ 0.5
Cb-752	410 $\pm$ 20	3.3 $\pm$ 1.2	3.3 [75]	0.014 $\pm$ 0.01	7.7 $\pm$ 0.7
D-43	410 $\pm$ 20	5.1 $\pm$ 0.8	5.5 [76]	0.007 $\pm$ 0.003	8.9 $\pm$ 0.7
FS-85	520 $\pm$ 20	3.5 $\pm$ 1.1	2.6 – 4.4 [75]	0.019 $\pm$ 0.01	10.0 $\pm$ 0.7
ASTAR-811C	450 $\pm$ 20	3.0 $\pm$ 0.8	3.4 – 6.7 [77]	0.013 $\pm$ 0.006	8.5 $\pm$ 0.9
TZM Stress Relieved	650 $\pm$ 80	2 $\pm$ 1	3.4 – 4.7 [79], [104]	0.02 $\pm$ 0.01	14 $\pm$ 3
TZM Recrystallized	720 $\pm$ 60	4 $\pm$ 1	0.4 – 3.0 [36], [78]	0.02 $\pm$ 0.02	16 $\pm$ 2
MAR-M247	550 $\pm$ 16	6.1 $\pm$ 0.5	7.4 – 8.6 [81]	0.0029 $\pm$ 0.0003	17.2 $\pm$ 0.8
Haynes 230	390 $\pm$ 30	5.3 $\pm$ 0.4	3.4 – 5.2 [80]	0.003 $\pm$ 0.001	15 $\pm$ 2

* Log(*A*) reported because bootstrapping revealed that A is log-normally distributed

Qualitatively, a comparison between the experimentally determined steady-state flow stress and the ST model predictions reveal the veracity of the Zener-Holloman parameter approach as a means of combining the effects of temperature and strain rate (Figure 3.4). Parametrically, the transition from power-law creep to thermally activated plasticity (power-law breakdown) (i.e., the break from linearity) on this log-log plot is controlled by the parameter α in the ST expression and is delineated by the dashed black line (where $\alpha\sigma = 1$) in Figure 3.4 [107]. Being aware that this transition to higher strain rate dependence exists can be insightful for materials selection and for developing proper expectations for component performance at a given rate and temperature. However, analysis of the bootstrapping results reveals that most of the ST fitting parameters are highly correlated, determined through calculating the respective Pearson correlation coefficients (*r*), reported in Table 3.4. A *r* value close to unity indicates a significant correlation between the two respective variables and the sign of *r* informs on the nature of the relationship (i.e., a negative *r* corresponds to an inverse relation). A lower level of correlation between parameters is obviously preferred, as it not only simplifies the fitting process, but it allows for a clearer understanding of each individual parameter. It is noted that, α and Q are highly, positively correlated and α and n are strongly negatively correlated. Future work should seek relationships involving fewer coefficients which also provide physical insight.

Table 3.4. *Pearson Correlation Coefficients (r) for Each Parameter Pairing in Equation 3.10*

r	***Q***	***n***	***α***	***Log(A)***
Q	--			
n	-0.80	--		
α	0.69	-0.88	--	
Log(A)	0.19	0.32	-0.28	--

Figure 3.4 also shows two specific areas of concern for alloy FS-85; the model slightly overpredicts the flow stress, i.e., is nonconservative, at the lowest rates (below 10^{-8} s^{-1}), whereas the opposite is true at the lowest temperatures. An engineering design constraint that might be employed for numerous high-temperature, single-use applications, such as rocket engines, is restricting permanent strains to 1% in 10 hr, which equates to a strain rate of approximately 3×10^{-7} s^{-1}. At this rate, the ST model describes the data well. For both alloys presented in Figure 3.4, the ST model fails to capture the data at the lowest temperature and highest strain rates, where the aforementioned plateau is observed. Again, this limitation of the model validity, due to deformation mechanism shift, is not a serious concern because it occurs at temperatures where Ni-based superalloys would most likely be favored over higher cost Nb-alloys.

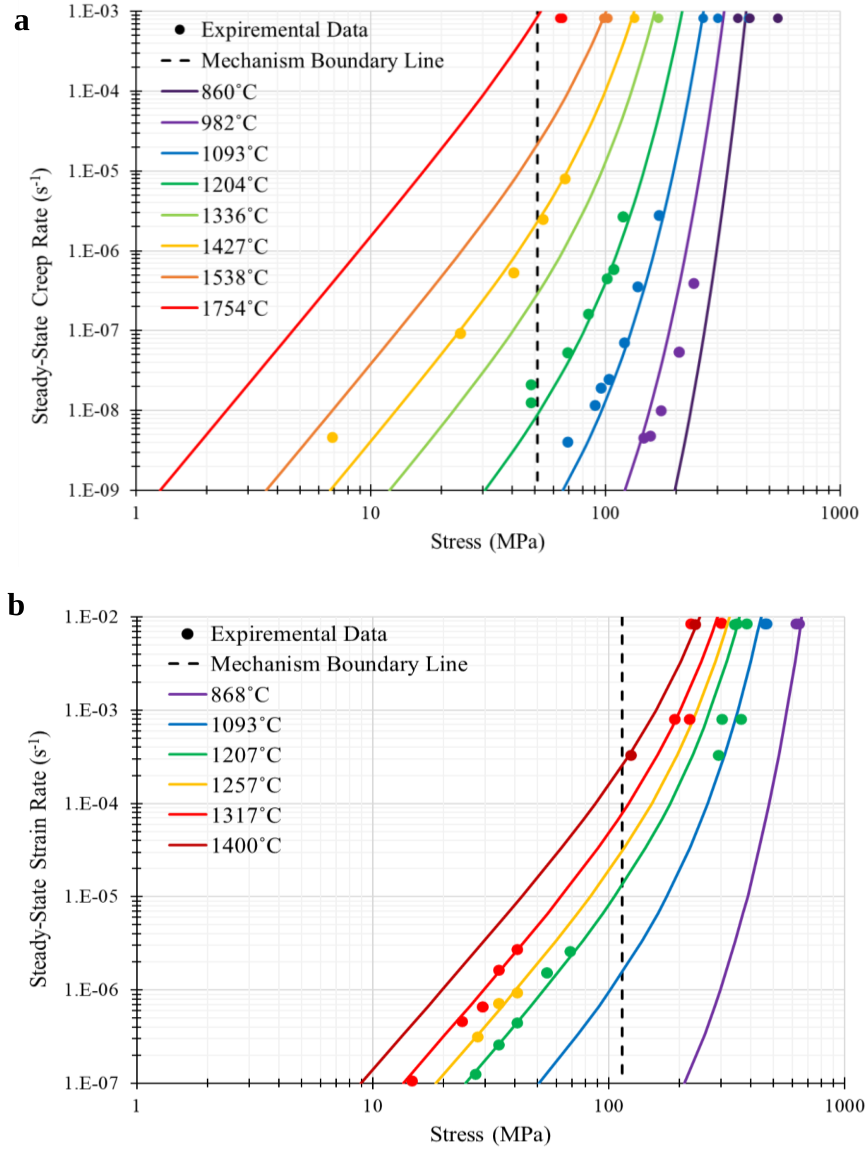

Figure 3.4. *ST predictions align well with experimental data for (a) FS-85 and (b) alloy WC-3009. It is noted that the predictions fail to perfectly describe the extreme conditions for FS-85, where the discrepancies are nonconservative at the lowest strain rates and conservative at the lowest temperatures. The onset of power-law breakdown occurs to the right of the dashed line, where behavior deviates from linearity on the log-log plot.*

3.2.3 Melting Points

The reported melting points (T_m) in the literature are in general agreement with the liquidus (T_L) and solidus (T_S) temperatures predicted by Thermo-Calc (Table 3.5), except for alloy D-43, where the literature melting point is ≈100˚C larger than T_L. Literature did not discuss the methods in which alloy melting points were measured. Additionally, only [28] reported the uncertainty associated with the melting point of C-129(Y) ($\pm$ 50˚C). It is noted that alloy WC-3009 has the lowest T_L and T_S, due to its large concentration (30 wt%) of relatively low melting temperature Hf, and FS-85 has the highest values because of its high concentration (28 wt%) of high melting Ta (the melting points of constituent elements are tabulated in Appendix E).

Table 3.5. *Liquidus (T_L) and Solidus (T_S) Temperatures According to Thermo-Calc (HEA3 v.3.1 database) and Literature Reported Melting Points (T_m) of the Considered Nb-Alloys*

Alloy	T_L (˚C)	T_S (˚C)	T_m (˚C) in Literature
WC-3009	2337	2222	N/A
C103	2413	2368	2350 [82]
C-129(Y)	2464	2407	2400 [28]
Cb-752	2488	2443	2425 [82]
D-43	2498	2453	2593 [30]
FS-85	2611	2560	2591 [82]

3.3 Discussion

3.3.1 Mechanistic Observations

All the selected Nb-alloys except D-43 have stress exponents close to 3, whereas that of D-43 is over 5 (Table 3.3). Stress exponents inform on the rate controlling creep mechanism, where alloys with a stress exponent of 3 suggest that the rate controlling mechanism is drag on the moving dislocations, either by solute or precipitates within grains [50]; this is described as Class 1 or Class A behavior [69]. These alloys also tend to exhibit limited primary creep, with their creep curves consisting mainly of secondary and tertiary creep, which allows the modified LMP approach denoted LMP* to be used to describe the creep-life of this class of material. Primary creep is normally associated with the development and stabilization of dislocation structures within the material. Class 2 or Class M materials are characterized by well-defined primary, secondary, and tertiary creep regimes and a stress exponent near 5 (and some will exhibit even higher apparent stress exponents due to so-called threshold stress effects). As demonstrated in Appendix A, the modified LMP expression can only be used to describe portions of the creep-life of Class 2 materials.

Wadsworth and Nieh noted that Hf-containing alloys, C103, WC-3009, and C-129(Y) exhibit Class 1 (Class A) behavior due to the large atomic size mismatch between Nb and Hf [69]. Based on published creep curves and stress exponents near 3, Cb-752 and FS-85 should also be classified as Class 1 (Class A) alloys. Mohamad [108] and Mukherjee [109] employed an equation proposed by Friedel [110] that defines the binding energy, W, and corresponding stress, σ, required to break dislocations free of the solute atoms that restrict their motion in binary solid-solution alloys (Equations 3.11–3.16). This "breakaway stress" depends on solute concentration (c, at%), temperature (T), Burgers vector (b), Boltzmann's constant (k), and binding energy (W), which further depends on Poisson's ratio (v, assumed to be that of pure Nb [111]), shear modulus (G, calculated from temperature-dependent Young's moduli (Chapter 4) and an assumption of isotropy), and atomic volumetric size difference (ΔV). ΔV was determined through Equation 3.12, where Ω_{alloy} is the atomic volume of the alloy calculated via Vegard's law (i.e., a RoM approach, Equation 3.13); when applicable, the effective atomic volume was used for Hf, Zr, and Ti, assuming a Nb-matrix ([112]) to account for the immiscibility of Group 4 metals in Groups 5 and 6. The temperature dependent Burgers vector of each alloy was calculated using the corresponding room temperature lattice parameter (a_0) determined from Ω_{alloy} (Equation 3.14) and the CTE values from Chapter 4.2.4 (Equation 3.15).

$$W(T) = -\frac{G(T) \cdot (1 + v) \cdot \Delta V}{2\pi \cdot (1 - v)} \qquad \text{Equation 3.11}$$

$$\Delta V = \Omega_{alloy} - \Omega_{solute} \qquad \text{Equation 3.12}$$

$$\Omega_{alloy} = \sum (c_i \cdot \Omega_i) \qquad \text{Equation 3.13}$$

$$a_0 = \sqrt[3]{2 \cdot \Omega_{alloy}} \qquad \text{Equation 3.14}$$

$$b(T) = \frac{a_0\sqrt{3}}{2} \cdot \left[1 + \left(CTE(T) \cdot (T - T_0)\right)\right] \qquad \text{Equation 3.15}$$

$$\sigma = \frac{W^2 c}{b^3 kT} \qquad \text{Equation 3.16}$$

Breakaway stresses associated with the individual solutes within the alloys were compared with the stresses at which creep tests were performed. For alloys C103, WC-3009, and C-129(Y), the breakaway stresses associated with Hf were above the creep flow stresses, which supports the conclusions of Wadsworth and Nieh [69]. For alloys Cb-752 and FS-85 the breakaway stresses associated with Zr are also higher than all the reported creep flow stresses (within the power-law regime) (Figure 3.5), prompting the conclusion that Cb-752 and FS-85 are also Class 1 materials.

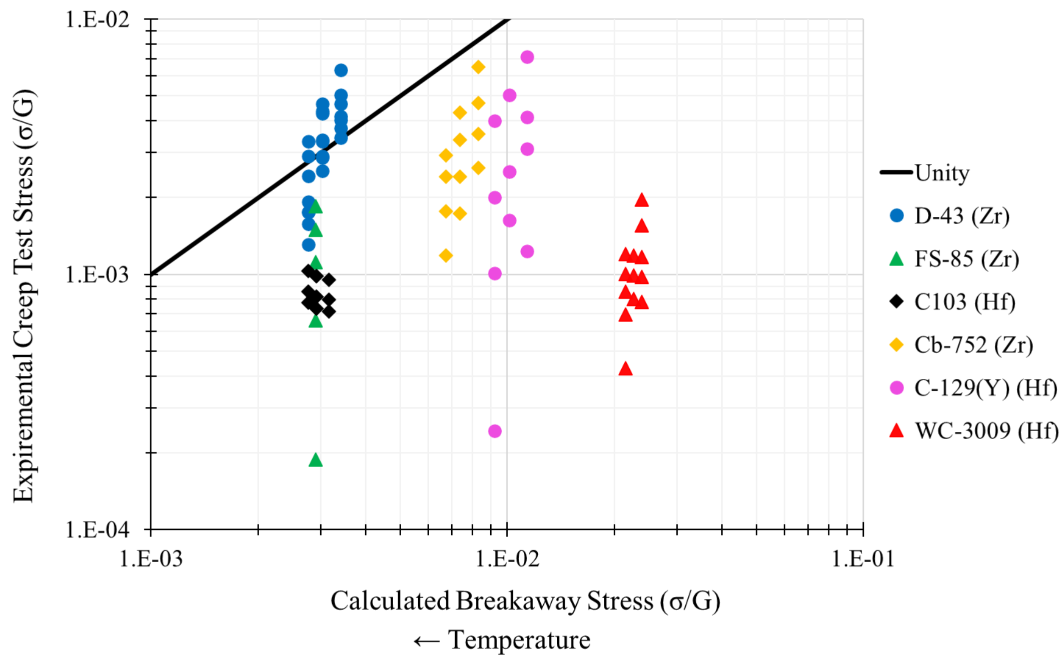

Figure 3.5. *For all alloys but D-43, all experimental creep stresses fall below the respective alloy's breakaway stress, informing that solute drag can occur at these conditions, and this correlates well with the ST stress exponents. D-43 appears not to be governed by solute drag due to its lower alloy content and presence of Zr-carbides, which deplete the matrix of Zr. As breakaway stress decreases, temperature increases relative to the data of each alloy.*

On the other hand, most of the creep stresses sustained by alloy D-43 are larger than the breakaway stress required to separate dislocations from both the W and Zr solute within it. Hence, solute drag is not expected to be rate controlling for D-43. This conclusion is corroborated by the ST fit of n = 5.5 for D-43, where a value of $n \approx 5$ indicates that a dislocation climb and glide mechanism controls the creep, rather than solute drag. Alloy D-43 has slightly lower Zr content than Cb-752 (1 wt% vs. 2.5 wt%), and also has C additions, which getter-Zr atoms from the lattice form ZrC precipitates, further reducing the dissolved Zr within the matrix. In fact, D-43 is the only intentionally precipitate strengthened Nb-alloy investigated in this study, and these precipitates have a significant, positive impact upon the creep resistance. However, the long-term stability of this carbide has not been studied. Precipitate coarsening (increases in particle size at constant volume fraction [112]), including coarsening of grain boundary precipitates [50], which is common in refractory metal alloys, may deleteriously impact the long-term creep performance [67]. It is important to note that although D-43 is shown to behave like that of a Class 2 alloy, the data employed to develop the LMP* trend for this alloy did not include a significant amount of primary creep, allowing the modified LMP expression to still be used.

It is noted that trends observed in flow strengths of various alloys generally correlate with their melting points. For example, the significant Ta content in FS-85 results in the highest solidus temperature. FS-85 correspondingly has superior creep performance relative to lower melting C103 and WC-3009 (Figure 3.2). Alloys FS-85 and D-43 exhibit similar creep responses except at the highest temperatures, where D-43 drops off (Figure 3.2), perhaps due to the aforementioned possibility of precipitate coarsening or carbide dissolution (see Section 3.3.2 below). Creep activation energy has previously been linked to melting points of materials in [19], and the trend of increasing *Q* with increasing melting temperature does hold in the present analysis.

The relatively low predicted solidus (and liquidus) temperature(s) of WC-3009 correlates with its poor creep response relative to FS-85, Cb-752, and D-43 (Figure 3.2). Furthermore, it provides an explanation for why the creep performance of WC-3009 is so similar to that of C103, despite the fact that it has much higher (nearly twice as great) low-temperature strength at strain rates typical of tensile testing. Alloy C-129(Y) is particularly informative, since it has the same Hf content as C103 and W content like WC-3009 (i.e., its composition is intermediate to the other two Hf alloys). At lower temperatures and higher rates, its strength is intermediate, as highlighted later in this document. However, at higher temperatures and lower rates, C-129(Y) is the strongest of the three and this correlates with its higher melting point, in agreement with recent assertions of Senkov et al. [113] who emphasize the correlation between high-temperature yield strength and melting point.

3.3.2 Effect of Heat Treatment on Flow Strength of Nb-Alloys

Stephenson investigated the effect of final anneal temperature on the creep-life responses of Cb-752 and FS-85 [75]. Processing of Cb-752 included various steps of cold working, a penultimate solution-anneal at 1538˚C for one hour, and a final cold-reduction. After that, final anneals at 1318, 1371, 1480, 1593, and 1760˚C were investigated, and the creep resistance increased with final annealing temperature until 1593˚C, while samples annealed at 1760˚C had inferior creep resistance. Similar trends were observed in FS-85. Bewley [99] conducted a study of the effects of this sort, specifically investigating the effect of double annealing schedule on the microstructure of Cb-752. He found that the ZrO_2 along grain boundaries and within the grains of the Cb-752 material began to dissolve as the solution annealing temperature increased, and samples annealed at 1760˚C were nearly single phase, with minimal precipitation along grain boundaries. One hypothesis consistent with these observations is that the oxide precipitates on the grain boundaries promote cavity nucleation. The effect of grain boundary precipitation on creep deformation has been actively studied [50], [114], [115], and materials with grain boundary precipitates often exhibit superior creep resistance to those without. However, materials with large, discontinuous precipitates along grain boundaries can exhibit inferior creep resistance. This suggests that once the precipitates along grain boundaries in Nb-alloys begin to coarsen, they lose their strengthening effect. The presently reported LMP* trends for alloys Cb-752 and FS-85 correspond with creep-life data obtained from samples subjected to the optimal final anneal at 1593˚C.

A 10-minute solution anneal at 1650˚C, 25% cold deformation, and final (aging) anneal of 1 hr at 1427˚C was found to result in the optimal D-43 creep strength [88], [116], [117]. This condition is denoted as D-43M and results in superior creep performance when compared to D-43 samples that have only been treated with an anneal [88]. After the initial solution anneal, some Nb_2C forms along grain boundaries during cooling due to the limited solubility of carbon at low temperatures [117], [118]. The dislocations induced by the cold work act as fast diffusion pathways and heterogeneous nucleation sites that promote formation of a monocarbide phase that forms within the grains during the final aging anneal [89], [119], [120], [121], [122], along with partial recrystallization. A typical microstructure of D-43M includes needle-like Nb_2C carbides with a hexagonal structure along grain boundaries, spherical, face-centered cubic monocarbides dispersed within the matrix, and refined, elongated grains [123]. Of these features, literature cites the fine distribution of the carbides within the matrix as the main reason for the increase in creep resistance of this heat treatment [124], [125]. Because the D-43 carbide dissolution temperature is around 1650˚C [78], [79], it is recommended that D-43M be employed at lower temperatures to avoid a rapid decrease in strength as carbides coarsen and dissolve. Note that materials that are strengthened by a second phase are expected to demonstrate a threshold stress when observing the data in a rate versus stress plot. However, available D-43M data does exhibit this effect [88], [89]. Other carbide strengthened Nb-alloys, such as PWC-11 (Nb-1Zr-0.1C wt%) do evidence such behavior [126]. In order to better understand the behavior of Nb-alloys in general, it is recommended that samples of D-43M be creep tested at low enough stresses to determine if a threshold stress is observed. It is also noted that no high-temperature tensile data has been reported for the D-43M condition, therefore, the ST trend for this alloy was developed by including tensile test data from other processing conditions, including stress relieved, annealed, and welded material, all of which fell onto a singular trend.

Two heat treatment conditions were investigated for WC-3009: 2 hr at 1260˚C [83] and 1 hr at 1317˚C [62]. Data from samples treated for 2 hr at 1260˚C were used to develop the LMP* parameter within this study, as no creep-life data was reported for WC-3009 in the other condition; the ST curve incorporates both conditions. Samples treated at 1317˚C for 1 hr appear to have a slightly improved tensile strength as compared to that of samples treated at 1260˚C for 2 hr, but the differences are small and no steady-state creep data for the 1260˚C annealed condition were reported. Unfortunately, grain size was not reported in either study and could not be accurately assessed from available micrographs. It should also be noted that both materials were reported to have HfO_2 present, but similar to alloy C103, there was no obvious correlation between oxygen content and strength. Wojcik [83] reported data for powder metallurgy samples produced via different routes, resulting in different oxygen concentrations, which ranged from 170–910 ppm, and Titran's material had a rather narrow range of oxygen impurity contents between 200–300 ppm [62].

The LMP* curve for C103 describes a wide range of heat treatment conditions, with annealing temperatures ranging from 1204–1649˚C and annealing times between 1–5 hr, and no prescribed level of cold work was dictated prior to the final annealing [87]. The higher temperature annealing times ranged from 3–5 hr, while the holds employed at the lower temperatures were only one hour in duration. Samples annealed at higher temperatures were creep tested at higher temperatures, while the lower-annealed samples were tested at lower temperatures. It might be expected that the samples annealed at the highest temperatures would exhibit improved creep resistance due to the larger reported grain size (≈60 μm) and the associated resistance to diffusional creep. Nevertheless, these various thermomechanical processing histories gave rise to a single LMP* response, and the ST modeling of C103, which included samples from a wide range of different processing histories and oxygen contents, also yielded a single trend line. This microstructure independence further emphasizes the fact that creep flow is dislocation mediated over the entire range stress-strain rate-temperature conditions considered, and diffusional flow does not seem to be an important contributor.

3.3.3 Rationale for a Minimum Flow Stress Model

The LMP* and ST model predictions are compared in Figure 3.6. Across all alloys except FS-85, LMP* predicts a lower, more conservative strength at the highest temperatures probed; whereas the ST strength prediction becomes the more conservative option at the lowest temperatures examined. The LMP* prediction becomes nonconservative when it is extrapolated to lower temperatures and higher strain rates (outside of the range experimentally assessed) because the underlying mechanism has changed and is no longer properly described by the LMP* model. The mechanism transitions from power-law creep to thermally activated plasticity, also known as power-law breakdown, and is well described by the ST model (Figure 3.3-3.4). Conversely, the failure of the ST model to account for transient deformation renders it nonconservative, especially at temperatures in which the LMP* model predicts the minimum flow stress, as the source of transient creep strain for Nb-alloys is via tertiary (accelerating) creep associated with strain softening. The LMP* model is immune from this type of nonconservatism because, although the basic expressions are based upon steady-state creep descriptions (Equation 3.1), the experimental data employed to parameterize the model (i.e., the amount of time needed to achieve a specific strain level) include any transient creep that may have occurred. Alloy FS-85 is an interesting case because even though it exhibits Class A behavior, it also has a more protracted steady-state creep (i.e., it is more resistant to the softening mechanisms responsible for tertiary creep). For this reason, alloys like FS-85 are competitive for long term applications, such as space nuclear reactors [61], despite the fact that it is denser than some competing alloys (Appendix F). To account for each model's limitations, it is recommended that engineers employ the minimum flow stress from a combination of both models, where ST is used at lower temperatures and higher rates and LMP* is used for higher temperatures and lower rates. Caution must still be exercised when employing the ST model, as its assumption of steady-state deformation always leads to a level of nonconservatism. Moreover, this minimum flow stress model can be proposed in this study only because of the modified LMP expression. In this expression, strain rate can be input, which allows for comparison of flow strengths between the ST and LMP* models. If a material cannot be expressed in terms of LMP*, then this proposed minimum flow stress model should not be used to predict high-temperature flow stress.

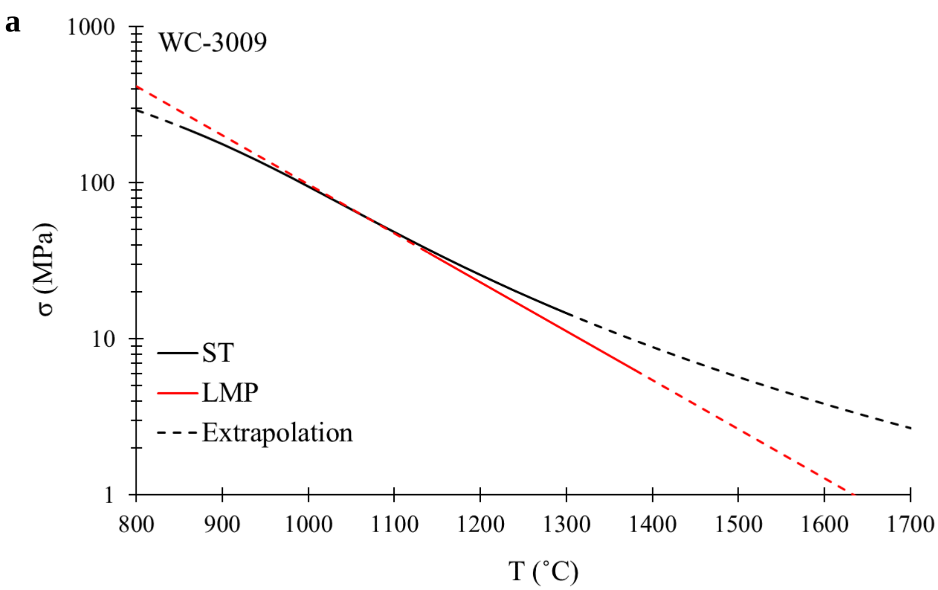

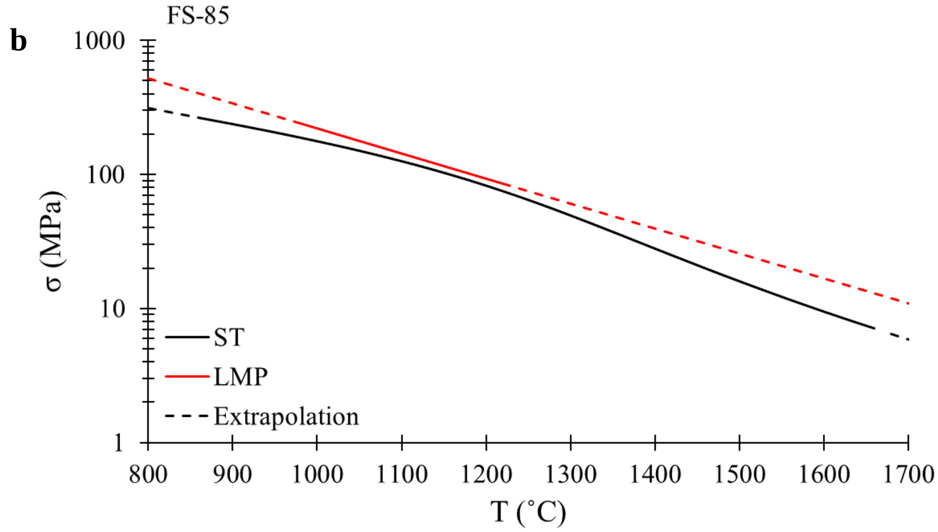

Figure 3.6. *Comparisons between LMP* and ST predicted strength at 10^{-7} s^{-1} for (a) WC-3009 and (b) FS-85. LMP* strength predictions are nonconservative at low temperatures due to extrapolating outside of the high-temperature power-law creep regime tested experimentally and into conditions described by lower activation energies and distinct rate dependencies. Conversely, the ST model is always nonconservative due to ignoring transient creep behaviors.*

A benefit to the proposed models is that they permit comparisons to be drawn between alloys over a range of strain rates and/or temperatures (a complete comparison between alloys WC-3009 and D-43 across a range of rates and temperatures is provided in Appendix G). See Figure 3.7 for a comparison between all the candidate alloys at a strain rate typical of (a) tensile tests 10^{-4} s^{-1} and (b) power law-regime creep tests 10^{-7} s^{-1} (Appendix H contains a similar treatment for the representative Ni-, Mo-, and Ta-based alloys). Amongst the Nb-alloys, WC-3009 is the strongest in the lower temperature regime at 10^{-4} s^{-1} (Figure 3.7), but as temperature increases, the strength of WC-3009 begins to fall off faster than the others. The high low-temperature strength of WC-3009 is attributed to its high, 30 wt%, Hf contents, which become less potent as temperatures increase due to the increased ease of Hf diffusion and the lower melting point it induces [127]. At the highest temperatures, LMP* modeling suggests that WC-3009 has similar strength to C103 (see Figures 3.2 and 3.7). However, it is important to note that no low strain rate studies have been conducted on WC-3009 at T > 1317˚C. Higher temperature creep tests are required to validate the predicted strength of WC-3009 relative to C103, which has been tested up to 1693˚C. Alloys FS-85 and Cb-752 have similar strengths at tensile testing rates and intermediate temperatures. D-43 has a slightly greater strength than Cb-752 and FS-85 due to intentional C additions which give rise to carbide precipitation.

a

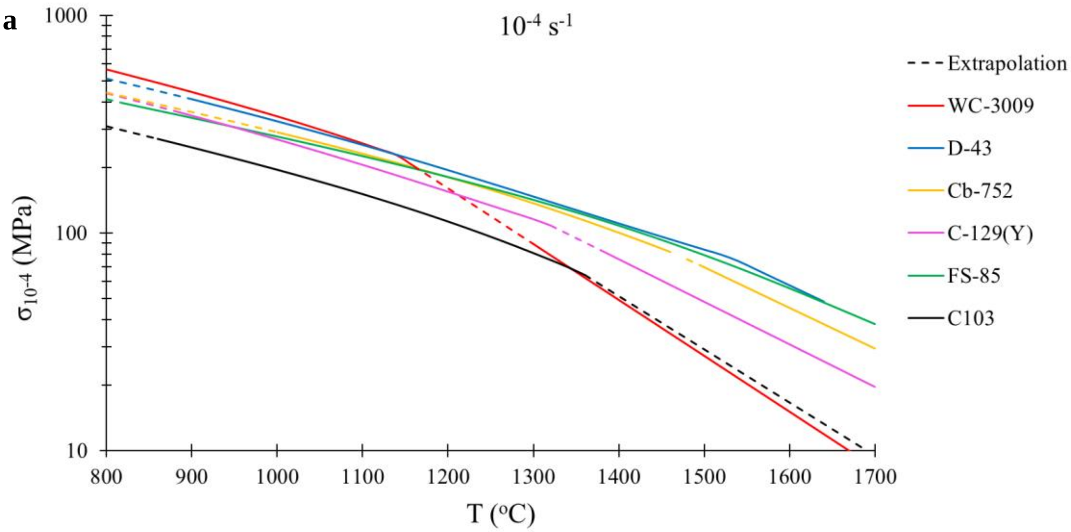

b

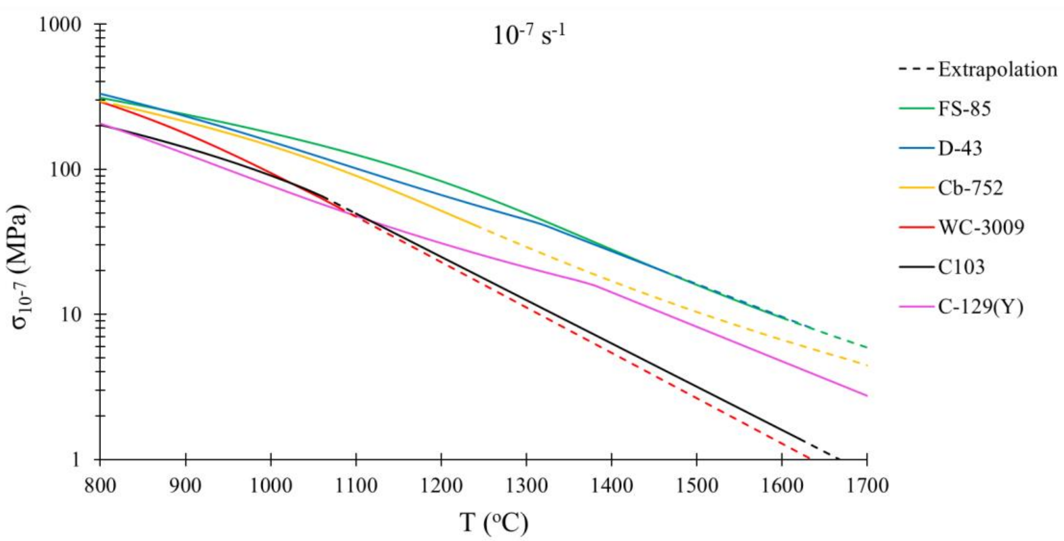

Figure 3.7. *Strain rate is important to consider when selecting a refractory alloy, as some are better suited than others for different rates (i.e., WC-3009 performs significantly better at (a) tensile rates than (b) creep rates). Extrapolations were determined via the bounds of experimental Zener-Holloman values and LMP*s.*

The temperature at which the minimum flow stress transitions from the ST model to LMP* model also correlates with melting point (Figure 3.8). The transition is observed as a discontinuity in the flow stress versus temperature in Figure 3.7 (i.e., stress begins to linearly decrease with temperature) and indicates temperatures above which transient effects (tertiary creep since these alloys exhibit very little primary creep) contributes appreciably to the creep response of the alloy. Nb-Hf alloys transition first (lowest melting points) and FS-85, which has the highest melting point of the alloys investigated, does not transition within the temperatures probed (as in Figure 3.6). Often, grain boundary cavitation is a major cause of tertiary creep, and given the fact that cavitation is controlled by a combination of diffusion and diffusion-controlled dislocation motion [128], the transition temperature will depend upon diffusivity, and therefore, correlate strongly with melting point. Failure to account for this transition would result in the lower melting-point alloys (e.g., Nb-Hf alloys) appearing stronger than they are.

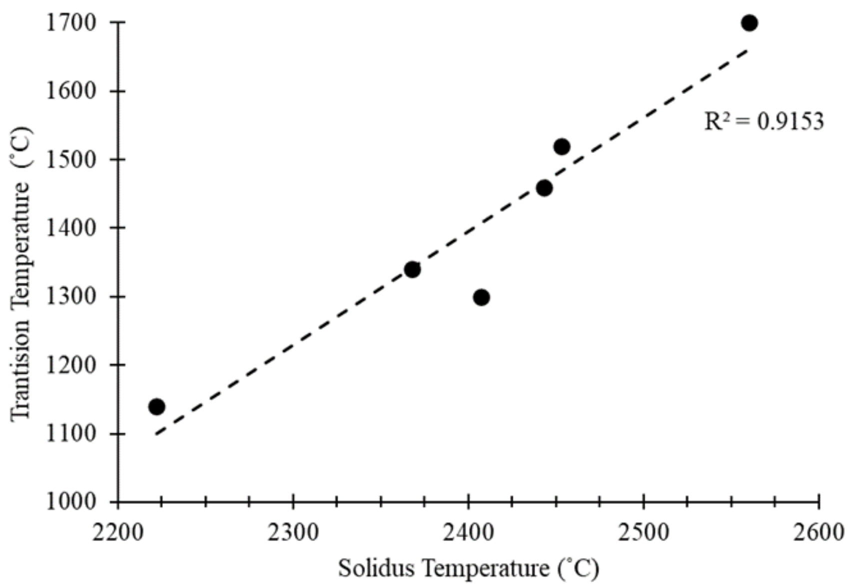

Figure 3.8. *The transition temperature from the ST to LMP* model in the employed minimum strength prediction correlates strongly with alloy melting temperature. Lower melting point alloys begin rapidly losing strength with increasing temperature (i.e., transition to the LMP* model) at lower temperatures relative to higher melting point alloys. Failure to incorporate this transition when modeling the high-temperature strength of materials will result in nonconservatism and an incorrect ranking of materials at the higher temperatures*.

When considering the lower (typical of creep testing) strain rate, 10^{-7} s^{-1}, the flow strengths correlate with alloy melting point. FS-85 is the strongest of the Nb-alloys at lower/intermediate temperatures, and as temperature increases, D-43 has comparable strength to FS-85, which is attributed to the presence of strengthening carbides because the strength of similar (though carbide-free) alloy Cb-752 falls slightly below these alloys. The carbides in D-43 dissolve around 1650˚C, so the modeled strength of D-43 above this temperature is truncated. The strength of D-43 at T > 1650˚C is likely very close to that of alloy Cb-752. At high temperatures, C103 and WC-3009 exhibit similar flow strengths.

Strength-to-density ratios are important to consider in aerospace applications to minimize component mass (see Appendix F for temperature-dependent density calculations). Depending on the application and part geometry, the relevant ratio between strength and density changes. For example, a figure of merit for a strut in tension or column in compression is σ/ρ, but the relevant ratio becomes σ/ρ^2 for a lightweight panel in bending or in-plane compression [129], as presented in Figure 3.9 (see Appendix H for reference alloys' results). The high Ta-content alloy, FS-85, and high Hf-content, WC-3009, drop in rank due to their higher densities. On the other hand, at higher temperatures, the Nb-W-Zr alloys (D-43 and Cb-752) remain top performers (Figure 3.9). Chapter 4 incorporates temperature dependent Young's moduli, the thermophysical properties of heat capacity, thermal conductivity and expansion, along with the mechanical properties investigated in this study to outline a holistic materials selection strategy.

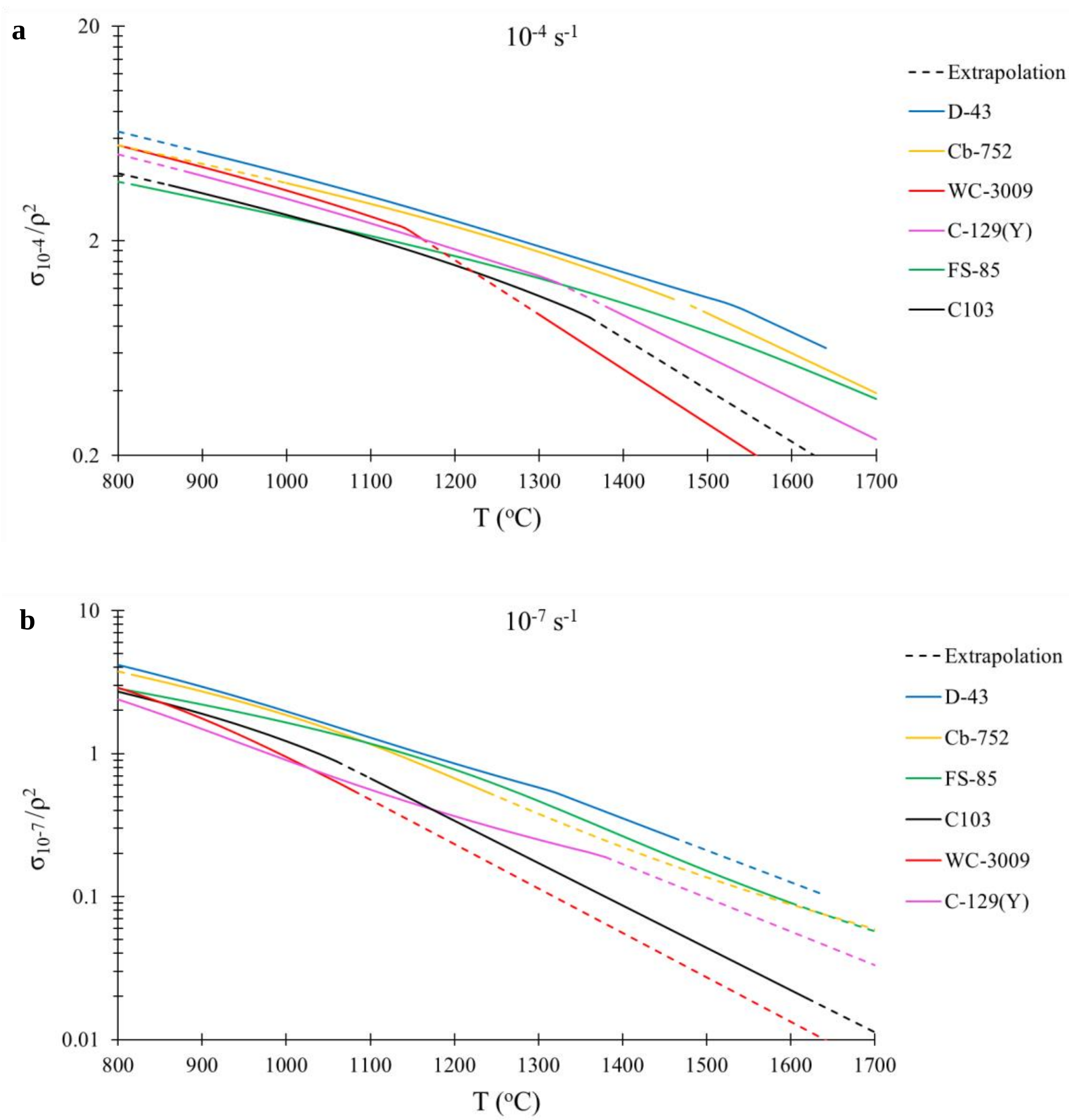

Figure 3.9. *Specific strength indices relevant to the design of lightweight panels reveal that Nb-W-Zr alloys (Cb-752 and D-43) excel at both (a) tensile test and (b) creep-type rates. Extrapolations were determined via the bounds of experimental Zener-Holloman values and LMP*s.*

3.4 Conclusions

1. Review of historical data augmented with new data for Hf-containing alloys, C103 and WC-3009, emphasizes that Nb-alloys are highly strain rate sensitive in the temperature range of interest (>1100˚C) relative to other materials. The viscoplastic nature of these materials *must* be taken into account, rather than assuming the material remains elastic up to a specific stress level.

2. All the Nb-alloys investigated, except D-43, exhibit Class 1 (Class A) creep behavior, indicating creep resistance is controlled by solute drag; Hf and Zr are key additions leading to solute drag. Alloy D-43 has low amounts of Zr, and carbon additions further deplete the matrix of Zr due to the formation of zirconium carbides. Importantly, these carbides significantly enhance the creep strength of alloy D-43 up to temperatures where dissolution and coarsening occur.

3. Thermomechanical processing histories of Nb-alloys affect their creep strength. Generally, the higher the final annealing temperature, the more creep resistant the material. In some cases, second phase precipitate microstructures (including carbides and oxides) are responsible, but in other cases, the reason for these trends is unknown. Interestingly, there is no obvious composition dependence in the creep behavior of C103 or WC-3009 amongst samples containing 170-1500 ppm of oxygen.

4. A unified understanding of both creep and tensile testing modalities is provided by the classical Sellars-Tegart (ST) model, which bridges low stress, power-law behavior (creep) and higher stress power-law breakdown (thermally activated plasticity).

5. One of the characteristics of the Class 1 (Class A) type creep behavior of refractory metal alloys (evidenced by all of the Nb-alloys investigated, including D-43) is an absence of significant primary (decelerating) creep and a preponderance of tertiary (accelerating) creep. Fortunately, the rate of acceleration is modest, which enables a *modified* Larson-Miller parameter (LMP*) that describes the time (creep-life) to achieve *any* strain level (within bounds), rather than only yielding a curve describing the creep-life at a single strain level or rupture.

6. Models based upon steady-state flow, such as the ST model, are always nonconservative since they exclude contributions of transient responses (i.e., primary or tertiary creep). Creep-life approaches such as the LMP and modified LMP (LMP*) model, on the other hand, account for such transients, but cannot account for changes in mechanism if they are extrapolated to temperatures below those at which the empirical testing was performed. *A minimum flow stress approach is proposed to mitigate the risks associated with use of either modeling approach independently*.

7. The transition temperature between the ST and LMP* models within the minimum flow stress approach (and the strength at high temperatures) are strongly correlated with alloy melting point.

8. At strain rates typical of tensile testing (e.g. 10^{-4} s^{-1}) and temperatures below ≈1100˚C, WC-3009 is the strongest Nb-alloy considered. At higher temperatures and lower rates (e.g., 10^{-7} s^{-1}), the strength advantage of WC-3009 disappears, and it is predicted to have a strength similar to C103. The relatively low melting point of WC-3009 correlates with this rapid decrease in strength.

9. When normalizing strength by density, heavier alloys such as FS-85 and WC-3009 drop in the ranking, but the Nb-W-Zr alloys (i.e., Cb-752 and D-43) assume a top ranking across the entire range of strain rates investigated.

Chapter 4: Thermophysical Modeling of Niobium-Alloys Informs Materials Selection and Design for High-Temperature Applications

The work in this chapter is currently in preparation for publication. As the lead author, I performed a majority of the data collection from literature and the final analysis of data gathered (i.e., of those via literature and those provided by collaborators). As lead author, I also completed the writing, reviewing, and editing of this work. The additional contributing authors and their roles within this study are as described below:

i. Alex T. Wang (Materials Science and Engineering, University of Virginia, Charlottesville, VA) assisted in gathering data within literature as well as also developing preliminary model fits.
ii. Dr. Noah R. Philips (ATI Specialty Alloys & Components, Albany, OR) provided specific room and elevated temperature experimental data that was lacking in literate including: (i) C103 specific heat capacity, (ii) C103 thermal conductivity, (iii) C103 elastic modulus, and (iv) C103 coefficient of thermal expansion data. These data were used in subsequent analysis. Dr. Noah R. Philips also provided insights into results and modeling techniques, and reviewed and edited the paper.
iii. William T. Riffe (Materials Science and Engineering, University of Virginia, Charlottesville, VA) conducted the room temperature thermal conductivity measurements (TDTR and SSTR) of cast and as-printed WC-3009, high RRR pure Nb, and cast C103, as well as the high-temperature thermal conductivity measurements (TDTR) of cast and as-printed WC-3009.
iv. Dr. Daniel E. Matejczyk (Aerojet Rocketdyne, an L3 Harris company, Los Angeles, CA) provided guidance and insights with respect to results and modeling techniques.
v. Dr. Jonathan M. Skelton (Materials Science and Engineering, University of Virginia, Charlottesville, VA) provided guidance with respect to results and modeling techniques,
vi. Dr. Patrick E. Hopkins (Mechanical and Aerospace Engineering, University of Virginia, Charlottesville, VA) oversaw the thermal conductivity measurements conducted at the University of Virginia.
vii. Dr. James M. Fitz-Gerald (Materials Science and Engineering, University of Virginia, Charlottesville, VA) served as the main Principal Investigator of the grant that funded this work and assisted in editing the paper.
viii. Dr. Sean R. Agnew (Materials Science and Engineering, University of Virginia, Charlottesville, VA) assisted in the writing, reviewing, and editing of the paper, as well as provided guidance on the conceptualization of the study and analysis.

Prior to selection for an application, it is important to consider the combined effects that various properties will have on the performance of the material. A typical approach involves performance indices (PIs), which are metrics designed for general applications with specific constraints and combine various constitutive relationships, as initially championed by Ashby in [129]. A high PI value indicates that the material is well-suited for the given application [127]. In the context of high-temperature applications, a PI that incorporates thermophysical (thermal conductivity and CTE) and mechanical (strength and elastic modulus) properties was developed, with the goal ranking Nb-alloy performance across a range of temperatures. Specific heat capacity is also relevant as it is often required to compute thermal conductivity from experimentally obtained data. In order to make this comparison, the temperature dependence of each property, for each Nb-alloy, was gathered from the currently available literature. Gaps in the data were filled using physics-based empirical models of the temperature dependencies of each of the properties, which enable constrained interpolation and extrapolation.

4.1 Analytical and Experimental Methods and Sources of Data

4.1.1 Specific Heat Capacity

Specific heat capacity data for these alloys was limited. Data was only found for a few temperatures for three alloys: C-129(Y): [28], Cb-752 [29], [130] and D-43 [30]. The current study obtained specific heat capacity measurements for C103 via differential scanning calorimetry (DSC). A Netzsch Heat Flux –DSC 404 instrument was used in accordance with standards DIN EN 821-3 and DIN51007, with forged bar samples adhering to ASTMB654/B655 [131], stress relieved at 1093˚C, with a 5 mm sample diameter.

The property model calculator feature within Thermo-Calc (HEA3 v.3.1 database) was also used to gather molar heat capacities of the alloys (J/mol·K), which were converted to specific heat capacity (J/g·K) via the molar volumes and densities also reported by Thermo-Calc. The freeze-in temperature for each alloy was determined via rounding the alloy’s solidus temperature down to the nearest hundred of a degree. The results of Chapter 3.2.3 are repeated here for convenience (Table 4.1).

Although there is a lack of experimental data for Nb-alloy specific heat capacities, and broadly, thermophysical properties (to be discussed in subsequent sections), Thermo-Calc remains an applicable tool to understand these properties due to its fundamental concept. Thermo-Calc is a CALPHAD (CALculation of PHAse Diagrams) technique, meaning that it develops empirical polynomial relationships to describe the free energy of each phase within specific binary and ternary systems [132], [133]. Groups of similar alloying systems are collected into databases, meaning that the phases in these databases are thermodynamically well-understood. These empirical relationships can then be employed and extrapolated to understand the thermodynamic properties of the same phases present in alloying systems where high-quality experimental data does not exist for [132]. Therefore, the lack of data for these Nb-alloys does not inhibit the use of Thermo-Calc to understand their thermophysical properties and is henceforth utilized in subsequent sections of this thesis.

Table 4.1. *Liquidus (T_L) and Solidus (T_S) Temperatures According to Thermo-Calc (HEA3 v.3.1 database) and Literature Reported Melting Points (T_m) of the Considered Nb-Alloys*

Alloy	**T_L (˚C)**	**T_S (˚C)**	**T_m (˚C) in Literature**
WC-3009	2337	2222	N/A
C103	2413	2368	2350 [82]
C-129(Y)	2464	2407	2400 [28]
Cb-752	2488	2443	2425 [82]
D-43	2498	2453	2593 [30]
FS-85	2611	2560	2591 [82]

4.1.2 Thermal Conductivity

Elevated temperature thermal conductivity measurements were found in the literature for all the Nb-alloys of interest except for WC-3009 [29], [30], [134], [135]. Therefore, thermal conductivity measurements up to 500˚C were conducted for as-cast and laser powder bed fusion (LPBF), additively manufactured samples of WC-3009, which were available. Room temperature measurements were conducted via time-domain thermoreflectance (TDTR) and steady-state thermoreflectance (SSTR), and elevated temperature measurements were done through TDTR alone. TDTR is a contactless, pump-probe laser thermometry technique that is well suited for extracting thermal properties of thin films and bulk materials. A pulsed laser is split into pump and probe paths, with a mechanical delay stage used to adjust the temporal delay between the arrival of the pulses at the sample surface. Through changing the time delay between the arrival of pump and probe pulses, the thermal decay in the material can be directly measured. Fitting this decay, with the cylindrical heat equation, allows thermal conductivity to be determined [136], [137]; a more in-depth description of TDTR is provided in Appendix I. The specific heat capacity of WC-3009 predicted via Thermo-Calc was used in this calculation. It is important to note that these thermal conductivity measurements are accompanied by significant uncertainty due to the individual uncertainties associated with all components factored into the calculation [138]; this uncertainty can range from 5 to 20% [139]. Thermal conductivity measurements of a C103 forged disc with a 12.6 mm diameter and 2.5 mm thickness are also included in this study; samples conformed to ASTMB654/B655 [131] and were stress relieved at 1093˚C. Laser flash analysis was used to standard DIN EN 821-2 with a Netzsch Laser Flash Apparatus LFA 247 instrument.

To model the temperature dependence of the thermal conductivities, a Smith-Palmer type equation (Equation 4.1) has been found applicable to aluminum at temperatures >500 K (>227˚C) [140] or for concentrated alloys. *A* and *B* are material constants, L_0 is a universal constant, *T* is temperature in K, ρ_r is electrical resistivity, and κ is thermal conductivity (W/m·K) [141]. Resistivity data for these alloys is scarce in the literature, therefore, Matthiessen's rule was used to describe the temperature dependence of the resistivity (Equation 4.2), which consists of additional constants *C* and *D*. Matthiessen's rule assumes that the resistivity of a crystalline metal is the sum of those from individual scattering mechanisms, specifically those due to lattice thermal vibrations and defects within the material [142]. Combining these two equations results in Equation 4.3, where the combined parameters of *A'*, *B'*, and *D'* were used to fit thermal conductivity data.

$$\kappa = \frac{A \cdot L_0 \cdot T}{\rho_r} + B \qquad \text{Equation 4.1}$$

$$\rho_r = C + D\,T \qquad \text{Equation 4.2}$$

$$\kappa = B' + \frac{A' \cdot T}{1 + (D' \cdot T)} \qquad \text{Equation 4.3}$$

4.1.3 Elastic Modulus

Room temperature data was found for all of the Nb-alloys of interest [16], [28], [143], whereas elevated temperature elastic modulus data were found for all but WC-3009 (C103: [16], [144]; C-129(Y) [28], [144]; Cb-752 [145]; D-43:[146]; FS-85: [16], [147]). New modulus measurements for C103 in the fully recrystallized condition (1 hr at 1316˚C) at room temperature and 1093˚C were obtained via tensile testing as a part of this study. The test apparatus consisted of an Epsilon model 3648 – HT extensometer and a radiatively heated, all-metal high-vacuum furnace within a 5988 Instron test frame, which provides feedback-controlled crosshead displacement in accordance with ASTM E8 and E21 [70], [71]; results are reported in Table 4.2.

Table 4.2. *Elastic Modulus Measurements of C103 at Room Temperature and 1093˚C*

Temperature ˚C (˚F)	E ± SD (GPa)
RT	106 ± 3
1093 (2000)	94.5

Note that all the gathered high-temperature data except for that of Cb-752 (which was tested via dynamic, ultrasonic methods) were static elastic moduli, determined via tensile tests. Such static moduli are typically lower than dynamic ones because they are prone to include some microplasticity, and this effect is likely to become more severe as the temperature is increased and the material becomes softer. A linear expression (Equation 4.4, T is in ˚C) is used to describe the alloys' high-temperature moduli, where E_0 corresponds to the Young's modulus at room temperature, T_0 = 25˚C, and M corresponds to the alloy's temperature dependence. The method for obtaining fits of M is discussed in a subsequent section.

$$E(T) = E_0 + M \cdot (T - T_0) \qquad \text{Equation 4.4}$$

Physically based, non-linear relationships between elastic moduli and temperature exist (e.g. Watchman [148] and Varshni [149]), but the non-linearity in these models is only significant at cryogenic conditions (see data for pure Nb [10], [150] and Ta [149]), suggesting that the temperature dependence of Young's modulus is linear in the high temperature range of interest. Note that recent studies of a refractory high entropy alloy, HfNbTaTiZr, confirm a linear dependence on temperature within the elevated temperature range of interest [151], as Frost and Ashby in [46] and in the modern Ansys GRANTA software [111].

Another avenue to convince oneself that the evaluated temperature dependence of a material's elastic modulus is linear is to consider fundamental thermodynamics. The Grüneisen parameter (γ) describes the change in vibrational frequencies within a crystal due to a change in volume. Equation 4.5 provides the dependence of the Grüneisen parameter on volumetric thermal expansion (α_V), density (ρ), bulk modulus (either isothermal K_T or isentropic K_S), and heat capacity (constant volume C_V or pressure C_P) [152].

$$\gamma = \frac{\alpha_V K_T}{C_V \rho} = \frac{\alpha_V K_S}{C_P \rho} \qquad \text{Equation 4.5}$$

The Grüneisen parameter itself varies little from one material to the next (being of order unity for most) and exhibits even less variation for a given material over a wide range of pressures and temperatures [153]. Taking pure Nb as an example, γ(300 K) = 1.3645 and γ(3000 K) = 1.3647 [154]. From this, the temperature dependence of elastic modulus (i.e., the bulk modulus) can be understood when considering the temperature dependencies of the other properties within the expression. At temperatures well above the Debye temperature, thermal expansion and heat capacities are relatively constant in most materials (though slight increases with temperature can occur, as will be presented in future sections). Therefore, changes in material density must be compensated via inverse changes of the bulk modulus. Density (i.e., volume) is expected to linearly increase with temperature as explained in [155], which indicates that bulk modulus, and therefore the elastic modulus, must linearly decrease with temperature. This thermodynamic exploration can also explain the nonlinear behavior of elastic moduli at cryogenic temperatures, near absolute zero temperature, as the thermal expansion and heat capacities both approach zero and the moduli asymptote to a constant value, reflecting the near harmonic shape of the interatomic potential when all the atoms in the lattice are near their equilibrium positions.

4.1.4 Linear Coefficient of Thermal Expansion

Linear coefficients of thermal expansion (CTE) collected between 93˚C and 1300˚C were obtained for all alloys but D-43 [16], for which only one, constant CTE value was reported from 540˚C to 1370˚C [30]. In general, the CTEs themselves were found to exhibit a linear temperature dependence [22], [23]. New CTE measurements of alloy C103 were acquired by dilatometry, adhering to DIN 51 045-1 and DIN EN 821-1, with a Netzsch Thermodilatometer DIL402. Measurements were completed on forged bars following ASTMB654/B655 [131] that were 3.8 x 2 x 20 mm in size and stress relieved at 1093˚C.

CTEs and densities (Appendix F) at elevated temperatures for these alloys were also modeled using the property model calculator mode within Thermo-Calc and calculated. Freeze-in temperatures were the same as those used when calculating specific heat capacities. It should be noted that the measured density of a cast WC-3009 sample conducted in accordance with the Archimedes method, ASTM B962-17 [156], resulted in a density of 10.25 g/cm^3, which is significantly higher than 10.1 g/cm^3 reported in [16] or its rule-of-mixtures (RoM) prediction of 10.16 g/cm^3 calculated via Equation 4.6 ([25], where u is atomic mass). This discrepancy may be due to a greater amount of W in the cast sample than specified in the nominal composition (Table 1.1). Thermo-Calc predicts a room temperature density of 10.22 g/cm^3 for WC-3009 at the nominal composition, which is also greater than that of [16] or via RoM. However, it is accepted that density measurements may contain up to 5% error, which encompasses the four measurements of WC-3009 density discussed [157].

$$\rho_{RoM} = \frac{\sum c_i u_i}{\sum \frac{c_i u_i}{\rho_i}} \qquad \text{Equation 4.6}$$

4.2 Results

4.2.1 Specific Heat Capacity

The specific heat capacity predicted by Thermo-Calc inform that the investigated Nb-based alloys all follow a similar trend with temperature (Figure 4.1): a gradually increasing value due to the anharmonic effects upon phonon-phonon and phonon-electron interactions [56]. At lower temperatures, it is difficult to distinguish between the specific heat capacities of C103, Cb-752, and D-43. At higher temperatures, trends in specific heat capacity are inversely related to alloy density; meaning that the denser alloys have lower specific heat capacities, which is expected as C_p is a reflection of the phonon frequency within the alloy [158]. All experimental data have values of the same magnitude as those predicted by Thermo-Calc but for some alloys, the two approaches may fall outside of the 4% error typically associated with specific heat capacity measurements (i.e., C-129(Y), and lower-temperature Cb-752 and D-43 data) [157]. The heat capacities of Ni-, Mo-, and Ta-based alloys can also be found in the literature, but the main reason the values of Nb-alloys are presented here is because it is a necessary step for determining the thermal conductivity of a material (as discussed previously). Uncertainty in alloy specific heat capacity is one source of the large uncertainties in thermal conductivity measurements, as knowledge of heat capacity is required to determine material thermal conductivity.

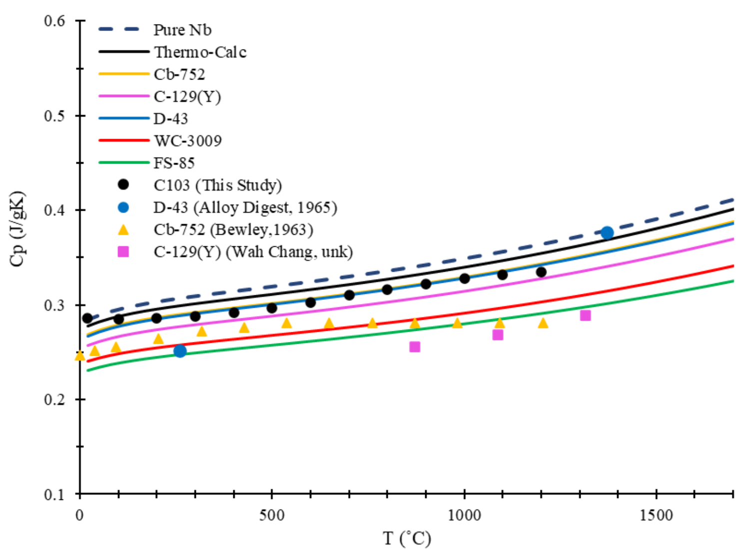

Figure 4.1. *Heat capacities predicted by Thermo-Calc for all Nb-alloys are similar to those experimentally measured for alloys C103, C-129(Y), and Cb-752.*

4.2.2 Thermal Conductivity

When taken collectively, the thermal conductivity data in the literature for all of the investigated Nb-alloys can be described using a singular Smith-Palmer equation (Equation 4.3), as shown by the solid curve in Figure 4.2. In this study, a singular trend was assumed for all Nb-alloys due to the significant scatter in the individual alloy measurements. For instance, thermal conductivity is expected to decrease with increasing alloying content due to the increased electron scattering within the material. The fact that compositionally similar alloys, D-43 and Cb-752, have the largest and smallest thermal conductivities of the presented alloys, respectively, suggests there is significant experimental uncertainty, approaching 20% in some cases. It is concluded that the thermal conductivities of these alloys (excluding WC-3009) cannot be confidently differentiated from each other, as the measurements fall within expected experimental error of one another. Therefore, to determine the *A'*, *B'*, and *D'* parameters for a singular Smith-Palmer equation, Equation 4.3 was fit for each set of high-temperature data reported in Section 4.1.2 (excluding all WC-3009 data). Then, the modeled thermal conductivities of each data set were averaged between 500-3000 K (227-2723˚C, per the applicability of Equation 4.1) and a final fit of Equation 4.3 was performed to obtain *A'*, *B'*, and *D'*, displayed in Figure 4.2 and reported in Table 4.4. Figure 4.2 reveals that the thermal conductivity of Ni-based alloys is significantly inferior to that of refractory metal alloys based upon Nb, Ta, and, especially, Mo.

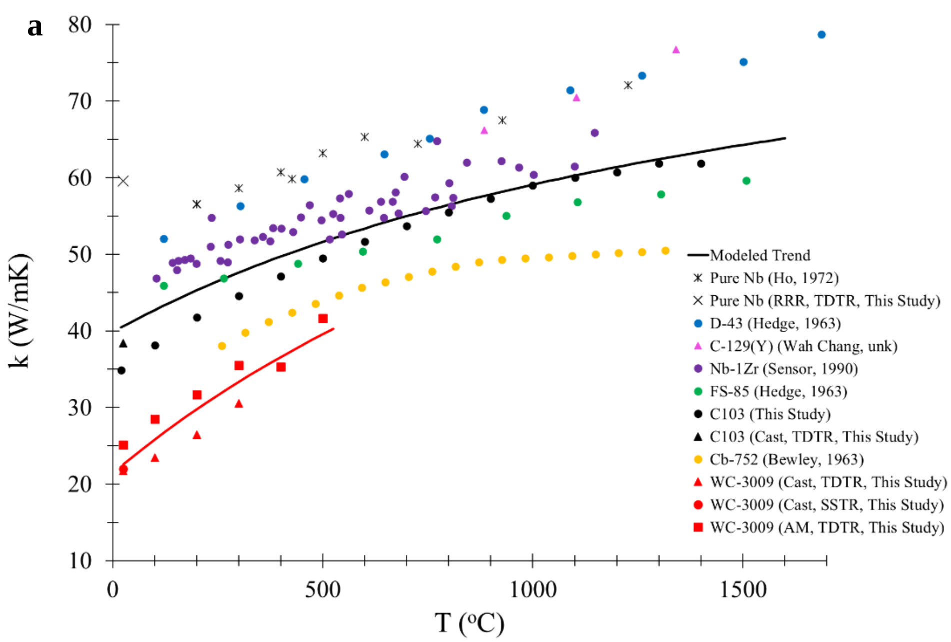

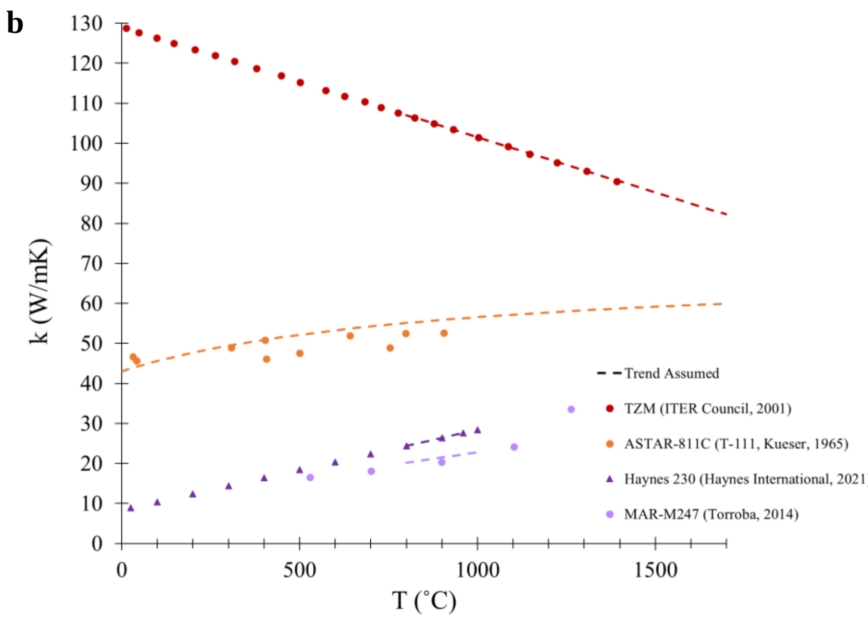

Figure 4.2. *The temperature dependence of the thermal conductivity of (a) Nb- and (b) Ni-, Mo-, and Ta-based alloys. Given the large uncertainty (5 – 20%) in these measurements, it is suggested that there is little composition dependence in the Nb-alloys examined. However, it does appear that WC-3009 has significantly lower thermal conductivity than the other Nb-alloys investigated.*

The thermal conductivity values experimentally measured on WC-3009 samples in this study merit specific consideration, as they are significantly lower than those of the other Nb-alloys. The room temperature thermal conductivity was measured via two different, independent techniques, and resulted in similar values. Additionally, room temperature TDTR measurements on samples of C103 and high RRR (residual resistivity ratio) pure Nb were consistent with (even slightly higher than) literature values. It is assumed that the low thermal conductivity of WC-3009 is due to its large Hf content, as Hf solute additions introduce significant lattice strains which are known to induce electron and phonon scattering. With this in mind, it is interesting that a WC-3009 sample produced via additive manufactured using laser powder bed (AM-LPBF [43]) has a larger thermal conductivity than its cast counterpart. It was expected that the AM sample would have lower thermal conductivity due to the presence of a high crystal defect density and high oxygen impurity content (1400 ppm, measurements made on LECO ONH836, guided by ASTM E1447-22 [159]). This is an important observation since oxygen pick-up during powder processing techniques (and during many high-temperature applications) is somewhat inevitable, as it suggests that the presence of significant oxygen contamination minimally contributes to the low WC-3009 thermal conductivity relative to the intrinsic effects of Hf. One-sample t-tests were conducted at each temperature that WC-3009 thermal conductivity data was collected at to ensure statistical significance of the measurements. Standard errors for this calculation were determined using the individual Smith-Palmer trends for each alloy at each temperature and the mean was the assumed to be the singular Nb-alloy modeled value at that temperature. Results are reported in Table 4.3 and indicate that at all temperatures except 500˚C (by a marginal amount), the thermal conductivity of WC-3009 and the singular Nb-alloy trend are statistically different ($p \leq 0.05$, for 95% confidence).

Table 4.3. *One-Sample t-test Results Comparing Measured WC-3009 Thermal Conductivity Values and the Singular Nb-Alloy Thermal Conductivity Trend*

Test Temperature (˚C)	p-value
RT	0.033
100	0.027
200	0.018
300	0.020
400	0.019
500	0.0504

Therefore, a Smith-Palmer equation was fit for the obtained WC-3009 data and is presented in Figure 4.2 and Table 4.4; the WC-3009 *D'* parameter was assumed to be that of the singular Nb-alloy trend.

Table 4.4. *Equation 4.3 Parameters for the Nb-Alloys Collectively and WC-3009*

Parameter	C103	Cb-752 *	D-43	FS-85	Nb-1Zr	Nb-Alloys	WC-3009
A'	0.057	15.16	0.041	0.012	0.023	0.043	0.066
B'	23.17	-351.16	38.40	40.77	40.02	30.05	6.33
D'	$7.9 \cdot 10^{-4}$	$3.7 \cdot 10^{-2}$	$5.2 \cdot 10^{-4}$	$5.0 \cdot 10^{-5}$	$2.8 \cdot 10^{-4}$	$6.8 \cdot 10^{-4}$	

* It is acknowledged that the Cb-752 trend does not align with the other alloy's fits, but was still used to model Cb-752 thermal conductivities

4.2.3 Elastic Modulus

The experimentally measured room temperature elastic moduli reported in the literature compare well with mole fraction weighted RoM averages, based upon the moduli of the pure constituents (Appendix E). However, when comparing the high-temperature measurements of the alloys, the modern high-temperature C103 moduli presented in this study are significantly higher than those reported in 1962 [142], which are repeatedly cited throughout literature [16], [100] These historical values should no longer be accepted as the true values for C103, as they fall below those of pure Nb despite containing a significant fraction of Hf, a higher stiffness alloying ingredient. Two possible explanations for the observation of low C103 moduli are the possibilities that (i) microplasticity may have impacted the measurement and (ii) the prior measurements may have been conducted on material with a unique crystallographic texture [160]. Other factors within the obtainment process that could affect the measurements (i.e., material composition, testing procedure, or general error within measurements) are not expected to have significantly changed with time such that the observed discrepancies between modern and historical measurements currently exist. Similarly, Nb-1Zr data from the same 1962 study [144] also fall well below the elevated temperature moduli of pure Nb (displayed as the more compliant Nb-1Zr data set in Figure 4.3). Due to these inconsistencies of C103 and Nb-1Zr historical data, the reliability of the C-129(Y) data ([28]) is also in question, as it originates from a similar time frame and lacks supporting methodology information. The modern C103 data reported in this study and data reported for Nb-1Zr in [161] should be accepted as the correct values. Additionally, there is also uncertainty in the high temperature elastic properties of Nb; the range of pure Nb moduli found in literature is included as a gray zone to demonstrate the uncertainty that presently exists regarding the temperature dependence of this fundamental physical property.

The process of determining the temperature dependence for all of the collected high-temperature data sets was initially done via a linear regression of each data set from room temperature to ≈1200˚C; however, no rational trend between the slopes of the various alloys was observed (for example, FS-85 has the greatest temperature dependence although it has the highest melting point of the alloys investigated, see Figure 4.3). Therefore, similar to what was done for thermal conductivity, all of the alloys were assumed to have the same temperature dependence of their elastic moduli. The temperature dependence was taken to be the average dependence across all data sets, excluding the historical C103, C-129(Y), and Nb-1Zr data. The final linear trends employed for the individual alloys were forced to have an E_0 value equal to either the room temperature RoM calculated value or experimental value (final parameters reported for each alloy in Table 4.5).

As elastic moduli are generally insensitive to slight changes in alloying, it is expected that D-43 and Cb-752 will have similar moduli. Room temperature data of alloy D-43 agree well with its RoM calculated modulus, and therefore, the D-43 linear fit was also assumed to hold for Cb-752 in subsequent analyses. It is noted that the temperature dependent trendline is parallel to but higher than the experimentally measured dynamic moduli of Cb-752. A plausible reason for this discrepancy is the possibility that one or both of the experimentally tested materials possessed crystallographic texture. Similarly, C-129(Y) and WC-3009 were assumed to have the same temperature dependent moduli. The experimentally measured room temperature modulus of WC-3009 and its RoM calculation align well with those of C-129(Y), and they are both within the Nb-Hf-W system.

Linear fits of the high-temperature elastic moduli of two representative Ni-based superalloys, and other refractory metal alloys mentioned earlier are presented in Figure 4.3, and the corresponding Equation 4.4 fit parameters are presented in Table 4.5. The temperature sensitivities of the Young's moduli of Ni-superalloys are much greater than the refractory alloys (Nb, Mo, and Ta). Finally, Figure 4.3 highlights the fact that Mo- and Ta-rich alloys have significantly higher Young's moduli than Nb-alloys, and while this may be attractive for some applications, it will be shown to be a liability for applications subjected to steep spatial and temporal temperature gradients.

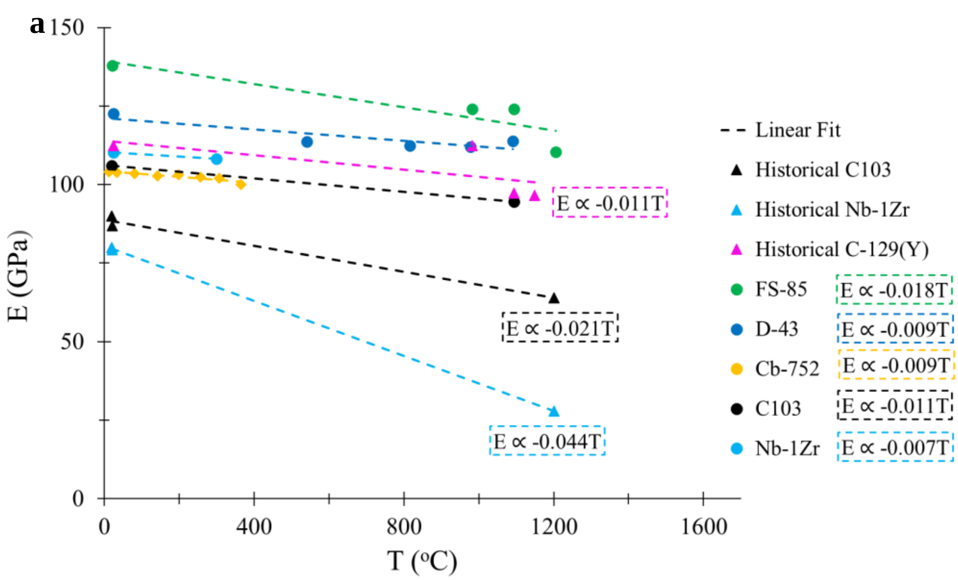

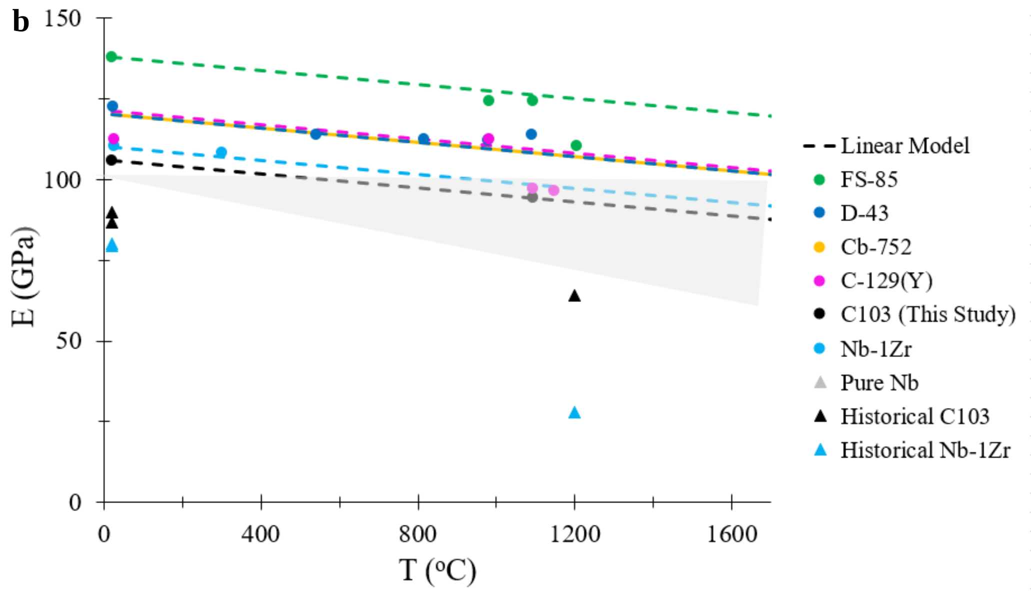

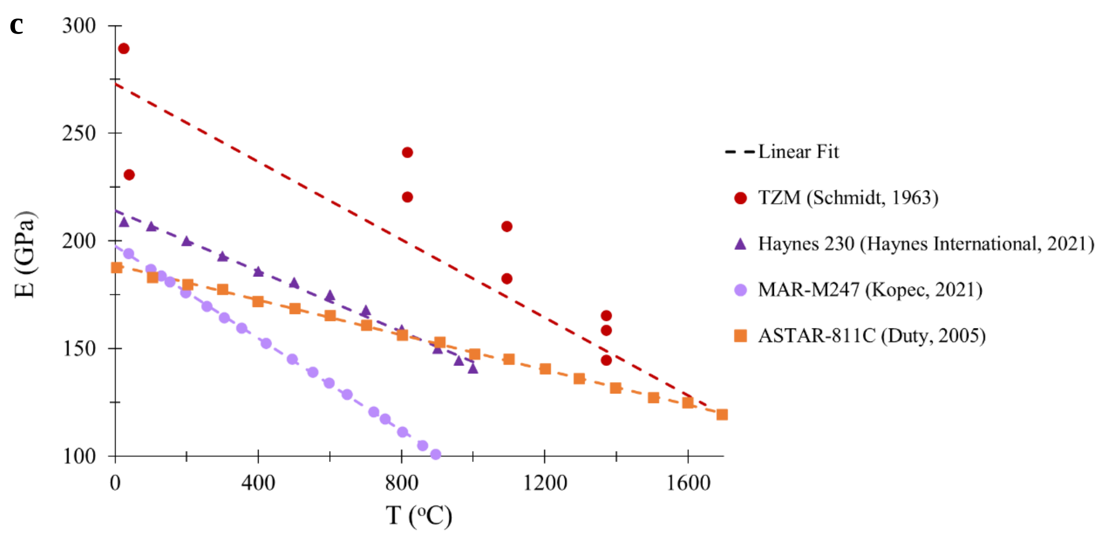

Figure 4.3. *Linear relationships were used to fit high-temperature elastic modulus data for (a) individual Nb-alloys, (b) Nb-alloys assuming the singular temperature dependence, and (c) Ni-, Ta-, and Mo-alloys. WC-3009 was assumed to demonstrate the same trend as C-129(Y) and Cb-752 was modeled with the trend of D-43.*

Table 4.5. *Alloy Fit Parameters for Equation 4.4*

Alloy	$E_{Experimental, RT}$ **(GPa)**	$M_{Experimental\ (RT\text{-}1200^{\circ}C)}$ **(GPa/°C)**	$E_{RoM, RT}$ **(GPa)**	E_0 **(GPa)**	M **(GPa/°C)**
C103	106 (this study)	-0.011	107	106	-0.011
WC-3009	--	--	126	121	
C-129(Y)	112 [28]	--	121		
Cb-752	104 [145]	-0.009	119	120	
D-43	123 [146]	-0.009	119		
FS-85	138 [10], [100]	-0.018	136	138	
Nb-1Zr	110 [161]	-0.007	103	110	-0.007
Haynes 230	209 [32]	--	--	214	-0.070
MAR-M247	194 [162]			198	-0.107
ASTAR-811C [15]	--			189	-0.041
TZM	290 [36]			273	-0.090

4.2.4 Linear Coefficient of Thermal Expansion

Figure 4.4 presents the temperature dependence of the thermal expansion of Nb-alloys. In general, the literature reported values agree well with those calculated by Thermo-Calc (with the HEA3 v.3.1 database and property model feature). Typically, an error of 3% can be associated with CTE measurements, which accounts for the differences in experimental and Thermo-Calc results for all alloys but WC-3009; the observed trend of the measured C103 data from this study is within the 3% error [157]. Interestingly, the thermal expansion of WC-3009 has been experimentally measured to be larger than pure Nb's, but when modeled in Thermo-Calc, it fell between those of pure Nb and Hf, following the rule-of-mixtures, which has been observed to be applicable to bcc high-entropy alloys via first principles density functional perturbation theory and the quasi-harmonic approximation [163]. The presence of oxygen is known to increase the CTE as the formation of oxides generates solvent atom vacancies within the lattice, therefore increasing the expansion of the material with temperature [164]. WC-3009 is known to internally oxidize, which supports the hypothesis that this led to an increase in measured CTE [16]. Temperature dependent densities determined from experimental CTE measurements were reported in Appendix F, which aligned well with those densities obtained from Thermo-Calc. Figure 4.4 highlights the fact that Ni-based alloys generally have higher CTE values than Nb-alloys, and this will be a liability for Ni-alloys employed in applications involving thermal gradients. However, other refractory alloys based upon Mo and Ta typically have even lower CTE values than Nb.

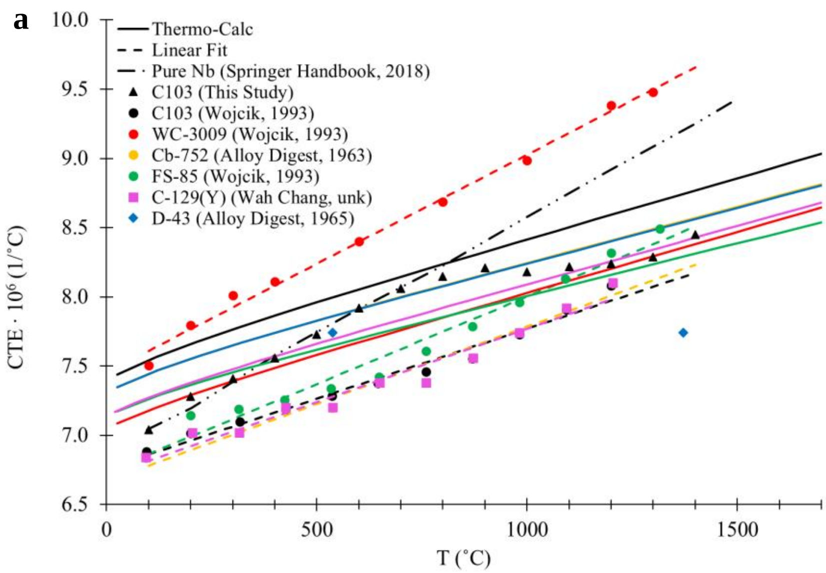

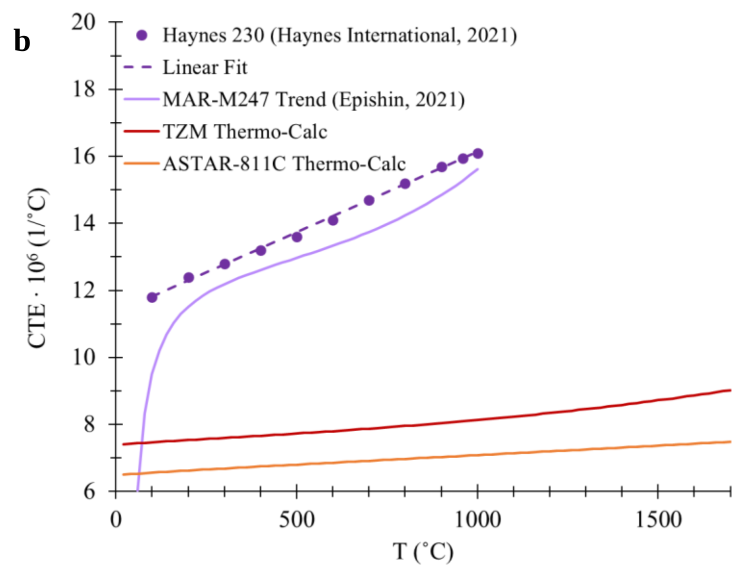

Figure 4.4. *(a) Linear coefficients of thermal expansion predicted by Thermo-Calc for Nb-alloys are similar to those that have been measured experimentally, except for alloy WC-3009 where the experimental data are significantly higher, possible due to internal oxidation. (b) CTE values for competing alloys are both higher (Ni) and lower (Mo and Ta) than those of Nb-based alloys, respectively.*

4.3 Discussion

4.3.1 Trends in Elastic Modulus

To verify the temperature dependencies of the elastic moduli, the reported temperature dependence of pure refractory metals in Frost and Ashby [46] and the GRANTA software [111] were used for comparison. It should be noted that in [46] the temperature dependence is reported for shear modulus, whereas in [111] it is reported for Young's modulus. In these sources, temperature dependence is reported in a different form ($\frac{T_m}{G_0}\frac{dG}{dT}$ in [46], $\frac{T_m}{E_0}\frac{dE}{dT}$ in [111]) than reported in this study. The provided room temperature and modulus values in [46], [111] were used to deconvolute the temperature dependence from the given expression for each metal (see Appendix E for [46], [111] values). When converting shear modulus dependence to elastic modulus, there was minimal difference between the two; this provided a general range of acceptable temperature dependencies. Through linear regression, both the modern C103 and Nb-1Zr data had a temperature dependence within this acceptable range (note that these dependencies were a factor of three smaller than that of the historical respective data reported for the same alloys in 1962 [142]). It was also observed that many of the other alloys exhibit this magnitude of dependence up to approximately 1200˚C (see Tabel 4.4); which was the temperature range used to develop the singular temperature dependence for the Nb-alloys. It is unknown whether the dependence does increase past a critical temperature or if this trend is an artifact of the means of data acquisition.

When evaluating elastic modulus data, it is important to understand the potential effect of crystallographic texture, which can be introduced through processing prior to testing or via the test itself. If the material is textured, then the single crystal elastic anisotropy of the material must be considered. All elemental metals, except W at room temperature, are anisotropic at the single crystal level, meaning that the elastic response varies with direction. In terms of ultrasonic techniques (i.e., dynamic modulus measurements), acoustic waves travel at different velocities along different directions in anisotropic materials. Nb, in contrast with many other metals with cubic crystal structures, is stiffest along <100> directions and the most compliant along <111> directions. Therefore, since the Cb-752 sample was dynamically measured to have a lower modulus than expected, it suggests that the samples may have a <111>-fiber texture component along the direction probed using ultrasound [160]. Close evaluation of the high-temperature experimental data of D-43 reveals that the modulus appears to slightly increase with temperature, which may indicate that the samples are absorbing oxygen during testing [165]. These two observations, along with the previously mentioned discrepancies in the data of alloys C103 and Nb-1Zr further highlight the challenges and the need for modern measurements.

In terms of understanding the trends of the alloys, the fact that FS-85 has the highest room temperature modulus is associated with its significant Ta concentration, which also correlates with it having the highest density and melting point of all the Nb-alloys considered. Similarly, alloys C103 and Nb-1Zr have the lowest modulus values, which correlates with an absence of stiff alloying ingredients such as Ta or W. Moreover, the Nb-W-Zr alloys (Cb-752 and D-43) have intermediate melting points between FS-85 and the Nb-Hf alloys (Chapter 3.1.3), which aligns well with their modulus values, which are also intermediate (Figure 4.3).

4.3.2 Application of Strain Rate Sensitivity

In Chapter 3, the influence of temperature and a constant strain rate on flow stress was discussed, but in some applications, the plastic strain rate is not constant. One such example, which has been discussed at length in Chapter 3, is creep, where the strain rate may be a function of strain (time) even at constant applied stress. Another time dependent material response is stress relaxation. Stress relaxation is expected to occur in applications where a constrained component at elevated temperatures is initially preloaded, and with time, the load within the component decreases, i.e., it relaxes, at a rate controlled by its creep behavior. Stress relaxation occurs because of the applied constraint, as the material is not permitted to strain (denoted in Equation 4.7, where $\dot{\varepsilon}_T$ is total strain rate), and therefore, with time, the elastic strain from the initial preload converts to plastic strain (time dependent plastic deformation), resulting in a decrease of stress. The rate of plastic strain accumulation ($\dot{\varepsilon}_p$) is equal to the loss of elastic strain with time ($\dot{\varepsilon}_e$)). Elastic strain rate is calculated through Hooke's law (Equation 4.8), which depends on the temperature dependent elastic modulus (*E(T)*, from Equation 4.4) and applied stress (σ). Plastic rate is determined through the minimum flow stress model, where the faster rate between the ST (Equation 3.1) and LMP (Equation 3.6) models is used (expressed in Equation 4.9). From this, with a given temperature and initial stress (at *time* = 0), the time it takes for a material to relax to a critical stress can be determined.

$$\dot{\varepsilon}_T = \dot{\varepsilon}_e + \dot{\varepsilon}_p = 0 \qquad \text{Equation 4.7}$$

$$\dot{\varepsilon}_e = \frac{d\sigma}{E(T) \cdot dt} \qquad \text{Equation 4.8}$$

$$\dot{\varepsilon}_p = max\ (\dot{\varepsilon}_{ST}, \dot{\varepsilon}_{LMP}) \qquad \text{Equation 4.9}$$

Simple examples of applications in which stress relaxation is a concern include bolts or other fasteners loosening with time, and this has recently been studied for various Ni-superalloys in the context of aircraft engines [166], [167]. WC-3009 and D-43 were selected for this exercise as they exhibit the greatest difference in creep response of the investigated alloys (see Table 3.3 and Figure 3.3). Conditions to model stress relaxation were chosen such that initially, WC-3009 and D-43 would exhibit the same response, which resulted in the selection of 1150˚C and a "preload" of 225 MPa. It should be noted that per Figure 3.7, these conditions will result in the LMP model mainly describing the response of WC-

3009, whereas D-43 is described by the ST model. Figure 4.5 displays the results and demonstrates that WC-3009 relaxes significantly faster than D-43; for example, it takes WC-3009 approximately 15 hours to lose 55% of its preload, whereas D-43 can sustain this stress for 150 hr. This difference in performance is directly related to the difference in alloy strain rate sensitivities (i.e., the inverse of stress exponent in Table 3.3), where WC-3009 is significantly more sensitive (with a value of ~0.3) than D-43 (~0.2). The larger strain rate sensitivity of WC-3009 informs that it will experience a greater change in stress from a change in rate relative to D-43. This is just one more example where strain rate sensitivity is an important material response to consider when selecting materials to employ in high-temperature applications and one that is accounted for in the proposed minimum flow stress model.

a

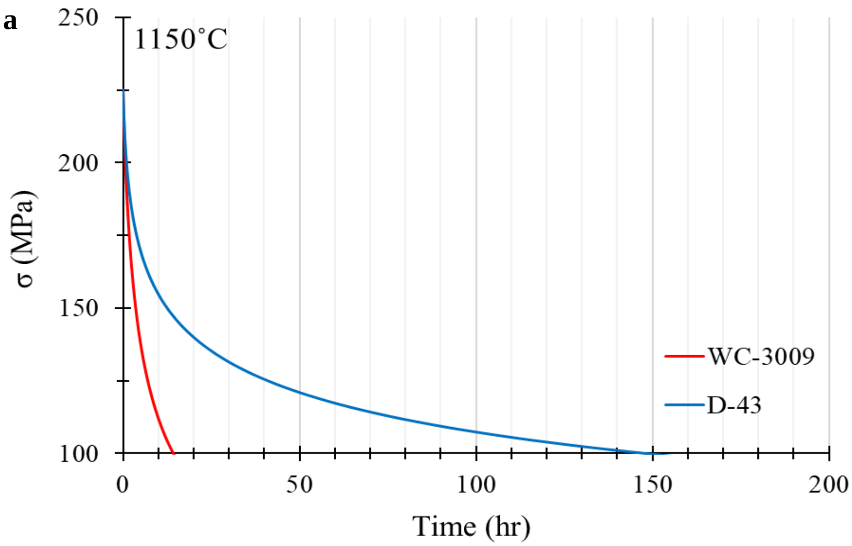

b

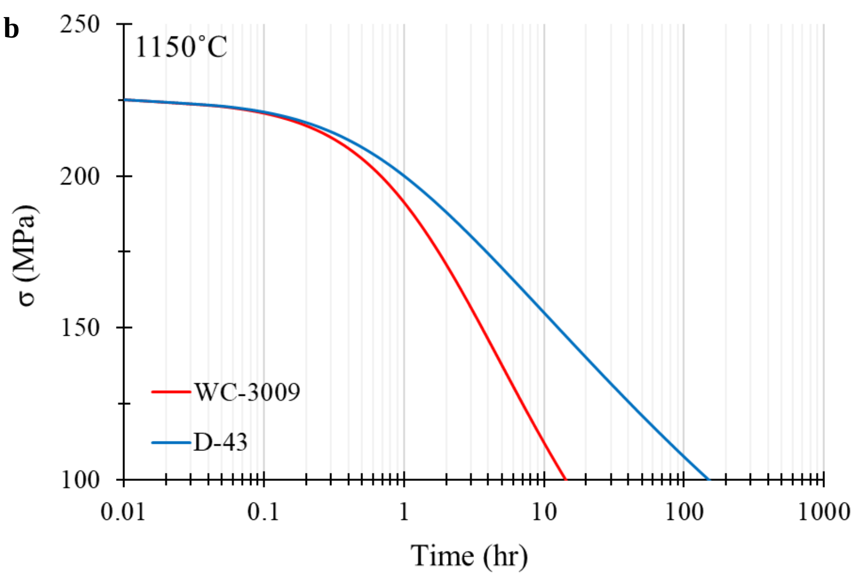

Figure 4.5. *WC-3009 exhibits a more severe stress relaxation than D-43 due to its larger strain rate sensitivity. The expected "exponential-like" decay in stress can be observed in (a) and (b) further highlights the differences between WC-3009 and D-43.*

4.3.3 Combination of Thermal Properties

A performance index (PI) relevant to designing a lightweight plate loaded in bending or in-plane compression (subject to buckling failure) is σ/ρ^2, where σ is the flow stress and ρ is mass density. Resistance to thermal transients is often analyzed through $\frac{\sigma \cdot \kappa}{CTE \cdot E}$ [168], [169], commonly referred to as "thermal shock"; this performance index is proportional to the largest temperature change (or gradient) the material can sustain before a relevant failure occurs. For cases where lightweight planar structures are subjected to thermal transients or steep thermal gradients, Equation 4.10 may be used to rank the performance of potential materials.

$$PI = \frac{(\sigma/\rho^2)\cdot(\kappa)}{CTE\cdot E} \qquad \text{Equation 4.10}$$

Thermo-Calc generated CTEs, the single trendline for the thermal conductivity of Nb-alloys (except for WC-3009), elastic moduli implied by the trendlines in Figure 4.3 and Table 4.5, and minimum predicted flow strengths, as modeled in Chapter 3 are used as input to the PI. Two limiting strain rates were investigated, one representative of a nominal tensile test, 10^{-4} s^{-1}, and that of a typical creep test, 10^{-7} s^{-1} (about 1% strain in 30 hr). Across both strain rates used, the Nb-W-Zr alloys were top performers, due to their relatively high strength, low density, and low CTEs (Figure 4.6). It is important to note that the performance of D-43 is truncated at 1650˚C, as 1650˚C is the dissolution temperature for the strengthening carbides within D-43 [117], [118]. If the minimum flow stress model was not included in this analysis and only the ST model was employed, then C103 would be predicted to have nearly identical performance as Cb-752 at the higher temperatures, which results in the incorrect ranking of materials.

In previous refractory alloy review papers, WC-3009 and FS-85 have been highlighted for their high strength under strain rate conditions typical of high-temperature tensile and creep testing. These reports suggest that these alloys would be key candidates for given aerospace applications [16], [82]. However, these studies fail to acknowledge the fact that other thermophysical properties also play a key role in determining the performance of a high-temperature structural component. Including these properties in the analysis highlights the applicability of Nb-W-Zr alloys to aerospace applications, which have not been highlighted in such a way before. Moreover, including these properties in the analysis also elevates C103, especially at strain rates typical of tensile testing. The strength that C103 lacks relative to the Nb-W-Zr and FS-85 alloys, is made up for via a lower elastic modulus and CTE; all of which serve to reduce the thermal stress a C103 component would be subjected to, improving its performance as a high-temperature structural component. This analysis also demonstrates that alloy WC-3009 is one of the most ill-suited alloys for this hypothetical application, even though it is the strongest alloy at tensile-like rates, as it is consistently one of the lowest performers across the strain rates and temperatures investigated, due to its relatively high density, low thermal conductivity, and low strength at low rates and high-temperatures.

Ni-superalloys were included to further demonstrate their inferior resistance to thermal transients due to their combination of low thermal conductivity and high CTE modulus. Similarly, the Ta-alloy ASTAR-811C is one of the lowest performers specifically due to its high modulus and high density relative to the Nb-alloys, regardless of the high flow stresses it can sustain at elevated temperatures. The Mo-alloy, TZM, is a top-performer in both processing conditions presented; however, as previously discussed, the difficulties associated with fabricability, a high ductile-to-brittle transition temperature (DBTT) and even poor oxidation resistance remove TZM as an alloy for consideration in most aerospace applications.

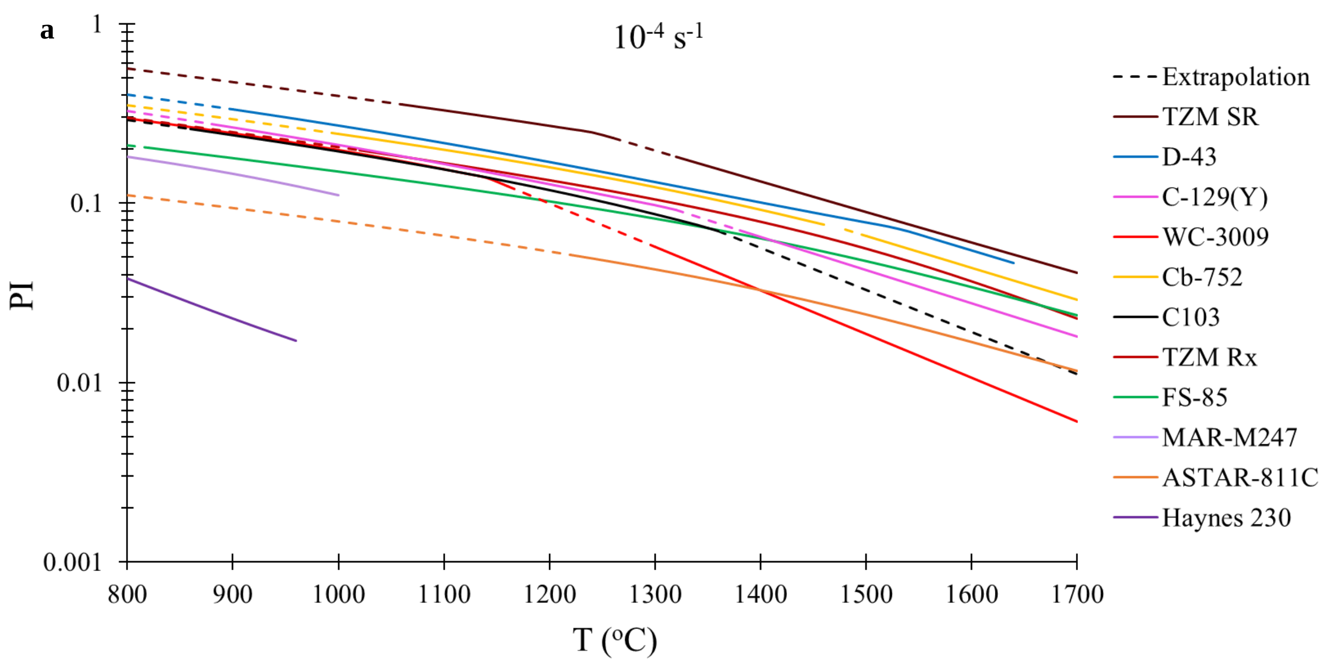

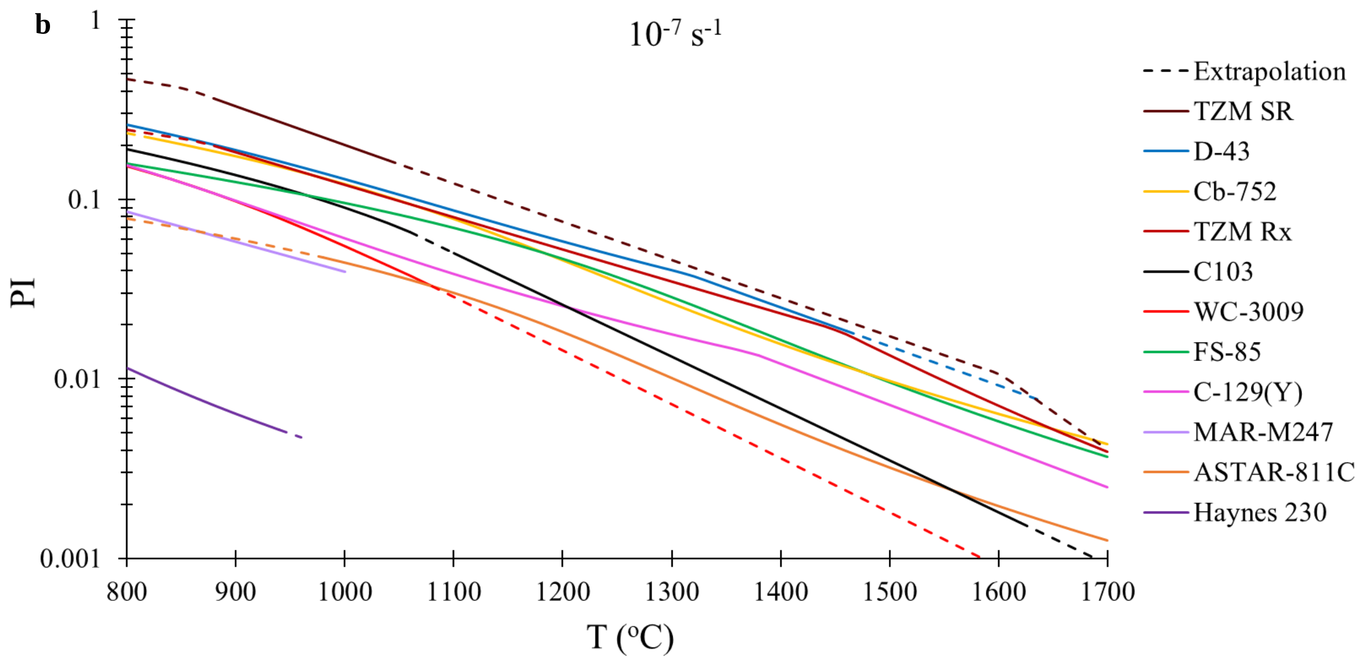

Figure 4.6. *Nb-W-Zr alloys perform best in this performance index at both (a) 10^{-4} s^{-1} and (b) 10^{-7} s^{-1} due to their relatively high strength, low density, and low CTEs*.

4.4 Conclusions

1. The room temperature moduli of most Nb-alloys agree well with mole fraction weighted rule-of-mixture calculations based upon the moduli of the alloy constituents. However, historical high-temperature elastic moduli reported in the literature for Nb-alloys have significant inconsistencies with respective modern measurements, suggesting that additional modern measurements are needed to understand the temperature dependence of Nb-alloy elastic moduli. At present, it is suggested that a single, linear temperature dependence of the elastic properties be employed for all the Nb-alloys considered in this study.

2. A single temperature-dependent thermal conductivity relationship based upon the Smith-Palmer equation adequately describes pure Nb and most of the Nb-based alloys investigated (alloy dependence implied by the data is attributed to significant uncertainty in thermal conductivity measurements). However, thermal conductivity measurements of WC-3009 indicate that it possesses significantly lower thermal conductivity than the other Nb-alloys investigated, and this is associated with the high Hf content of the WC-3009.

3. A performance index (PI) is introduced for lightweight, panel-shaped applications subject to thermal gradients or transients. Because of its relatively high density, high thermal expansion, and low thermal conductivity, WC-3009 appears to be the worst suited for such applications despite its high strength at low temperatures and high strain rates. Hf-free alloys Cb-752, D-43, and FS-85 are worthy of further study, however, commercially available C103 ranks surprisingly well across a wide range of strain rate and temperature conditions.

4. Beyond the properties considered here, additional properties must be considered when selecting a refractory alloy for a given application, such as oxidation resistance, ductile-brittle transition temperature (DBTT), and cost (which may largely be associated with alloying element availability, manufacturing challenges, formability, weldability, etc.).

Chapter 5: Conclusions

In summary, this work investigated the temperature dependence of various thermophysical properties (specific heat capacity, thermal conductivity, and coefficient of thermal expansion) and mechanical properties (flow strength and elastic modulus) of six historically researched Nb-alloys; these alloys include C103, WC-3009, C-129(Y), Cb-752, D-43, and FS-85. The goal of this work was to provide engineers with the appropriate tools required to informed decisions regarding which of these materials merit further investigation and employment into application; specific attention was paid to aerospace applications in this thesis. This work employs various physically based empirical relationships that can be, in turn, used to predict the high-temperature property values for temperatures that data does not currently exist in literature for the investigated alloys. Such relationships include (i) the Sellars-Tegart model and modified Larson-Miller parameter for flow strength; (ii) a Smith-Palmer type relationship for thermal conductivity; and (iii) a linear relationship for both elastic modulus and coefficient of thermal expansion (CTE). From this, three main conclusions can be drawn:

1. Trends in room temperature/low-temperature elastic modulus and density data for all of the alloys are well understood and can be replicated via various techniques (e.g., experimental, rule-of-mixture calculations, or Thermo-Calc modeling). Moreover, low-temperature flow strength is also well understood. However, with the exception of material density and flow strength, there is a general lack of confidence in the accuracy of high-temperature data within literature. New data for Nb-Hf alloys were included in this work to alleviate some of the inaccuracies throughout the historical data. Two major takeaways from the comparison of these new data to the historical data are: (i) the elastic modulus of Nb-alloys are larger and less temperature dependence than historical data suggests and (ii) WC-3009 appears to have a significantly lower thermal conductivity than the other investigated Nb-alloys, where they all of had values within experimental uncertainty of each other. Various possibilities for these inconsistencies have been discussed. These include the presence of more compliant textures during historical tensile testing, resulting in lower elastic modulus measurements, and the detrimental effect of lattice strain imparted by the significant Hf content in WC-3009 has on the thermal conductivity. Strategies that engineers can employ to gain a more informed understanding of the temperature dependence of investigated properties are also suggested, such as assuming a singular temperature dependence of elastic modulus for all Nb-alloys or using a singular thermal conductivity for all Nb-alloys but WC-3009.

2. A *minimum flow stress* model is proposed, which incorporates both the Sellars-Tegart model and Larson-Miller parameter. The Sellars-Tegart model is based upon steady-state flow, rendering it always nonconservative as it excludes contributions of transient material responses (i.e., primary or tertiary creep); however, it provides a unified approach to describe the behavior of materials within the low stress, power-law behavior (creep) and higher stress power-law breakdown (thermally activated plasticity). On the other hand, the Larson-Miller parameter is only accurate within the conditions (i.e., the mechanism) that it was empirically developed for, but can account for material transients. A *modified* version of the Larson-Miller parameter (LMP*) can further be employed for these Nb-alloys due to their (Class 1 or Class A-type) mildly accelerating creep behavior, which may be described as approximately steady-state throughout. This allows for *any* creep-life data to be employed when developing the Larson-Miller parameters for these alloys. The combination of these empirical flow stress relationships mitigates the risks associated with the use of either approach independently. Moreover, the use of any such model allows for interpolation and extrapolation of scant available date enabling direct comparisons between alloys elevated temperature strength across various strain rates to be made. The high strain rate sensitivity of the Nb-alloys implies that their elevated temperature flow strengths are highly dependent on rate and can therefore only be compared at the same strain rate. The inability to do so can result in incorrect understandings of alloy performance at elevated temperatures. An example of stress relaxation was also included to further demonstrate the importance of strain rate sensitivity of hypothetical high-temperature applications; where the more sensitive alloys (i.e., Class 1 alloys with a sensitivity of $\approx$0.33) will relax faster than alloys will smaller strain rate sensitivities (i.e., Class 2 alloys with sensitivities $\leq$ 0.2).

3. The combination of thermophysical and mechanical properties into a performance index can inform on alloy performance at elevated temperatures; this thesis specifically focused on a PI for a lightweight panel undergoing a thermal gradient/transient. It is important to consider more properties than flow stress when selecting a material for high-temperature applications, as those that are high in strength may have detrimental properties that would otherwise make them unsuitable for the given application. Although C103 has the lowest strength at the rates and temperatures investigated, when considering its thermophysical properties collectively, it has comparable performance to the higher strength alloys. Moreover, Nb-W-Zr alloys appear to have an ideal combination of both strength and thermophysical properties when considering an application involving thermal gradients and transients, making them a top candidate for such applications.

Chapter 6: Future Work

This thesis aimed to provide a greater understanding of the high-temperature properties and trends of historically developed Nb-alloys, such that engineers or designers can confidently select these alloys for possible aerospace applications. Through using empirical relationships to understand such temperature dependencies, numerous knowledge gaps within current existing literature have been identified.

The first general gap relates to the creep testing of the alloys and optimal heat treatments. High-temperature steady-state data does not exist for WC-3009 above 1317˚C and above 1371˚C for creep-life tests. The inclusion of this data in the literature would verify if WC-3009 does have a similar creep response to C103 at elevated temperatures and slower strain rates as the developed models suggest in this thesis. Moreover, this data would aid in reducing the extrapolations of the WC-3009 minimum flow stress model. In a similar regard, for both Cb-752 and D-43, no creep data, including both steady-state and creep-life, exists at testing temperatures beyond 1204˚C. Although the provided data within the literature does span a range of Zener-Holloman (Z) and modified Larson-Miller parameters (LMP*) (i.e., Cb-752 and D-43 demonstrated smaller sections of extrapolation in the minimum flow stress model than WC-3009), this creep testing of Cb-752 and D-43 at elevated temperatures would further improve the accuracy of the Sellars-Tegart (ST) and LMP* models at temperature in which Ni-superalloys cannot operate. Moreover, the LMP* responses of each Nb-alloy were developed via data obtained from samples in the identified optimal heat treatment conditions. For alloys Cb-752 and FS-85, this optimal heat treatment was considered to include a high-temperature final anneal. However, the microstructural features primarily responsible for the improved creep resistance after the anneal is unclear, whether it be attributed to the formation and growth of unintentional second-phases (i.e., oxides and/or carbides) within the matrix or large grains. Detailed studies that focus on impurity concentration and changes of the microstructure with annealing temperature will be required to inform on the underlying strengthening mechanism(s) of these high-temperature anneals. Along similar lines of investigating optimal heat treatments, of the two WC-3009 processing histories present in literature (1 hr at 1317˚C and 2 hr at 1260˚C), it is unclear which one is truly the optimal schedule, as no creep-life data exists for the 1317˚C treatment, which appears to result in stronger samples at tensile testing conditions when compared to the 1260˚C treatment. Lastly, no optimal C103 heat treatment was identified as no studies of this topic are currently available in literature, to the best of the author's knowledge.

In relation to further understanding the creep response of these materials, it would be advantageous to improve the current process described in this thesis for determining the breakaway stress between solute and dislocation. Currently, the binding energy used within the calculation is dependent upon the atomic volume of the matrix (estimated by an expanded version of Vegard's law in this thesis) and only accounts for one species of solute interacting with the dislocation. One avenue for possible improvement includes incorporating atomistic simulations to gain a more accurate prediction of the atomic volume of the matrix. Additionally, developing a process that can account for multiple solutes may not only improve the accuracy of the results presented in this thesis but can extend the technique's applicability to HEA/CCAs. A possible approach for this could include accounting for multiple species within the solute cloud of a dislocation via a rule-of-mixtures approach that incorporates each solute's interaction energy and respective composition.

With respect to the uncertainties identified within existing high-temperature elastic modulus measurements, modern measurements for all of the alloys would confirm or disprove the assumption made in this thesis that all Nb-alloys have similar temperature dependencies up to 1200˚C. Modern measurements of high-temperature modulus values can be gathered via tensile testing equipped with an extensometer, as was done in this thesis. However, although this will provide more reliable data than the historical literature data presented, concerns regarding the effects of microplasticity are still relevant. Moreover, it remains unknown whether the behavior of elastic modulus past 1200˚C is a result of the material or acquisition method; this is important to understand, as again, Ni-superalloys cannot survive above 1100˚C. Therefore, it would be advantageous if the modern high-temperature elastic moduli of these Nb-alloys were measured dynamically (i.e., using ultrasonic methods), especially at temperature above 1200˚C. Nonetheless, texture will remain an important factor in these measurements regardless of the technique employed, meaning that a succinct understanding and articulation of sample texture prior to testing is required. A clear understanding of the behavior of elastic modulus with temperature with respect to texture will also inform on the high-temperature trends of other elastic properties of the material (i.e., shear modulus and Poisson's ratio), which are also currently lacking in literature.

Knowledge gaps relating to the discussed thermophysical properties were also identified in this thesis. Firstly, there is a general lack of accurate specific heat capacity data within the literature. The current experimental data and Thermo-Calc predictions are similar, but the trends do not align, especially at higher temperatures. Therefore, new specific heat capacity measurements are desired, which can be conducted via differential scanning calorimetry (DSC) methods. Moreover, accurate specific heat capacity data will also improve the accuracy of the thermal conductivity measurements of the Nb-alloys. However, as previously discussed, errors as large as 20% can exist in thermal conductivity measurements, meaning that in addition to having accurate specific heat capacity at temperature data, confidence in thermal conductivity measurements can also be improved through developing a firm understanding of the impurity content and defect concentration of the sample; these can be understood through composition analysis methods and x-ray diffraction (XRD) techniques. New thermal conductivity values can be acquired via time-domain thermoreflectance (TDTR) or steady-state thermoreflectance (SSTR) measurements; TDTR is a technique that has demonstrated the capability to measure conductivities up to ≈727˚C, depending on the type of transducer applied to the sample prior to measurement. In this thesis, an aluminum transducer was used, which limited the presented measurements to a maximum temperature of 500˚C. SSTR is a cutting-edge thermal conductivity measurement technique that eliminates the need for knowledge of specific heat capacity. SSTR achieves this by relying on steady-state temperatures, which removes the specific heat capacity term in the heat diffusion equation, thus removing the dependence of thermal conductivity on heat capacity. Therefore, if uncertainties within the specific heat capacity data remains, SSTR is a viable option for understanding the high-temperature thermal conductivity behavior of these Nb-alloys.

Finally, with respect to the coefficient of thermal expansion (CTE), new measurements for alloys D-43 and WC-3009 are required. Currently, limited CTEs for D-43 exist in the literature and those reported for WC-3009 do not align well with the trends of other Nb-Hf alloys (C103 and C-129(Y)), as well as significantly disagree with the Thermo-Calc predictions. It is hypothesized that oxygen impurities may be responsible for the increased literature reported CTEs for WC-3009, therefore, testing on low-oxygen content WC-3009 may be of interest. However, maintaining low impurity content will pose as an issue for conducting these measurements, as typical obtainment techniques are done outside of vacuum or not in an oxygen-free environment (i.e., hot-stage XRD or synchrotron source with an aerodynamic levitation system); thermodilatometry was used in this thesis to measure the CTEs of C103.

Generally, the knowledge gaps identified in this thesis relate to either the lack of data in literature or the errors and uncertainties associated with the literature data. It should be noted for a final time that all high-temperature testing and processing of Nb-alloys must be conducted under vacuum or at least in an inert environment to ensure that impurity pick-up does not play a significant role in the results of the modern measurements of these properties.

Appendix A: Applicability of Modified Larson-Miller Parameter

In this appendix, it will be demonstrated that the creep-life of a material with an approximately linear creep curve can be described using the modified LMP presented in this thesis. If the creep curve mainly demonstrates slowly accelerating or steady-state creep, then a linear regression can be fit to the curve; an example creep curve of Cb-752 is presented in Figure A1 (replotted from Titran [88]) with its fit linear regression. A secant slope analysis can be done such that the values of $(\varepsilon(\%)/t(hr))$ throughout the creep test can be observed (i.e., the total aggregated strain with respect to total time). This type of analysis not only informs on the stages of creep (i.e., primary, secondary, or tertiary, where decelerating, steady, and accelerating rates are expected, respectively), but also on the rate at which the creep rate changes throughout the test. This analysis also implicitly assumes that the aggregated strain rate is similar to the instantaneous strain rate the material experiences. If the aggregated strain rate does not agree well with the instantaneous rate, then the LMP* cannot accurately model the behavior of the material, and therefore, cannot be employed; this is such a case for materials that undergo regions of primary creep.

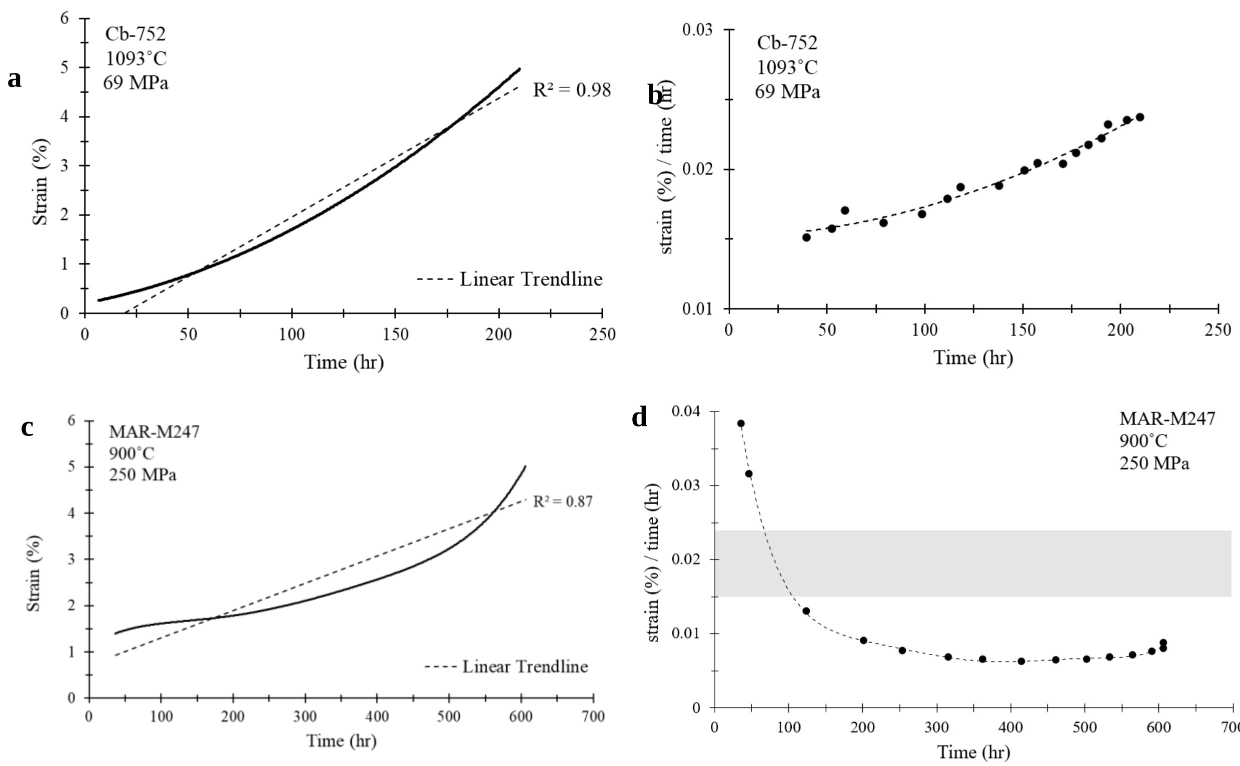

Figure A1. *Creep curves with their corresponding secant slope analysis for (a-b) Cb-752 and (c-d) MAR-M247. The linear nature of the Cb-752 creep curve results in a fairly constant slope throughout the creep test, where MAR-M247 does not demonstrate this; Cb-752 slope values are included in (d) for further comparison.*

It is through this depiction that it becomes obvious that $(\varepsilon(\%)/t(hr))$ (i.e., $log(\varepsilon(\%)/t(hr))$) does not significantly change for the Cb-752 alloy, which indicates that the modified LMP will result in approximately the same value at any given point along the curve. The LMP* values will not be exactly the same due to the creep curve not being exactly linear throughout the entire test. When preforming the same treatment on a MAR-M247 curve (replotted from [84]), creep rate varies significantly and demonstrates that this MAR-M247 specimen underwent all three stages of creep. The spread of the Cb-752 $(\varepsilon(\%)/t(hr))$ values are included within the MAR-M247 secant slope analysis (Figure A1) to further demonstrate their minimal change.

Once it has been accepted that the creep curve can be assumed to be linear (i.e., the aggregated strain rate is similar to the instantaneous strain rate) and that there is minimal rate change throughout the test, the modified LMP expression can be used to describe the creep-life of the material; meaning that any strain and corresponding time data obtained from the curve can be used. Stephenson [75] reported numerous creep-life data for Cb-752 amongst other refractory alloys; Figure A2 demonstrates the collapse of the data when using the traditional LMP and modified LMP equations. Figure A2 also includes the same treatment of MAR-M247 creep-life data (data from [84]), where the modified LMP expression does not collapse all data onto a singular curve (i.e., strain levels of ~1% do not fully collapse), which is due to the non-linearity of the MAR-M247 creep response.

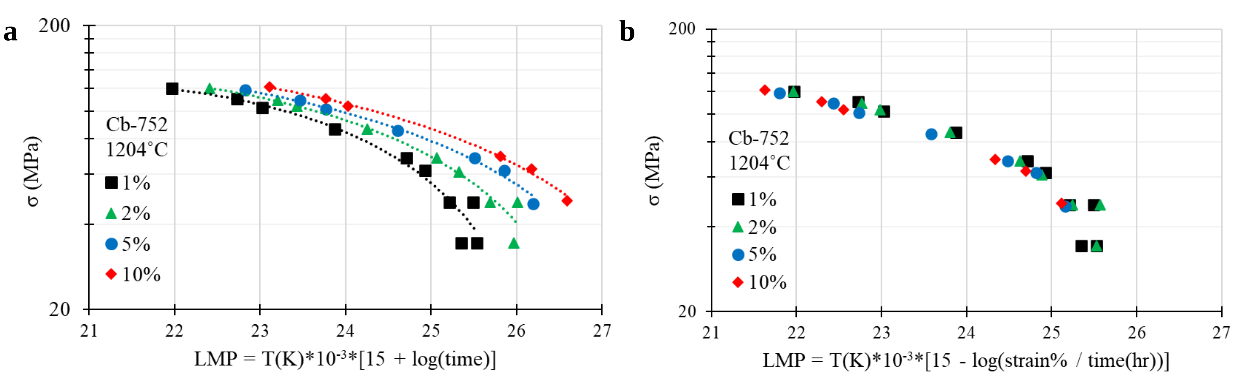

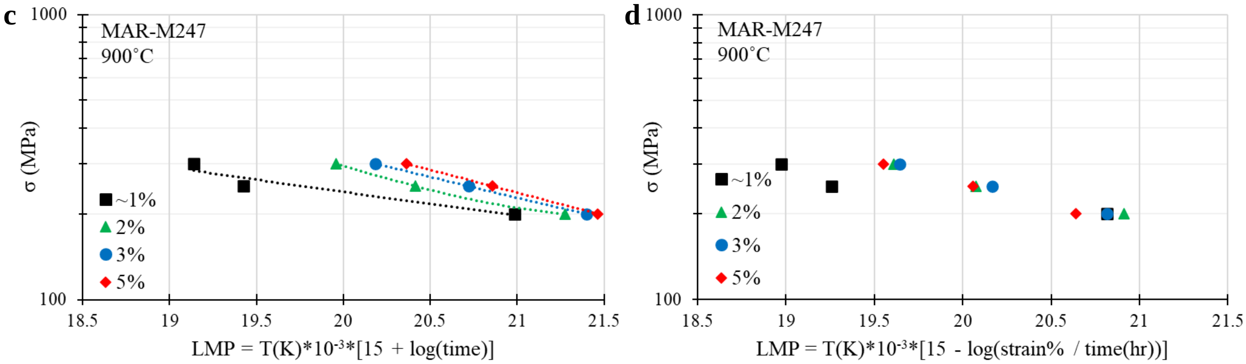

Figure A2. *(a-b) Cb-752 and (c-d) MAR-M247 creep-life data represented with the traditional and modified LMP expressions. Use of the traditional LMP results in strain-level contours, and for Cb-752, the modified LMP collapses all creep-life data onto a singular curve. MAR-M247 data does not demonstrate a similar collapse from LMP* due to its creep curve containing primary, secondary, and tertiary creep.*

Appendix B: Summary of New Data Reported in this Thesis

Table B.1. *Tensile Testing Results for C103 in Fully Recrystallized Condition (1 hr at 1316˚C)*

C103				
Test Temp (˚C)	**Test Rate (in/min)**	**Strain Rate (1/s)**	**Stress (psi)**	**Stress (MPa)**
1093	0.02	3.3E-04	27151	187.2
1093	0.5	8.3E-03	31124	214.6
1093	0.02	3.3E-04	27992	193.0
1093	0.5	8.3E-03	33359	230.0
1315	0.02	3.3E-04	13369	92.2
1315	0.5	8.3E-03	20986	144.7
1482	0.02	3.3E-04	7300	50.3
1482	0.02	3.3E-04	7584	52.3
1482	0.5	8.3E-03	13149	90.7
1482	0.5	8.3E-03	13290	91.6
1649	0.02	3.3E-04	4100	28.3
1649	0.02	3.3E-04	4238	29.2
1649	0.5	8.3E-03	8900	61.4
1649	0.5	8.3E-03	9023	62.2

Table B.2. *Tensile Testing Results for WC-3009 in Annealed and As-Printed Conditions*

WC-3009						
Anneal Time (hr)	**Anneal Temp (˚C)**	**Test Temp (˚C)**	**Test Rate (in/min)**	**Strain Rate (1/s)**	**Stress (psi)**	**Stress (MPa)**
2	1260	1200	0.02	3.3E-04	42351	292
2	1260	1200	0.5	8.3E-03	49168	339
2	1260	1400	0.02	3.3E-04	20450	141
2	1260	1400	0.5	8.3E-03	33649	232
Condition		**Test Temp (˚C)**	**Test Rate (in/min)**	**Strain Rate (1/s)**	**Stress (psi)**	**Stress (MPa)**
LPBF		1316	0.02	3.3E-04	24656	170
LPBF		1316	0.5	8.3E-03	38870	268
LPBF		1315	0.02	3.3E-04	25817	178
LPBF		1315	0.5	8.3E-03	37420	258
LPBF		1400	0.02	3.3E-04	16244	112
LPBF		1400	0.5	8.3E-03	29298	202
LPBF		1400	0.02	3.3E-04	16099	111
LPBF		1400	0.5	8.3E-03	27557	190
LPBF		1600	0.02	3.3E-04	6962	48
LPBF		1600	0.5	8.3E-03	16099	111
LPBF		1600	0.02	3.3E-04	9427	65
LPBF		1600	0.5	8.3E-03	18710	129

Table B.3. *Specific Heat Capacity Data for C103*

C103	
Test Temp (˚C)	**Cp (J/gK)**
20	0.29
100	0.29
200	0.29
300	0.29
400	0.29
500	0.30
600	0.30
700	0.31
800	0.32
900	0.32
1000	0.33
1100	0.33
1200	0.34

Table B.4. *Elastic Modulus at Room and Elevated Temperature of Fully Recrystallized C103*

C103	
Test Temp (˚C)	**E (GPa)**
25	106 $\pm$ 3
1093	94

Table B.5. *Linear Coefficient of Thermal Expansion for C103*

C103	
Test Temp (˚C)	**CTE * 10^{-6} (1/˚C)**
100	7.04
200	7.28
300	7.41
400	7.56
500	7.73
600	7.92
700	8.06
800	8.15
900	8.21
1000	8.18
1100	8.22
1200	8.24
1300	8.29
1400	8.45

Table B.6. *Thermal Conductivity Measurements of C103*

C103									
Unspecified		**Forged Nozzle**		**Forged Chamber**		**Bar**		**Sheet**	
Test Temp (˚C)	κ (W/mC)	Test Temp (˚C)	κ (W/mC)	Test Temp (˚C)	κ (W/mC)	Test Temp (˚C)	κ (W/mC)	Test Temp (˚C)	κ (W/mC)
20	35.1	19	39.4	20	38.1	20	34.9	20	36.1
100	38.4	100	41.5	100	40.7	100	38.1	100	39.0
200	41.8	200	44.1	200	43.6	200	41.8	200	42.0
300	44.7	300	46.8	300	46.0	300	44.6	300	44.7
400	47.3	400	49.1	400	48.2	400	47.1	400	47.3
500	49.6	500	51.5	500	50.4	500	49.5	500	49.7
600	51.8	600	53.6	600	52.3	600	51.6	600	51.5
700	53.8	700	55.8	700	54.2	700	53.7	700	53.7
800	55.7	800	57.8	800	56.2	800	55.5	800	55.9
900	57.4	900	59.7	900	58.0	900	57.3	900	57.5
1000	58.9	1000	61.4	1000	59.5	1000	59.0	1000	59.0
1100	60	1100	62.7	1100	60.9	1100	60.0	1100	60.4
1200	60.7	1200	63.5	1200	61.8	1200	60.7	1200	61.4
		1300	65.0	1300	62.2	1300	61.8	1300	62.3
		1400	65.9	1400	62.5	1400	61.8	1400	62.9
Cast (TDTR)									
Test Temp (˚C)	κ (W/mC)								
25	38 ± 5								

Table B.7. *Thermal Conductivity Measurements of WC-3009 in As-Cast and As-Printed Conditions*

WC-3009							
Cast (TDTR)		**Cast (TDTR)**		**LPBF (TDTR)**		**Cast (SSTR)**	
Test Temp (˚C)	κ (W/mC)	Test Temp (˚C)	κ (W/mC)	Test Temp (˚C)	κ (W/mC)	Test Temp (˚C)	κ (W/mC)
25	17 ± 2	25	22 ± 3	25	25 ± 3	25	22 ± 3
		100	23 ± 3	100	28 ± 3		
		200	26 ± 3	200	32 ± 4		
		300	31 ± 4	300	36 ± 4		
				400	35 ± 4		
				500	42 ± 5		

Table B.8. *Thermal Conductivity Measurements of high RRR Pure Nb*

RRR Nb (TDTR)	
Test Temp (˚C)	κ (W/mC)
25	60 ± 7

Appendix C: Summary of Literature Data Used in this Thesis

C.1 Creep-Life Data

Table C.1.1. *Creep-Life Data for C103*

C103							
[87]							
Test #	**Anneal Time (hr)**	**Anneal Temp (˚C)**	**Test Temp (˚C)**	**Stress (MPa)**	**Time to 1% Strain (hr)**	**Time to Rupture (hr)**	**Rupture Strain (%)**
11	1	1204	982	48.3	670	818	1.36
7	1	1327	827	138	3960	4867	1.81
5	1	1327	927	55.2	2980	4897	3.37
6	1	1327	927	82.7	1260	2037	3.17
18	1	1327	977	41.4	2210	2493	1.24
3	1	1327	977	50.1	876	982	1.28
4	1	1327	977	60.1	967	960	1.30
17	1	1327	1027	20.7	2930	3016	1.10
23	1	1327	1027	41.4	545	1294	3.35
9	1	1327	1027	55.2	229	433	3.55
14	1	1538	982	48.3	1330	2353	2.59
15	1	1649	982	48.3	1060	1153	1.19
16	1	1760	982	48.3	1600	2541	2.12
38	3	1593	927	68.9	3370	3931	1.44
30	3	1593	954	64.5	6467	6575	1.01
35	3	1593	982	20.7	20800 a	18873	0.96
33	3	1593	982	34.5	4125	5041	1.39
61	3	1593	982	48.3	1440	1717	1.30
36	3	1593	1002	27.6	5200	5230	1.06
50	3	1593	1002	34.5	1.82	2013	1.18
37	3	1593	1052	17.2	8215	9237	1.14
32	3	1593	1093	13.8	1630	4748	1.07
51	3	1593	1093	17.2	1524	1790	1.25
39	3	1593	1093	34.5	228	295	1.62

34	3	1593	1149	10.3	3245	3715	1.27
52	3	1593	1149	13.8	1052	1827	2.10
49	3	1593	1149	20.7	510	1030	3.04
40	3	1593	1149	34.5	89	240	4.11
45	3	1593	1204	6.89	4630	5066	1.10
44	3	1593	1204	10.3	1200	1415	1.32
29	3	1649	871	89.6	8975	9023	1.02
28	3	1649	927	62.1	2790	3861	1.67
27	3	1649	982	41.4	2030	2275	1.18
13	5	1427	982	48.3	1135	1387	1.42

[16]

T (˚C)	Stress (MPa)	Strain (%)	Time to Strain (hr)
982	69.2	1	100
927	85.2	1	1000
982	48.9	1	1000
1149	34.2	1	100
1093	21.2	1	1000
1149	14.0	1	1000
1205	11.5	1	1000

Table C.1.2 *Creep-Life Data for WC-3009*

WC-3009 Creep-Life							
[16]							
T (˚C)		**Stress (MPa)**		**Strain (%)**		**Time to Strain (hr)**	
982		138.4		1		100	
1104		69.4		1		100	
1216		35.0		1		100	
[83]							
HDH Swaged				**PREP Swaged/HIP'd**			
T (˚C)	**Stress (MPa)**	**Strain (%)**	**Time to Strain (hr)**	**T (˚C)**	**Stress (MPa)**	**Strain (%)**	**Time to Strain (hr)**
1260	103.0	29.0	2.7	1204	103.0	54.0	11

1149	103.0	34.0	24.4	1260	69.0	46.0	1.9
1204	69.0	55.0	18.0	1204	55.0	71.0	66.8
1288	35.0	52.0	50.9	1288	35.0	92.0	90.3
1316	28.0	94.0	69.7	1316	28.0	116.0	102.2
1371	21.0	126.0	69.4	1371	21.0	164.0	126.5

Table C.1.3. *Creep-Life Data for C-129(Y)*

C-129(Y)					
[28]					
T (˚C)	**Strain (%)**	**Time to Strain (min)**	**Time to Strain (s)**	**Stress (psi)**	**Stress (MPa)**
1371	0.2	16	960	7000	48.3
1371	0.5	40	2400	7000	48.3
1371	0.2	3	180	12000	82.7
1371	0.5	7	420	12000	82.7
1371	2	21	1260	12000	82.7
1371	0.2	1	60	15000	103.4
1371	0.5	2	120	15000	103.4
1371	2	7	420	15000	103.4
1482	0.2	20	1200	3000	20.7
1482	0.2	10	600	5000	34.5
1482	0.5	27	1620	5000	34.5
1482	0.2	3	180	7000	48.3
1482	0.5	10	600	7000	48.3
1482	2	37	2220	7000	48.3
1649	0.2	22	1320	2000	13.8
1649	0.5	46	2760	2000	13.8
1649	0.2	6	360	3000	20.7
1649	0.5	17	1020	3000	20.7
1649	0.5	3	180	5000	34.5
1649	2	8	480	5000	34.5

Table C.1.4. *Creep-life Data for Cb-752*

Cb-752						
[75]						
Anneal Time (hr)	**Anneal Temp (˚C)**	**Test Temp (˚C)**	**Stress (ksi)**	**Stress (MPa)**	**Strain (%)**	**Time to Strain (hr)**
1	1316	1204	1.48	10.19	1	930.45
1	1316	1204	3.00	20.68	1	193.77
1	1316	1204	3.00	20.68	5	1833.80
1	1316	1204	3.02	20.85	2	433.71
1	1316	1204	5.98	41.26	1	34.79
1	1316	1204	5.98	41.26	2	86.57
1	1316	1204	6.03	41.60	5	239.54
1	1316	1204	8.92	61.52	1	5.99
1	1316	1204	8.92	61.52	10	79.53
1	1316	1204	8.92	61.52	5	40.35
1	1316	1204	9.07	62.55	2	14.58
1	1316	1204	12.34	85.10	5	12.84
1	1316	1204	12.45	85.81	10	24.78
1	1316	1204	12.55	86.53	2	4.84
1	1316	1204	12.65	87.25	1	2.21
1	1316	1204	14.95	103.05	5	4.84
1	1316	1204	15.07	103.91	2	1.75
1	1316	1204	15.07	103.91	10	8.96
1	1316	1204	15.20	104.78	1	0.95
1	1316	982	13.94	96.10	1	243.00
1	1316	982	13.94	96.10	5	1357.82
1	1316	982	14.05	96.90	2	533.26
1	1316	982	18.64	128.50	5	258.99
1	1316	982	18.79	129.57	2	134.06
1	1316	982	18.95	130.65	1	70.88
1	1316	982	19.11	131.74	10	413.27
1	1316	982	24.51	169.00	1	14.41
1	1316	982	24.51	169.00	5	54.94
1	1316	982	24.72	170.40	2	26.12

1	1316	982	24.92	171.82	10	84.01
1	1316	982	34.45	237.51	5	3.06
1	1316	982	34.74	239.49	1	0.56
1	1316	982	34.74	239.49	2	1.20
1	1316	982	34.74	239.49	10	5.54
1	1318	982	35000	241.32	1	0.57
1	1318	982	35000	241.32	2	1.17
1	1318	982	35000	241.32	5	3.01
1	1368	982	35000	241.32	1	1.87
1	1368	982	35000	241.32	2	3.28
1	1368	982	35000	241.32	5	6.05
1	1480	982	35000	241.32	1	5.82
1	1480	982	35000	241.32	2	7.56
1	1480	982	35000	241.32	5	9.93
1	1591	982	35000	241.32	1	16.28
1	1591	982	35000	241.32	2	19.39
1	1591	982	35000	241.32	5	24.00
1	1371	1204	17500	120.66	1	0.63
1	1371	1204	17500	120.66	2	1.16
1	1371	1204	17500	120.66	5	2.23
1	1480	1204	17500	120.66	1	0.96
1	1480	1204	17500	120.66	2	1.67
1	1480	1204	17500	120.66	5	3.25
1	1591	1204	17500	120.66	1	2.38
1	1591	1204	17500	120.66	2	3.50
1	1591	1204	17500	120.66	5	4.67
1	1593	1204	17258.21	118.99	1	2.33
1	1593	1204	11647.62	80.31	1	18.81
1	1593	1204	8845.18	60.99	1	33.26
1	1593	1204	5853.43	40.36	1	118.08
1	1593	1204	3873.59	26.71	1	385.23
1	1593	1204	17089.3947	117.83	2	3.40
1	1593	1204	11647.6242	80.31	2	28.69

1	1593	1204	8845.1774	60.99	2	51.82
1	1593	1204	5796.17364	39.96	2	217.83
1	1593	982	36712.9402	253.13	1	4.61
1	1593	982	29629.0077	204.28	1	15.72
1	1593	982	20287.8862	139.88	1	122.44
1	1593	982	20287.8862	139.88	1	383.88
1	1593	982	18488.1124	127.47	1	409.04
1	1593	982	24256.1489	167.24	1	122.44
1	1593	982	36976.2249	254.94	2	5.23
1	1593	982	29841.4903	205.75	2	19.02
1	1593	982	24256.1489	167.24	2	145.02
1	1593	982	20287.8862	139.88	2	183.03
1	1593	982	20433.3795	140.88	2	464.41
1	1593	982	18356.4701	126.56	2	724.27
[88]						
Anneal Time (hr)	Anneal Temp (˚C)	Test Temp (˚C)	Stress (psi)	Stress (MPa)	Strain (%)	Time to Strain (hr)
1	1204	1093	8520	58.74	0.27	18.08
1	1204	1093	8520	58.74	0.40	27.12
1	1204	1093	8520	58.74	0.87	90.40
1	1204	1093	8520	58.74	1.90	198.87
1	1204	1093	8520	58.74	3.04	298.31
1	1204	1093	8520	58.74	4.29	397.74
1	1204	1093	8520	58.74	4.98	451.98
1	1204	1204	4270	29.44	0.52	18.08
1	1204	1204	4270	29.44	0.99	54.24
1	1204	1204	4270	29.44	1.51	90.40
1	1204	1204	4270	29.44	2.03	126.55
1	1204	1204	4270	29.44	2.48	162.71
1	1204	1204	4270	29.44	3.02	207.91
1	1204	1204	4270	29.44	3.47	253.11
1	1204	1204	4270	29.44	3.99	307.34
1	1204	1204	4270	29.44	4.48	352.54
1	1204	1204	4270	29.44	5.00	406.78

1	1204	1093	10000	68.95	0.99	68.57
1	1204	1093	10000	68.95	1.96	114.29
1	1204	1093	10000	68.95	2.97	154.29
1	1204	1093	10000	68.95	3.98	182.86
1	1204	1093	10000	68.95	4.99	205.71

Table C.1.5. *Creep-Life Data for D-43*

D-43						
[76]						
Heat Treatment	**Time to Strain (hr)**	**Stress (psi)**	**Stress (MPa)**	**Strain (%)**	**Test Temp (˚C)**	
SR @ 980C	1.1	35312	243.46	1	980	
SR @ 980C	5.7	27894	192.32	1	980	
SR @ 980C	23.0	23516	162.14	1	980	
SR @ 980C	39.0	22035	151.93	1	980	
SR @ 980C	56.5	20370	140.44	1	980	
SR @ 980C	128.7	16533	113.99	1	980	
SR @ 980C	2.2	35407	244.13	2	980	
SR @ 980C	14.8	27894	192.32	2	980	
SR @ 980C	64.7	23200	159.96	2	980	
SR @ 980C	103.7	22035	151.93	2	980	
SR @ 980C	175.6	20592	141.97	2	980	
SR @ 980C	503.1	16444	113.38	2	980	
SR @ 980C	4.7	35504	244.79	5	980	
SR @ 980C	43.4	27744	191.29	5	980	
SR @ 980C	222.3	23200	159.96	5	980	
SR @ 980C	315.8	21976	151.52	5	980	
SR @ 980C	632.8	20536	141.59	5	980	
SR @ 980C	7.4	35696	246.12	10	980	
SR @ 980C	68.7	27894	192.32	10	980	
SR @ 980C	391.9	22887	157.80	10	980	
SR @ 980C	538.2	21916	151.11	10	980	
SR @ 980C	1193.4	20592	141.97	10	980	

SR @ 980C	0.7	24776	170.83	1	1090	
SR @ 980C	1.1	22368	154.22	1	1090	
SR @ 980C	1.2	22368	154.22	1	1090	
SR @ 980C	5.2	17322	119.43	1	1090	
SR @ 980C	5.2	14740	101.63	1	1090	
SR @ 980C	11.0	17557	121.05	1	1090	
SR @ 980C	13.6	14939	103.00	1	1090	
SR @ 980C	41.8	12849	88.59	1	1090	
SR @ 980C	274.1	8935	61.61	1	1090	
SR @ 980C	1.9	24776	170.83	2	1090	
SR @ 980C	3.2	22248	153.39	2	1090	
SR @ 980C	3.6	22248	153.39	2	1090	
SR @ 980C	16.0	17369	119.75	2	1090	
SR @ 980C	32.1	17322	119.43	2	1090	
SR @ 980C	35.7	14899	102.73	2	1090	
SR @ 980C	53.8	14779	101.90	2	1090	
SR @ 980C	142.5	12849	88.59	2	1090	
SR @ 980C	896.7	8959	61.77	2	1090	
SR @ 980C	5.3	24776	170.83	5	1090	
SR @ 980C	13.9	22188	152.98	5	1090	
SR @ 980C	14.9	22308	153.81	5	1090	
SR @ 980C	63.4	17322	119.43	5	1090	
SR @ 980C	97.3	14779	101.90	5	1090	
SR @ 980C	254.3	14819	102.17	5	1090	
SR @ 980C	545.4	12884	88.83	5	1090	
SR @ 980C	9.3	24776	170.83	10	1090	
SR @ 980C	21.9	22248	153.39	10	1090	
SR @ 980C	102.8	17416	120.08	10	1090	
SR @ 980C	125.2	17137	118.15	10	1090	
SR @ 980C	163.3	17416	120.08	10	1090	
SR @ 980C	374.9	14819	102.17	10	1090	
SR @ 980C	415.3	14859	102.45	10	1090	
SR @ 980C	1020.6	12884	88.83	10	1090	

SR @ 980C	0.9	15163	104.54	1	1204	
SR @ 980C	1.3	12725	87.74	1	1204	
SR @ 980C	6.0	9184	63.32	1	1204	
SR @ 980C	10.2	8161	56.26	1	1204	
SR @ 980C	26.8	6135	42.30	1	1204	
SR @ 980C	28.7	5107	35.21	1	1204	
SR @ 980C	1.7	15287	105.40	2	1204	
SR @ 980C	2.8	12673	87.38	2	1204	
SR @ 980C	11.8	9184	63.32	2	1204	
SR @ 980C	18.1	8194	56.49	2	1204	
SR @ 980C	51.5	6110	42.13	2	1204	
SR @ 980C	61.8	5107	35.21	2	1204	
SR @ 980C	3.3	15225	104.97	5	1204	
SR @ 980C	5.6	12829	88.45	5	1204	
SR @ 980C	24.2	9184	63.32	5	1204	
SR @ 980C	35.9	8194	56.49	5	1204	
SR @ 980C	110.8	6160	42.47	5	1204	
SR @ 980C	148.4	5107	35.21	5	1204	
SR @ 980C	5.1	15225	104.97	10	1204	
SR @ 980C	8.8	12829	88.45	10	1204	
SR @ 980C	42.6	9222	63.58	10	1204	
SR @ 980C	55.3	8261	56.96	10	1204	
SR @ 980C	183.4	6135	42.30	10	1204	
SR @ 980C	291.4519	5128	35.35	10	1204	
[170]						
Time to Strain (hr)	**Stress (MPa)**	**Strain (%)**	**Test Temp (˚C)**			
60	138	1	1093			
3	138	1	1204			
[88]						
Heat Treatment	**Time to Strain (hr)**	**Stress (psi)**	**Stress (MPa)**	**Strain (%)**	**Test Temp (˚C)**	
D-43M	1148	10000	68.9	2.2	1204	
D-43M	1096	10000	68.9	2.1	1204	

D-43M	997	10000	68.9	1.9	1204	
D-43M	908	10000	68.9	1.7	1204	
D-43M	814	10000	68.9	1.5	1204	
D-43M	704	10000	68.9	1.3	1204	
D-43M	605	10000	68.9	1.1	1204	
D-43M	511	10000	68.9	1.0	1204	
D-43M	407	10000	68.9	0.8	1204	
D-43M	303	10000	68.9	0.6	1204	
D-43M	203	10000	68.9	0.4	1204	
D-43M	1987	8520	58.7	2.0	1093	
D-43M	1897	8520	58.7	1.9	1093	
D-43M	1789	8520	58.7	1.8	1093	
D-43M	1699	8520	58.7	1.7	1093	
D-43M	1600	8520	58.7	1.7	1093	
D-43M	1501	8520	58.7	1.6	1093	
D-43M	1402	8520	58.7	1.5	1093	
D-43M	1303	8520	58.7	1.4	1093	
D-43M	1204	8520	58.7	1.3	1093	
D-43M	1097	8520	58.7	1.2	1093	
D-43M	998	8520	58.7	1.1	1093	
D-43M	908	8520	58.7	1.0	1093	
D-43M	800	8520	58.7	0.9	1093	
D-43M	701	8520	58.7	0.8	1093	
D-43M	602	8520	58.7	0.7	1093	
D-43M	494	8520	58.7	0.6	1093	
D-43M	396	8520	58.7	0.5	1093	
D-43M	297	8520	58.7	0.5	1093	
D-43M	207	8520	58.7	0.4	1093	
D-43M	99	8520	58.7	0.3	1093	
D-43M	1841	4270	29.4	2.3	1204	
D-43M	1795	4270	29.4	2.2	1204	
D-43M	1687	4270	29.4	2.1	1204	
D-43M	1588	4270	29.4	2.0	1204	

D-43M	1489	4270	29.4	1.9	1204	
D-43M	1389	4270	29.4	1.8	1204	
D-43M	1290	4270	29.4	1.6	1204	
D-43M	1182	4270	29.4	1.5	1204	
D-43M	1083	4270	29.4	1.4	1204	
D-43M	992	4270	29.4	1.3	1204	
D-43M	893	4270	29.4	1.1	1204	
D-43M	785	4270	29.4	1.0	1204	
D-43M	686	4270	29.4	0.9	1204	
D-43M	586	4270	29.4	0.8	1204	
D-43M	487	4270	29.4	0.6	1204	
D-43M	388	4270	29.4	0.5	1204	
D-43M	280	4270	29.4	0.4	1204	
D-43M	180	4270	29.4	0.3	1204	
D-43M	90	4270	29.4	0.2	1204	
[89]						
Heat Treatment	**Time to Strain (hr)**	**Stress (psi)**	**Stress (MPa)**	**Strain (%)**	**Test Temp (˚C)**	
D-43M	24	39	269.4	1	982	
D-43M	109	34	235.7	1	982	
D-43M	169	27	184.5	1	982	
D-43M	1311	22	151.4	1	982	
D-43M	190	29	202.5	1	982	
D-43M	32	39	271.0	2	982	
D-43M	130	34	237.0	2	982	
D-43M	227	29	202.5	2	982	
D-43M	244	27	185.6	2	982	
D-43M	1917	22	151.4	2	982	
D-43M	12	27	187.2	1	1093	
D-43M	15	27	187.2	2	1093	
D-43M	20	27	187.2	5	1093	
D-43M	22	25	171.9	1	1093	
D-43M	30	25	171.9	2	1093	
D-43M	43	25	170.3	5	1093	

D-43M	79	20	135.7	1	1093	
D-43M	107	20	135.7	2	1093	
D-43M	169	20	135.7	5	1093	
D-43M	115	16	109.2	1	1093	
D-43M	195	16	109.2	2	1093	
D-43M	356	16	109.2	5	1093	
D-43M	411	14	95.7	1	1093	
D-43M	864	14	97.5	2	1093	
D-43M	1	22	152.6	1	1204	
D-43M	2	22	154.4	2	1204	
D-43M	2	22	152.6	1	1204	
D-43M	3	23	156.3	2	1204	
D-43M	7	17	119.4	1	1204	
D-43M	12	17	119.4	2	1204	
D-43M	11	15	102.6	1	1204	
D-43M	20	15	103.8	2	1204	
D-43M	40	12	85.1	1	1204	
D-43M	86	12	86.1	2	1204	
D-43M	25	11	74.8	1	1204	
D-43M	57	11	75.7	2	1204	
D-43M	160	11	75.7	5	1204	
D-43M	197	12	86.1	5	1204	
D-43M	4	40	274.0	1	982	
D-43M	103	35	239.5	1	982	
D-43M	249	25	169.3	1	982	
D-43M	1239	20	138.8	1	982	
D-43M	10	40	274.0	2	982	
D-43M	129	35	242.6	2	982	
D-43M	311	25	170.4	2	982	
D-43M	2318	20	137.9	2	982	
D-43M	14	20	137.9	1	1093	
D-43M	46	20	137.9	2	1093	
D-43M	71	20	137.9	5	1093	

D-43M	57	17	120.5	1	1093	
D-43M	110	17	120.5	2	1093	
D-43M	144	17	120.5	5	1093	
D-43M	63	17	120.5	1	1093	
D-43M	102	17	120.5	2	1093	
D-43M	160	17	120.5	5	1093	
D-43M	342	13	89.3	1	1093	
D-43M	644	12	81.4	2	1093	
D-43M	817	13	89.3	5	1093	
D-43M	434	12	80.5	1	1093	
D-43M	37.7	13	86.5	1	1204	
D-43M	60.3	13	86.5	2	1204	
D-43M	99.4	13	86.5	5	1204	
D-43M	195.4	9	63.2	1	1204	
D-43M	395.3	9	62.4	2	1204	
D-43M	799.9	9	62.4	5	1204	
D-43M	303.5	8	58.2	1	1204	
D-43M	562.3	8	58.2	2	1204	
D-43M	1011.8	8	57.6	5	1204	
D-43M	0.2	20	137.9	2	1204	
D-43M	0.7	20	137.9	5	1204	
[88]						
Anneal Time (hr)	**Anneal Temp (˚C)**	**Time to Strain (hr)**	**Stress (psi)**	**Stress (MPa)**	**Strain (%)**	**Test Temp (˚C)**
1	1204	914	10000	68.9	5.0	1204
1	1204	800	10000	68.9	4.0	1204
1	1204	701	10000	68.9	3.2	1204
1	1204	603	10000	68.9	2.5	1204
1	1204	494	10000	68.9	1.9	1204
1	1204	405	10000	68.9	1.4	1204
1	1204	301	10000	68.9	1.0	1204
1	1204	208	10000	68.9	0.6	1204
1	1427	73	10000	68.9	0.5	1204
1	1427	135	10000	68.9	1.0	1204

1	1427	197	10000	68.9	1.5	1204
1	1427	249	10000	68.9	2.0	1204
1	1427	306	10000	68.9	2.5	1204
1	1427	353	10000	68.9	3.0	1204
1	1427	410	10000	68.9	3.5	1204
1	1427	452	10000	68.9	4.0	1204
1	1427	499	10000	68.9	4.5	1204
1	1427	540	10000	68.9	5.0	1204

Table C.1.6. *Creep-Life Data for FS-85*

FS-85			
[16]			
Test Temp (˚C)	**Stress (MPa)**	**Strain (%)**	**Time to Strain (hr)**
1010	138.3	1	100
1177	69.6	1	100
1309	35.0	1	100
1093	66.2	1	1000
1205	31.8	1	1000

[75]							
Anneal Time (hr)	**Anneal Temp (˚C)**	**Test Temp (˚F)**	**Test Temp (˚C)**	**Time to Strain (hr)**	**Stress (ksi)**	**Stress (MPa)**	**Strain (%)**
1	1371	2600	1427	0.3	10	69.8	1
1	1371	2600	1427	1.2	8	55.9	1
1	1371	2600	1427	3.6	6	41.6	1
1	1371	2600	1427	20.1	4	24.2	1
1	1371	2600	1427	288.7	1	7.0	1
1	1371	2600	1427	0.6	10	68.9	2
1	1371	2600	1427	2.2	8	55.2	2
1	1371	2600	1427	8.9	6	41.6	2
1	1371	2600	1427	49.8	4	24.5	2
1	1371	2600	1427	740.0	1	7.0	2
1	1371	2600	1427	1.1	10	69.8	5

1	1371	2600	1427	4.9	8	55.2	5
1	1371	2600	1427	23.5	6	41.6	5
1	1371	2600	1427	149.4	3	23.9	5
1	1371	2600	1427	1.9	10	68.9	10
1	1371	2600	1427	8.1	8	55.2	10
1	1371	2600	1427	41.3	6	41.6	10
1	1371	2600	1427	288.7	4	24.5	10
1	1371	2200	1204	0.7	17	120.4	1
1	1371	2200	1204	2.4	16	110.5	1
1	1371	2200	1204	3.9	15	102.6	1
1	1371	2200	1204	14.3	13	86.4	1
1	1371	2200	1204	53.1	10	68.3	1
1	1371	2200	1204	74.9	9	61.9	1
1	1371	2200	1204	116.0	7	47.8	1
1	1371	2200	1204	179.6	7	47.8	1
1	1371	2200	1204	144.3	5	34.3	1
1	1371	2200	1204	191.1	5	34.3	1
1	1371	2200	1204	1.5	17	120.4	2
1	1371	2200	1204	5.1	16	109.1	2
1	1371	2200	1204	7.2	15	103.9	2
1	1371	2200	1204	25.9	13	86.4	2
1	1371	2200	1204	93.2	10	68.3	2
1	1371	2200	1204	139.9	9	61.2	2
1	1371	2200	1204	245.4	7	47.8	2
1	1371	2200	1204	404.4	7	47.8	2
1	1371	2200	1204	379.9	5	34.3	2
1	1371	2200	1204	2.8	17	119.0	5
1	1371	2200	1204	7.7	16	109.1	5
1	1371	2200	1204	12.3	15	101.4	5
1	1371	2200	1204	45.5	12	85.3	5
1	1371	2200	1204	185.3	10	68.3	5
1	1371	2200	1204	315.0	9	61.9	5
1	1371	2200	1204	535.6	7	47.2	5

1	1371	2200	1204	4.4	18	121.9	10
1	1371	2200	1204	12.2	16	110.5	10
1	1371	2200	1204	18.4	15	103.9	10
1	1371	2200	1204	295.9	10	69.2	10
1	1371	2200	1204	519.1	9	62.7	10
1	1371	2200	1204	1000.0	7	48.4	10
1	1371	1800	982	4.2	35	243.7	1
1	1371	1800	982	25.0	30	204.9	1
1	1371	1800	982	127.7	25	172.3	1
1	1371	1800	982	204.5	22	152.2	1
1	1371	1800	982	447.9	21	143.1	1
1	1371	1800	982	33.1	30	207.5	2
1	1371	1800	982	174.8	25	170.2	2
1	1371	1800	982	288.7	22	154.1	2
1	1371	1800	982	10.1	34	237.7	5
1	1371	1800	982	45.4	30	204.9	5
1	1371	1800	982	239.2	25	170.2	5
1	1371	1800	982	477.0	22	152.2	5
1	1371	1800	982	1222.3	21	143.1	5
1	1371	1800	982	739.9	21	144.9	10
[170]							

Test Temp (˚F)	**Test Temp (˚C)**	**Time to Strain (hr)**	**Stress (MPa)**	**Strain (%)**
2000	1093	10.00	138	1
2200	1204	0.4	138	1
[75]				

Anneal Time (hr)	**Anneal Temp (˚C)**	**Test Temp (˚C)**	**Time to Strain (hr)**	**Stress (psi)**	**Stress (MPa)**	**Strain (%)**	
1	1359	982	7.5	35000	241.3	2	
1	1360	982	4.2	35000	241.3	1	
1	1360	982	10.0	35000	241.3	5	
1	1407	982	15.7	35000	241.3	2	
1	1410	982	21.9	35000	241.3	5	
1	1412	982	27.2	35000	241.3	1	

1	1605	982	49.7	35000	241.3	5	
1	1606	982	56.9	35000	241.3	1	
1	1606	982	61.7	35000	241.3	2	
1	1749	982	5.6	35000	241.3	1	
1	1751	982	16.3	35000	241.3	2	
1	1362	1204	0.8	17500	120.7	1	
1	1362	1204	1.5	17500	120.7	2	
1	1362	1204	4.3	17500	120.7	10	
1	1363	1204	3.0	17500	120.7	5	
1	1412	1204	1.8	17500	120.7	1	
1	1412	1204	3.0	17500	120.7	2	
1	1412	1204	5.0	17500	120.7	5	
1	1412	1204	6.6	17500	120.7	10	
1	1608	1204	7.4	17500	120.7	2	
1	1609	1204	5.6	17500	120.7	1	
1	1609	1204	11.7	17500	120.7	5	
1	1611	1204	13.9	17500	120.7	10	
1	1752	1204	4.7	17500	120.7	1	
1	1752	1204	7.9	17500	120.7	2	
1	1752	1204	19.6	17500	120.7	10	
1	1754	1204	13.7	17500	120.7	5	
1	1593	982	136.2	27.2	187.7	1	
1	1593	982	8.5	44.7	308.4	1	
1	1593	982	42.7	35.2	242.7	1	
1	1593	982	342.9	27.5	189.3	1	
1	1593	982	1446.5	22.5	155.5	1	
1	1593	982	10.3	44.7	308.4	2	
1	1593	982	47.5	34.9	240.6	2	
1	1593	982	187.9	27.2	187.7	2	
1	1593	982	416.1	27.5	189.3	2	
1	1593	982	1954.1	22.4	154.1	2	
1	1593	1204	0.9	20.3	140.3	1	
1	1593	1204	16.9	15.3	105.4	1	

1	1593	1204	68.5	12.6	87.1	1	
1	1593	1204	196.2	10.1	69.6	1	
1	1593	1204	961.7	7.0	48.3	1	
1	1593	1204	1.9	20.2	139.1	2	
1	1593	1204	24.9	15.2	104.5	2	
1	1593	1204	100.8	12.5	86.4	2	
1	1593	1204	358.0	9.8	67.8	2	
1	1593	1204	3.7	20.2	139.1	5	
1	1593	1204	40.9	15.2	104.5	5	
1	1593	1204	161.7	12.5	86.4	5	
1	1593	1204	625.8	10.1	69.6	5	
[88]							
Anneal Time (hr)	**Anneal Temp (˚C)**	**Test Temp (˚C)**	**Time to Strain (hr)**	**Stress (psi)**	**Stress (MPa)**	**Strain (%)**	
1	1427	2000	32.8	10000	68.9	0.1	
1	1427	2000	106.7	10000	68.9	0.2	
1	1427	2000	205.1	10000	68.9	0.3	
1	1427	2000	295.4	10000	68.9	0.4	
1	1427	2000	393.8	10000	68.9	0.6	
1	1427	2000	492.3	10000	68.9	0.7	
1	1427	2000	607.2	10000	68.9	0.9	
1	1427	2000	705.6	10000	68.9	0.9	
1	1427	2000	795.9	10000	68.9	1.1	
1	1427	2000	902.6	10000	68.9	1.2	
1	1427	2000	1001.0	10000	68.9	1.4	
1	1427	2000	1091.3	10000	68.9	1.6	
1	1427	2000	1206.2	10000	68.9	1.7	
1	1427	2000	1304.6	10000	68.9	1.9	
1	1427	2000	1403.1	10000	68.9	2.1	
1	1427	2000	1501.5	10000	68.9	2.4	
1	1427	2000	1600.0	10000	68.9	2.7	
1	1427	2000	1706.7	10000	68.9	3.0	
1	1427	2000	1805.1	10000	68.9	3.4	
1	1427	2000	1903.6	10000	68.9	3.8	

1	1427	2000	2002.1	10000	68.9	4.1	
1	1427	2000	2100.5	10000	68.9	4.6	
1	1427	2000	2182.6	10000	68.9	5.0	
1	1427	2200	99.4	5000	34.5	0.2	
1	1427	2200	198.9	5000	34.5	0.3	
1	1427	2200	289.3	5000	34.5	0.4	
1	1427	2200	388.7	5000	34.5	0.4	
1	1427	2200	497.2	5000	34.5	0.5	
1	1427	2200	587.6	5000	34.5	0.6	
1	1427	2200	705.1	5000	34.5	0.7	
1	1427	2200	804.5	5000	34.5	0.9	
1	1427	2200	904.0	5000	34.5	1.0	
1	1427	2200	994.4	5000	34.5	1.1	
1	1427	2200	1093.8	5000	34.5	1.2	
1	1427	2200	1193.2	5000	34.5	1.4	
1	1427	2200	1301.7	5000	34.5	1.5	
1	1427	2200	1401.1	5000	34.5	1.7	
1	1427	2200	1500.6	5000	34.5	1.8	
1	1427	2200	1609.0	5000	34.5	2.1	
1	1427	2200	1699.4	5000	34.5	2.2	
1	1427	2200	1807.9	5000	34.5	2.5	
1	1427	2200	1907.3	5000	34.5	2.6	
1	1427	2200	1997.7	5000	34.5	2.8	
1	1427	2200	2097.2	5000	34.5	3.0	
1	1427	2200	2205.6	5000	34.5	3.2	
1	1427	2200	2305.1	5000	34.5	3.3	
1	1427	2200	2404.5	5000	34.5	3.5	
1	1427	2200	2494.9	5000	34.5	3.7	
1	1427	2200	2603.4	5000	34.5	4.0	
1	1427	2200	2702.8	5000	34.5	4.2	
1	1427	2200	2802.3	5000	34.5	4.4	
1	1427	2200	2910.7	5000	34.5	4.6	
1	1427	2200	3001.1	5000	34.5	4.8	

1	1427	2200	3109.6	5000	34.5	5.0	

Table C.1.7. *Creep-Life Data for MAR-M247*

MAR-M247			
[85]			
Test Temp (˚C)	**Stress (MPa)**	**Time to Rupture (hr)**	**Rupture Strain**
760	724	309.1	0.14
760	669	1259.9	0.17
760	642	555.7	0.09
760	669	0.5	0.02
760	655	4.9	0.04
760	641	8.0	0.01
760	621	1155.2	0.14
760	621	331.3	0.04
871	434	184.0	0.19
871	345	774.3	0.21
871	317	1270.0	0.31
871	448	104.1	0.06
871	434	136.3	0.09
871	414	225.1	0.09
927	297	167.8	0.27
927	255	320.0	0.28
927	276	169.3	0.09
927	241	338.6	0.13
982	207	123.4	0.40
982	152	646.2	0.29
982	131	1678.3	0.25
982	207	90.4	0.10
982	186	124.3	0.12
982	172	227.4	0.09
1038	124	174.5	0.14

1038	103	838.0	0.19
[84]			
Test Temp (˚C)	**Stress (MPa)**	**Time to Rupture (hr)**	**Rupture Strain**
800	300	9131.1	0.04
800	400	1655.3	0.03
800	500	129.8	0.03
800	550	104.4	0.03
800	600	16.4	0.03
900	200	1985.6	0.05
900	250	607.3	0.05
900	300	230.8	0.06
900	400	37.1	0.08
900	450	7.8	0.08
900	500	3.9	0.07
900	550	1.4	0.05
950	150	1013.9	0.06
950	200	233.8	0.06
950	250	69.8	0.06
950	300	20.0	0.09
950	400	2.6	0.08
950	450	0.6	0.06
1000	100	1033.3	0.05
1000	150	62.0	0.02
1000	200	19.3	0.06
1000	250	5.0	0.07
1000	300	0.7	0.07
800	300	10103.7	0.05
800	400	1097.7	0.02
800	450	666.6	0.03
800	600	50.6	0.03
800	700	2.7	0.03
900	250	377.3	0.04
900	300	162.0	0.06

900	400	24.8	0.09
900	450	15.2	0.08
900	500	4.2	0.08
900	550	0.9	0.07
950	150	829.1	0.05
950	200	189.0	0.05
950	200	166.1	0.05
950	250	60.4	0.06
950	300	15.4	0.05
950	400	2.1	0.08
950	450	1.0	0.10
1000	100	931.3	0.02
1000	100	969.7	0.05
1000	150	94.3	0.05
1000	200	18.8	0.09
1000	250	4.6	0.07
1000	300	1.3	0.09

Table C.1.8. *Creep-Life Data for Haynes 230*

Haynes 230					
[86]					
Form	**Test Temp (˚C)**	**Stress (ksi)**	**Stress (MPa)**	**Time to Strain (hr)**	**Strain**
Sheet	649	48	331.0	10	0.005
Sheet	649	32	220.6	100	0.005
Sheet	649	22	151.7	1000	0.005
Sheet	649	51	351.6	10	0.01
Sheet	649	36	248.2	100	0.01
Sheet	649	25	172.4	1000	0.01
Sheet	704	31	213.7	10	0.005
Sheet	704	21	146.9	100	0.005
Sheet	704	15	100.0	1000	0.005
Sheet	704	34	234.4	10	0.01
Sheet	704	24	165.5	100	0.01
Sheet	704	17	113.8	1000	0.01
Sheet	760	17	118.6	10	0.005
Sheet	760	14	94.5	100	0.005
Sheet	760	11	74.5	1000	0.005
Sheet	760	20	137.9	10	0.01
Sheet	760	15	102.0	100	0.01
Sheet	760	12	80.7	1000	0.01
Sheet	816	13	90.3	10	0.005
Sheet	816	10	71.0	100	0.005
Sheet	816	8	53.8	1000	0.005
Sheet	816	14	97.2	10	0.01
Sheet	816	11	77.2	100	0.01
Sheet	816	9	59.3	1000	0.01
Sheet	871	10	69.0	10	0.005
Sheet	871	8	52.4	100	0.005
Sheet	871	6	37.9	1000	0.005
Sheet	871	11	75.8	10	0.01
Sheet	871	8	57.9	100	0.01

Sheet	871	6	40.0	1000	0.01
Sheet	927	8	51.7	10	0.005
Sheet	927	5	37.2	100	0.005
Sheet	927	3	23.4	1000	0.005
Sheet	927	8	57.2	10	0.01
Sheet	927	6	39.3	100	0.01
Sheet	927	4	24.8	1000	0.01
Sheet	982	5	37.2	10	0.005
Sheet	982	3	23.4	100	0.005
Sheet	982	2	11.7	1000	0.005
Sheet	982	6	39.3	10	0.01
Sheet	982	4	24.8	100	0.01
Sheet	982	2	13.1	1000	0.01
Bar and Plate	649	59	406.8	10	0.005
Bar and Plate	649	34	234.4	100	0.005
Bar and Plate	649	23	158.6	1000	0.005
Bar and Plate	649	60	413.7	10	0.01
Bar and Plate	649	39	268.9	100	0.01
Bar and Plate	649	26	182.0	1000	0.01
Bar and Plate	649	18	120.7	10000	0.01
Bar and Plate	704	30	206.9	10	0.005
Bar and Plate	704	21	141.3	100	0.005
Bar and Plate	704	15	103.4	1000	0.005
Bar and Plate	704	35	241.3	10	0.01
Bar and Plate	704	24	162.0	100	0.01
Bar and Plate	704	18	124.1	1000	0.01
Bar and Plate	704	12	84.8	10000	0.01
Bar and Plate	760	19	131.0	10	0.005
Bar and Plate	760	14	96.5	100	0.005
Bar and Plate	760	11	75.8	1000	0.005
Bar and Plate	760	22	148.2	10	0.01
Bar and Plate	760	16	109.6	100	0.01
Bar and Plate	760	12	79.3	1000	0.01

Bar and Plate	760	8	55.2	10000	0.01
Bar and Plate	816	13	92.4	10	0.005
Bar and Plate	816	11	73.1	100	0.005
Bar and Plate	816	8	56.5	1000	0.005
Bar and Plate	816	15	103.4	10	0.01
Bar and Plate	816	12	82.7	100	0.01
Bar and Plate	816	9	63.4	1000	0.01
Bar and Plate	816	7	44.8	10000	0.01
Bar and Plate	871	10	71.0	10	0.005
Bar and Plate	871	8	55.2	100	0.005
Bar and Plate	871	6	38.6	1000	0.005
Bar and Plate	871	12	80.7	10	0.01
Bar and Plate	871	9	62.1	100	0.01
Bar and Plate	871	6	41.4	1000	0.01
Bar and Plate	871	4	30.3	10000	0.01
Bar and Plate	927	8	53.8	10	0.005
Bar and Plate	927	6	37.9	100	0.005
Bar and Plate	927	3	23.4	1000	0.005
Bar and Plate	927	9	60.7	10	0.01
Bar and Plate	927	6	43.4	100	0.01
Bar and Plate	927	4	27.6	1000	0.01
Bar and Plate	927	3	17.9	10000	0.01
Bar and Plate	982	6	37.9	10	0.005
Bar and Plate	982	3	23.4	100	0.005
Bar and Plate	982	2	11.0	1000	0.005
Bar and Plate	982	6	43.4	10	0.01
Bar and Plate	982	4	26.2	100	0.01
Bar and Plate	982	2	13.8	1000	0.01
Bar and Plate	982	1	7.6	10000	0.01
Bar and Plate	1038	4	30.3	10	0.01
Bar and Plate	1038	2	13.8	100	0.01
Bar and Plate	1038	1	6.2	1000	0.01
Bar and Plate	1093	2	15.9	10	0.01

Bar and Plate	1093	1	5.5	100	0.01
Bar and Plate	1149	1	7.6	10	0.01
Bar and Plate	1149	0	2.8	100	0.01

Table C.1.9. *Creep-Life Data for ASTAR-811C*

ASTAR-811C				
[91]				
Test Temp (˚C)	**Stress (ksi)**	**Stress (MPa)**	**Time to Strain (hr)**	**Strain (%)**
1316	22	151.7	271.9	11.4
1316	18	124.1	500.7	4.0
1538	7	48.3	386.5	5.5
[90]				
Test Temp (˚C)	**Stress (ksi)**	**Stress (MPa)**	**Time to Strain (hr)**	**Strain (%)**
1316	15	103.4	23.9726	0.04
1316	15	103.4	30.82192	0.05
1316	15	103.4	47.94521	0.11
1316	15	103.4	65.06849	0.17
1316	15	103.4	143.8356	0.47
1316	15	103.4	178.0822	0.63
1316	15	103.4	191.7808	0.75
1316	15	103.4	212.3288	0.87
1316	15	103.4	246.5753	1.05
1316	15	103.4	315.0685	1.63
1093	26	179.3	89.0411	0.15
1093	26	179.3	116.4384	0.16
1093	26	179.3	143.8356	0.17
1093	26	179.3	164.3836	0.17
1093	26	179.3	188.3562	0.18
1093	26	179.3	263.6986	0.19
1093	26	179.3	284.2466	0.20

1093	26	179.3	321.9178	0.21
1093	26	179.3	335.6164	0.22
1093	26	179.3	352.7397	0.22
1093	26	179.3	428.0822	0.22
1093	26	179.3	438.3562	0.24
1093	26	179.3	472.6027	0.25
1093	26	179.3	496.5753	0.25
1093	26	179.3	523.9726	0.25
1093	26	179.3	589.0411	0.26
1093	26	179.3	609.589	0.26
1093	26	179.3	636.9863	0.28
1093	26	179.3	664.3836	0.28
1093	26	179.3	688.3562	0.28
1093	26	179.3	763.6986	0.29
1093	26	179.3	780.8219	0.29
1093	26	179.3	808.2192	0.30
1093	26	179.3	835.6164	0.31
1093	26	179.3	852.7397	0.31
1093	26	179.3	934.9315	0.32
1093	26	179.3	952.0548	0.32
1093	26	179.3	979.4521	0.33
1093	26	179.3	996.5753	0.33
1093	26	179.3	1027.397	0.34
1093	26	179.3	1102.74	0.35
1093	26	179.3	1123.288	0.35
1093	26	179.3	1143.836	0.35
1093	26	179.3	1167.808	0.35
1093	26	179.3	1191.781	0.36
1093	26	179.3	1287.671	0.38
1093	26	179.3	1315.068	0.38
1093	26	179.3	1335.616	0.39
1093	26	179.3	1359.589	0.40
1093	26	179.3	1431.507	0.41

1093	26	179.3	1458.904	0.41
1093	26	179.3	1482.877	0.43
1093	26	179.3	1500	0.42
1093	26	179.3	1527.397	0.43
1093	26	179.3	1599.315	0.44
1093	26	179.3	1619.863	0.46
1093	26	179.3	1657.534	0.45
1093	26	179.3	1671.233	0.46
1093	26	179.3	1698.63	0.46
1093	26	179.3	1773.973	0.46
1093	26	179.3	1787.671	0.47
1093	26	179.3	1811.644	0.48
1093	26	179.3	1839.041	0.48
1093	26	179.3	1859.589	0.48
1093	26	179.3	1938.356	0.50
1093	26	179.3	1958.904	0.50
1093	26	179.3	1979.452	0.52
1093	26	179.3	2013.699	0.52
1093	26	179.3	2034.247	0.52
1093	26	179.3	2130.137	0.53
1093	26	179.3	2154.11	0.53
1093	26	179.3	2174.658	0.55
1093	26	179.3	2198.63	0.55
1093	26	179.3	2273.973	0.56
1093	26	179.3	2291.096	0.57
1093	26	179.3	2325.342	0.58
1093	26	179.3	2345.89	0.58
1093	26	179.3	2369.863	0.58
1093	26	179.3	2445.205	0.58
1093	26	179.3	2469.178	0.60
1093	26	179.3	2493.151	0.60
[77]				

Test Temp (˚C)	Stress (ksi)	Stress (MPa)	Time to Strain (hr)	Strain (%)
1204	25	172.4	0.8	0.1
1204	25	172.4	18.7	0.7
1204	22.5	155.1	19.9	0.6
1204	22.5	155.1	71.1	1.0
1316	20	137.9	75.6	1.6
1316	20	137.9	91.4	2.3
1316	17.5	120.7	92.2	2.4
1316	17.5	120.7	97.2	2.5
1316	15	103.4	98.1	2.5
1316	15	103.4	164.1	3.0
1427	12.5	86.2	169.5	3.5
1427	12.5	86.2	187.8	4.4
1427	10	68.9	189.5	4.4
1427	10	68.9	241.0	5.5
1427	7.5	51.7	241.8	5.5
1427	7.5	51.7	264.3	5.7
1427	5	34.5	265.1	5.7

Table C.1.10 *Creep-Life Data for Stress-Relieved (SR) and Recrystallized (Rx) TZM*

TZM SR				
[36]				
Test Temp (˚C)	**Time to Strain (hr)**	**Stress (ksi)**	**Stress (MPa)**	**Strain (%)**
982	11.0	85	586.1	16.0
982	65.3	85	586.1	17.3
1316	2.6	35	241.3	26.1
1316	4.0	27	186.2	27.9
982	18.6	70	482.6	14.0
982	59.6	70	482.6	13.0
982	79.0	72	496.4	15.0
982	32.5	77	530.9	15.0
982	20.0	65	448.2	6.0
1093	132.6	50	344.7	12.0
1093	23.9	60	413.7	18.0
1093	6.2	65	448.2	25.0
1316	40.0	14	96.5	55.0
1316	10.1	22	151.7	25.0
1316	3.5	32	220.6	21.0
TZM Rx				
[36]				
Test Temp (˚C)	**Time to Strain (hr)**	**Stress (ksi)**	**Stress (MPa)**	**Strain (%)**
982	334.1	40.0	275.8	8.4
1316	15.0	20.0	137.9	41.7
1316	32.9	16.0	110.3	37.0
982	7.5	40.0	275.8	29.0
982	51.5	40.0	275.8	25.0
982	95.1	35.0	241.3	16.0
982	10.9	40.0	275.8	24.0
1093	213.8	27.0	186.2	27.0
1093	119.5	30.0	206.8	34.0

1093	44.0	33.0	227.5	28.0
1093	10.8	34.0	234.4	24.0
1316	40.2	14.0	96.5	57.0
1316	26.3	18.0	124.1	40.0
1316	13.1	20.0	137.9	66.0
1649	24.0	3.5	24.1	89.0
1649	4.0	5.0	34.5	90.0

C.2 Tensile Testing Data

Table C.2.1. *Tensile Test Data for C103*

C103		
[92]		
Test Temp (˚C)	**Stress (MPa)**	**Strain Rate (1/s)**
25	453.3	1.0E-01
500	311.1	1.0E-01
700	315.6	1.0E-01
900	308.9	1.0E-01
1100	260.0	1.0E-01
1300	193.3	1.0E-01
1500	140.0	1.0E-01
[93]		
Test Temp (˚C)	**Stress (MPa)**	**Strain Rate (1/s)**
25	434.0	1.0E-02
600	310.0	1.0E-02
800	308.0	1.0E-02
900	289.0	1.0E-02
1000	259.0	1.0E-02
1100	215.0	1.0E-02
1200	186.0	1.0E-02
[94]		

Condition	Test Temp (˚C)	Strain Rate (1/min)	Strain Rate (1/s)	Stress (ksi)	Stress (MPa)
Wrought	1649	3.3E-02	5.5E-04	4	26.9
Wrought	1649	3.3E-03	5.5E-05	2	15.2
PM	1649	3.3E-02	5.5E-04	5	31.7
PM	1649	3.3E-02	5.5E-04	5	31.0
PM	1649	3.3E-03	5.5E-05	3	17.2
PM	1649	3.3E-03	5.5E-05	3	17.6

Table C.2.2. *Tensile Test Data for WC-3009*

WC-3009			
[83]			
Condition	**Test Temp (˚C)**	**Stress (MPa)**	**Strain Rate (1/s)**
Prep HIP'd	869	640.6	8.5E-03
Prep HIP'd	921	595.1	8.5E-03
Prep HIP'd	1037	504.2	8.5E-03
Prep HIP'd	1094	466.9	8.5E-03
Prep HIP'd	1147	408.4	8.5E-03
Prep HIP'd	1200	350.0	8.5E-03
Prep HIP'd	1319	223.4	8.5E-03
HDH Swaged	869	622.7	8.5E-03
HDH Swaged	976	548.1	8.5E-03
HDH Swaged	1095	460.4	8.5E-03
HDH Swaged	1201	384.1	8.5E-03
HDH Swaged	1319	301.3	8.5E-03

Table C.2.3. *Tensile Test Data for Cb-752*

Cb-752			
[97]			
Recrystallized Cb-752			
Test Temp (˚C)	**Stress (psi)**	**Stress (MPa)**	**Strain Rate (1/s)**
1093	37900	261	8.33E-04
1093	38300	264	8.33E-04
1093	38200	263	8.33E-04
1371	21300	147	8.33E-04
1371	21500	148	8.33E-04
1371	21500	148	8.33E-04
1482	17200	119	8.33E-04
1482	15200	105	8.33E-04
1482	17200	119	8.33E-04
1649	9450	65	8.33E-04
1649	8950	62	8.33E-04
1649	7950	55	8.33E-04
1482	16900	117	8.33E-04
1482	17100	118	8.33E-04
1482	17000	117	8.33E-04
[100]			
Cb-752 Bar			
Test Temp (˚C)	**Stress (ksi)**	**Stress (MPa)**	**Strain Rate (1/s)**
399	58	402.7	8.3E-04
399	60	410.2	8.3E-04
399	62	429.5	8.3E-04
538	53	362.0	8.3E-04
538	56	383.3	8.3E-04
538	56	383.3	8.3E-04
1093	39	269.6	8.3E-04
1093	36	251.0	8.3E-04
1093	35	242.0	8.3E-04

1316	21	141.3	8.3E-04
1316	26	182.0	8.3E-04
1316	26	178.6	8.33E-04
Annealed Cb-752			
Test Temp (˚C)	**Stress (ksi)**	**Stress (MPa)**	**Strain Rate (1/s)**
1204	26	180.6	3.3E-04
1204	27	184.1	3.3E-04
1204	34	235.8	3.3E-04
1204	32	218.6	3.3E-04
1204	36	244.8	8.3E-04
1204	38	262.0	8.3E-04
1204	35	240.6	8.3E-04
1204	34	233.7	8.3E-04
1204	33	224.8	8.3E-04
1204	31	210.3	8.3E-04
1204	33	228.2	8.3E-04
1204	31	213.7	8.3E-04
Cb-752 Sheet			
Test Temp (˚C)	**Stress (ksi)**	**Stress (MPa)**	**Strain Rate (1/s)**
1093	43	295.8	8.3E-04
1093	41	285.4	8.3E-04
1204	34	231.0	8.3E-04
1204	30	204.1	8.3E-04
1204	33	229.6	8.3E-04
1316	23	159.3	8.3E-04
1316	23	157.9	8.3E-04
538	54	370.9	8.3E-04
1093	42	289.6	8.3E-04
1204	36	248.2	8.3E-04
1316	27	185.5	8.3E-04
Recrystallized Cb-752			

Test Temp (˚C)	**Stress (ksi)**	**Stress (MPa)**	**Strain Rate (1/s)**
1482	17	116.5	8.3E-04
1482	17	117.9	8.3E-04
1482	17	117.2	8.3E-04
[98]			
Cb-752 Sheet			
Test Temp (˚C)	**Stress (ksi)**	**Stress (MPa)**	**Strain Rate (1/s)**
1093	46	319.2	3.3E-04
1316	24	163.4	3.3E-04

Table C.2.4. *Tensile Test Data for D-43*

D-43			
[101]			
Annealed Base Metal			
Test Temp (˚C)	**Stress (ksi)**	**Stress (MPa)**	**Strain Rate (1/s)**
982	54	375.7	8.3E-04
1146	43	296.7	8.3E-04
1316	32	220.6	8.3E-04
Welded Metal			
Test Temp (˚C)	Stress (ksi)	Stress (MPa)	Strain Rate (1/s)
982	55	380.5	8.3E-04
1154	43	298.6	8.3E-04
1325	32	218.7	8.3E-04
[98]			
Sheet			
Test Temp (˚C)	**Stress (ksi)**	**Stress (MPa)**	**Strain Rate (1/s)**
1093	43	298.5	3.3E-04
1316	26	180.6	3.3E-04
[100]			

Stress Relieved			
Test Temp (˚C)	**Stress (ksi)**	**Stress (MPa)**	**Strain Rate (1/s)**
1093	46	317.2	8.3E-04
1093	48	330.9	8.3E-04
1204	34	234.4	8.3E-04
1204	37	255.1	8.3E-04
1316	24	165.5	8.3E-04
1316	27	186.2	8.3E-04
1427	12	82.7	8.3E-04
1427	16	106.9	8.3E-04
1204	31	210.3	8.3E-04
1204	30	206.8	8.3E-04
1204	37	255.1	8.3E-04
1204	37	255.1	8.3E-04
1204	37	255.1	8.3E-04
1204	37	253.7	8.3E-04

Table C.2.5. *Tensile Test Data for FS-85*

FS-85			
[101]			
Annealed Base Metal			
Test Temp (˚C)	**Stress (ksi)**	**Stress (MPa)**	**Strain Rate (1/s)**
980	44	305.4	8.3E-04
1148	34	237.0	8.3E-04
1314	22	155.1	8.3E-04
Welded Metal			
Test Temp (˚C)	**Stress (ksi)**	**Stress (MPa)**	**Strain Rate (1/s)**
982	40	277.4	8.3E-04
1148	33	226.4	8.3E-04
1316	23	160.9	8.3E-04
[100]			
Stress Relieved			
Test Temp (˚C)	**Stress (ksi)**	**Stress (MPa)**	**Strain Rate (1/s)**
201	106	732.6	8.3E-04
435	99	681.6	8.3E-04
639	90	623.3	8.3E-04
861	79	543.1	8.3E-04
1095	59	406.4	8.3E-04
1337	24	167.7	8.3E-04
1538	14	98.4	8.3E-04
1760	10	65.6	8.3E-04
Recrystallized			
Test Temp (˚C)	**Stress (ksi)**	**Stress (MPa)**	**Strain Rate (1/s)**
210	76	526.7	8.3E-04
438	68	472.0	8.3E-04
645	67	462.9	8.3E-04
864	60	411.9	8.3E-04
1097	44	300.7	8.3E-04

1334	24	164.0	8.3E-04
1538	15	102.1	8.3E-04
1755	9	63.8	8.3E-04
207	68	472.0	8.3E-04
438	60	415.5	8.3E-04
642	60	413.7	8.3E-04
861	53	366.3	8.3E-04
1095	38	260.6	8.3E-04
1328	19	133.0	8.3E-04
[102]			
Annealed			
Test Temp (˚C)	**Stress (psi)**	**Stress (MPa)**	**Strain Rate (1/s)**
30	87700	604.7	1.0E-03
400	48300	333.0	1.0E-03
Rolled			
Test Temp (˚C)	**Stress (psi)**	**Stress (MPa)**	**Strain Rate (1/s)**
30	119200	821.9	1.0E-03
400	79200	546.1	1.0E-03
Shock Loaded			
Test Temp (˚C)	**Stress (psi)**	**Stress (MPa)**	**Strain Rate (1/s)**
30	91400	630.2	1.0E-03
400	60700	418.5	1.0E-03

Table C.2.6. *Tensile Test Data for C-129(Y)*

C-129(Y)			
[28]			
Test Temp (˚C)	**Stress (psi)**	**Stress (MPa)**	**Strain Rate (1/s)**
316	59000	406.8	8.3E-04
316	66300	457.1	8.3E-04

649	59100	407.5	8.3E-04
649	66100	455.7	8.3E-04
982	52200	359.9	8.3E-04
1093	41500	286.1	8.3E-04
1093	40800	281.3	8.3E-04
1093	38200	263.4	8.3E-04
1093	38700	266.8	8.3E-04
1316	22300	153.8	8.3E-04
1316	22600	155.8	8.3E-04
1316	24600	169.6	8.3E-04
1316	24900	171.7	8.3E-04
1316	23700	163.4	8.3E-04
1316	23800	164.1	8.3E-04
1316	21200	146.2	8.3E-04
1316	25300	174.4	8.3E-04
1316	25600	176.5	8.3E-04
1316	25700	177.2	8.3E-04
1316	24100	166.2	8.3E-04
1316	23800	164.1	8.3E-04
1371	22000	151.7	8.3E-04
1371	22400	154.4	8.3E-04
1371	20600	142.0	8.3E-04
1371	19600	135.1	8.3E-04
1649	11700	80.7	8.3E-04
1649	11100	76.5	8.3E-04
1649	10300	71.0	8.3E-04
1649	11200	77.2	8.3E-04
1649	9450	65.2	8.3E-04
1927	5800	40.0	8.3E-04
1927	5050	34.8	8.3E-04
1927	5200	35.9	8.3E-04

Table C.2.7. *Tensile Test Data for ASTAR-811C*

ASTAR-811C		
[77]		
Strain Rate (1/s)	**Stress (MPa)**	**Test Temp (˚C)**
8.3E-04	370.2	316
8.3E-04	284.8	816
8.3E-04	241.3	1093
8.3E-04	217.9	1204
8.3E-04	209.6	1316
8.3E-04	203.4	1427
8.3E-04	158.6	1538
[103]		
Strain Rate (1/s)	**Stress (MPa)**	**Test Temp (˚C)**
8.3E-04	462.6	982
8.3E-04	283.4	1316
8.3E-04	248.2	1427

Table C.2.8. *Tensile Test Data for Stress-Relieved (SR) and Recrystallized (Rx) TZM*

TZM SR			TZM Rx		
[104]			[105]		
Strain Rate (1/s)	**Stress (MPa)**	**Test Temp (˚C)**	**Strain Rate (1/s)**	**Stress (MPa)**	**Test Temp (˚C)**
1.0E-05	732.7	21	1.0E-03	312.9	900
1.0E-05	757.1	21	3.4E-01	322.0	900
1.0E-04	779.6	21	6.7E-01	331.8	900
1.0E-03	857.1	21	1.0E+00	340.9	900
1.0E-02	908.2	21	1.0E-03	362.1	800
1.0E-02	926.5	21	3.3E-01	367.4	800
1.1E-01	991.8	21	6.7E-01	375.0	800
1.0E-05	628.6	350	1.0E+00	387.1	800
1.1E-03	624.5	350	1.0E-03	353.0	700

1.0E-02	616.3	350
1.0E-01	632.7	350
1.0E-04	630.6	400
1.0E-03	598.0	400
1.1E-02	616.3	400
1.0E-01	618.4	400
1.0E-04	606.1	450
1.0E-03	559.2	450
1.0E-02	583.7	450
1.1E-01	598.0	450
1.0E-03	829.4	23
1.0E-03	758.8	76
1.0E-03	678.2	151
1.0E-03	654.2	252
1.0E-03	634.0	349
1.0E-03	615.1	450

3.4E-01	359.1	700
6.7E-01	367.4	700
1.0E+00	377.3	700
1.2E-03	370.5	600
3.4E-01	377.3	600
6.7E-01	386.4	600
1.0E+00	400.0	600

[36]

Strain Rate (1/s)	**Stress (MPa)**	**Test Temp (˚C)**
1.4E-08	255.1	982
6.9E-06	275.8	982
1.0E-07	275.8	982
1.6E-07	186.2	1093
1.9E-07	227.5	1093
1.9E-07	24.1	1649
6.1E-06	34.5	1649
1.3E-07	241.3	982
3.1E-06	275.8	982

Table C.2.9. *Tensile Test Data for MAR-M247 and Haynes 230*

MAR-M247		
[81]		
Strain Rate (1/s)	**Stress (MPa)**	**Test Temp (˚C)**
1.3E-04	1121	25
1.3E-04	1139	25
1.3E-04	1146	760
1.3E-04	1176	760
1.3E-04	590	982
1.3E-04	613	982

Haynes 230		
[106]		
Strain Rate (1/s)	**Stress (MPa)**	**Test Temp (˚C)**
1.0E-03	819.9	22
1.0E-03	794.0	198
1.0E-03	786.9	298
1.0E-03	765.7	400
1.0E-03	692.7	598
1.0E-03	619.6	700
1.0E-03	395.8	796
1.0E-03	294.5	849
1.0E-03	216.8	900
1.0E-03	169.6	951
1.0E-04	881.2	22
1.0E-04	711.5	601
1.0E-04	292.1	799
1.0E-04	113.1	952
1.0E-05	862.3	22
1.0E-05	631.4	601
1.0E-05	181.4	799
1.0E-05	70.7	952

C.3 Steady-State Creep Rate Data

Table C.3.1. *Steady-State Creep Rate Data for C103*

C103							
[73]							
Wrought 1593˚C		**Wrought 1650˚C**		**Wrought 1693˚C**		**HIP 1650˚C**	
Stress (MPa)	**Strain Rate (1/s)**	**Stress (MPa)**	**Strain Rate (1/s)**	**Stress (MPa)**	**Strain Rate (1/s)**	**Stress (MPa)**	**Strain Rate (1/s)**
12.4	7.20E-06	12.4	1.00E-05	12.4	1.79E-05	12.4	1.16E-05
13.8	8.33E-06	13.8	1.92E-05	13.8	2.78E-05	13.8	1.50E-05
16.5	1.67E-05	16.5	3.00E-05	16.5	5.50E-05	16.5	3.00E-05
[171]							
Cast 1093˚C		**Cast 1204˚C**		**Cast 1316˚C**			
Strain Rate (1/s)	**Stress (MPa)**	**Strain Rate (1/s)**	**Stress (MPa)**	**Strain Rate (1/s)**	**Stress (MPa)**		
5.74E-08	108.2	9.83E-08	86.0	4.05E-07	43.9		
5.27E-08	121.1	8.96E-08	78.5	8.96E-08	27.1		
2.78E-08	100.3	4.49E-08	60.2				
[87]							
Wrought/Annealed 927˚C		**Wrought/Annealed 977˚C**		**Wrought/Annealed 1002˚C**		**Wrought/Annealed 1027˚C**	
Strain Rate (1/s)	**Stress (MPa)**	**Strain Rate (1/s)**	**Stress (MPa)**	**Strain Rate (1/s)**	**Stress (MPa)**	**Strain Rate (1/s)**	**Stress (MPa)**
3.68E-10	55.2	6.34E-10	41.4	3.91E-10	27.6	2.68E-10	20.7
8.47E-10	82.7	8.04E-10	50.1	1.19E-09	34.5	3.15E-09	41.4
1.64E-10	68.9	5.68E-10	60.1			6.64E-09	55.2
6.54E-10	62.1						
Wrought/Annealed 982˚C		**Wrought/Annealed 1093˚C**		**Wrought/Annealed 1149˚C**		**Wrought/Annealed 1204˚C**	
Strain Rate (1/s)	**Stress (MPa)**	**Strain Rate (1/s)**	**Stress (MPa)**	**Strain Rate (1/s)**	**Stress (MPa)**	**Strain Rate (1/s)**	**Stress (MPa)**
1.79E-09	48.3	1.58E-09	20.7	7.85E-10	10.3	4.76E-10	6.89
1.12E-09	48.3	3.92E-10	13.8	2.09E-09	13.8	1.5E-09	10.3
1.12E-09	48.3	1.46E-09	17.2	4.36E-09	20.7		
1.07E-10	20.7	8.12E-09	34.5	2.62E-08	34.5		
2.83E-10	34.5						

9.68E-10	48.3	
1.14E-09	48.3	
1.48E-09	48.3	
8.38E-10	41.4	
Unknown Processing		
Strain Rate (1/s)	**Stress (MPa)**	**T (˚C)**
2.1E-10	17.2	1052
1.67E-10	138	827
1.39E-10	34.5	954
1.38E-10	89.6	871

Table C.3.2. *Steady-State Creep Rate Data for WC-3009*

WC-3009	
[62].	
Hot Pressed 1317˚C	
Stress (MPa)	**Strain Rate (1/s)**
14.7	1.07E-07
23.9	4.59E-07
29.4	6.62E-07
34.3	1.63E-06
41.1	2.73E-06
Hot Pressed 1257˚C	
Stress (MPa)	**Strain Rate (1/s)**
27.8	3.16E-07
34.3	7.19E-07
41.0	9.37E-07
Hot Pressed 1207˚C	
Stress (MPa)	**Strain Rate (1/s)**

Table C.3.3. *Steady-State Creep Rate Data for C-129(Y)*

C-129(Y)		
[95]		
Test Temp (˚C)	**Stress (MPa)**	**Strain Rate (1/s)**
980	42.3	2.7E-08
980	106.2	4.3E-07
980	141.3	2.0E-06
980	244.0	1.1E-05
1095	56.7	4.6E-07
1095	87.3	2.9E-06
1095	174.7	1.3E-05
1205	8.5	5.2E-09
1205	35.3	6.0E-07
1205	70.1	5.7E-06
1205	140.2	2.5E-05

27.4	1.25E-07
34.2	2.56E-07
41.0	4.47E-07
54.7	1.53E-06
68.7	2.58E-06

Table C.3.4. *Steady-State Creep Rate Data for Cb-752*

Cb-752			
[75]			
Wrought 982˚C			
Stress (psi)	**Stress (MPa)**	**Strain Rate (1/hr)**	**Strain Rate (1/s)**
13885	95.7	3.47E-05	9.63E-09
18798	129.6	1.30E-04	3.62E-08
24806	171.0	6.07E-04	1.69E-07
34538	238.1	1.60E-02	4.43E-06
Wrought 1093˚C			
Stress (psi)	**Stress (MPa)**	**Strain Rate (1/hr)**	**Strain Rate (1/s)**
9001	62.1	1.58E-04	4.38E-08
12473	86.0	3.81E-04	1.06E-07
17447	120.3	1.39E-03	3.87E-07
22337	154.0	7.24E-03	2.01E-06
Wrought 1204˚C			
Stress (psi)	**Stress (MPa)**	**Strain Rate (1/hr)**	**Strain Rate (1/s)**
6028	41.6	1.80E-04	5.01E-08
8980	61.9	1.05E-03	2.91E-07
12300	84.8	3.74E-03	1.04E-06
14890	102.7	1.00E-02	2.79E-06
[96]			
Sheet 1204˚C			
Stress (psi)	**Stress (MPa)**	**Strain Rate (1/hr)**	**Strain Rate (1/s)**

20000	137.9	1.90E-01	5.28E-05
18000	124.1	1.57E-02	4.36E-06
15000	103.4	3.40E-03	9.44E-07
14000	96.5	2.00E-03	5.56E-07
13000	89.6	8.30E-04	2.31E-07

Table C.3.5. *Steady-State Creep Rate Data for D-43*

D-43			
[76]			
Stress Relieved 980˚C			
Stress (psi)	**Stress (MPa)**	**Strain Rate (1/hr)**	**Strain Rate (1/s)**
18249	125.8	3.27E-05	9.09E-09
19806	136.6	6.66E-05	1.85E-08
21350	147.2	1.55E-04	4.31E-08
22091	152.3	2.04E-04	5.66E-08
24640	169.9	5.53E-04	1.54E-07
26743	184.4	1.07E-03	2.97E-07
33497	231.0	7.76E-03	2.15E-06
Stress Relieved 1090˚C			
Stress (psi)	**Stress (MPa)**	**Strain Rate (1/hr)**	**Strain Rate (1/s)**
13152	90.7	8.30E-05	2.31E-08
15075	103.9	1.69E-04	4.70E-08
14871	102.5	1.90E-04	5.29E-08
17162	118.3	6.89E-04	1.91E-07
17398	120.0	1.33E-03	3.70E-07
22548	155.5	3.06E-03	8.49E-07
22091	152.3	4.08E-03	1.13E-06
24141	166.4	1.03E-02	2.87E-06
Stress Relieved 1204˚C			
Stress (psi)	**Stress (MPa)**	**Strain Rate (1/hr)**	**Strain Rate (1/s)**
6647	45.8	4.29E-05	1.19E-08
8047	55.5	1.25E-04	3.46E-08
8914	61.5	2.00E-04	5.56E-08
8914	61.5	2.67E-04	7.42E-08
9807	67.6	3.44E-04	9.56E-08
12368	85.3	1.33E-03	3.70E-07
14770	101.8	2.72E-03	7.54E-07

16929	116.7	9.03E-03	2.51E-06	
[88]				
T (˚C)	**Stress (psi)**	**Stress (MPa)**	**Strain Rate (1/hr)**	**Strain Rate (1/s)**
1093	8476	58.4	8.30E-06	2.31E-09
1204	4271	29.4	1.20E-05	3.33E-09

Table C.3.6. *Steady-State Creep Rate Data for FS-85*

FS-85			
[75]			
Wrought 982˚C			
Stress (psi)	**Stress (MPa)**	**Strain Rate (1/hr)**	**Strain Rate (1/s)**
21039	145.1	1.63E-05	4.53E-09
22585	155.7	1.75E-05	4.85E-09
24992	172.3	3.58E-05	9.94E-09
29789	205.4	1.97E-04	5.47E-08
34443	237.5	1.42E-03	3.95E-07
Wrought 1093˚C			
Stress (psi)	**Stress (MPa)**	**Strain Rate (1/hr)**	**Strain Rate (1/s)**
9976	68.8	1.47E-05	4.10E-09
13114	90.4	4.20E-05	1.17E-08
13889	95.8	6.92E-05	1.92E-08
15011	103.5	8.91E-05	2.48E-08
17473	120.5	2.58E-04	7.17E-08
19865	137.0	1.30E-03	3.60E-07
24491	168.9	1.01E-02	2.80E-06
Wrought 1204˚C			
Stress (psi)	**Stress (MPa)**	**Strain Rate (1/hr)**	**Strain Rate (1/s)**
6975	48.1	4.53E-05	1.26E-08
6975	48.1	7.59E-05	2.11E-08
9976	68.8	1.91E-04	5.29E-08

12299	84.8	5.91E-04	1.64E-07
14710	101.4	1.63E-03	4.52E-07
15684	108.1	2.11E-03	5.87E-07
17239	118.9	9.75E-03	2.71E-06
Wrought 1427˚C			
Stress (psi)	**Stress (MPa)**	**Strain Rate (1/hr)**	**Strain Rate (1/s)**
991	6.8	1.66E-05	4.61E-09
3479	24.0	3.35E-04	9.32E-08
5892	40.6	1.91E-03	5.31E-07
7850	54.1	9.04E-03	2.51E-06
9743	67.2	2.92E-02	8.12E-06

Table C.3.7. *Steady-State Creep Rate Data for Nb-1Zr*

Nb-1Zr											
[172]											
Bulk 800˚C			**Bulk 900˚C**			**Bulk 950˚C**			**Bulk 1000˚C**		
Stress (MPa)	**Strain Rate (1/min)**	**Strain Rate (1/s)**	**Stress (MPa)**	**Strain Rate (1/min)**	**Strain Rate (1/s)**	**Stress (MPa)**	**Strain Rate (1/min)**	**Strain Rate (1/s)**	**Stress (MPa)**	**Strain Rate (1/min)**	**Strain Rate (1/s)**
59.8	2.40E-05	4.01E-07	49.7	5.68E-05	9.46E-07	50.0	7.90E-05	1.32E-06	40.0	1.84E-04	3.06E-06
69.9	3.18E-05	5.31E-07	59.8	6.27E-05	1.05E-06	60.1	1.32E-04	2.20E-06	50.0	1.99E-04	3.32E-06
80.1	3.70E-05	6.16E-07	70.2	7.90E-05	1.32E-06	70.2	1.64E-04	2.73E-06	59.9	2.28E-04	3.79E-06
89.8	5.59E-05	9.31E-07	80.4	7.90E-05	1.32E-06	79.6	2.06E-04	3.43E-06	70.2	3.50E-04	5.83E-06
100.4	6.48E-05	1.08E-06	90.1	1.10E-04	1.83E-06	90.1	2.43E-04	4.05E-06	80.4	5.37E-04	8.96E-06
110.5	7.65E-05	1.27E-06	100.1	1.19E-04	1.99E-06	100.1	2.92E-04	4.86E-06	89.8	7.60E-04	1.27E-05
120.1	9.02E-05	1.50E-06	110.5	1.32E-04	2.20E-06	110.1	3.06E-04	5.11E-06	100.1	8.82E-04	1.47E-05
129.7	9.64E-05	1.61E-06				120.1	4.95E-04	8.25E-06	110.5	1.50E-03	2.50E-05
						130.1	9.27E-04	1.55E-05	130.1	6.10E-03	1.02E-04
[96]											
Work Hardened 982˚C			**Annealed 982˚C**			**Work Hardened 1200˚C**			**Annealed 1200˚C**		
Stress (MPa)	**Strain Rate (1/min)**	**Strain Rate (1/s)**	**Stress (MPa)**	**Strain Rate (1/min)**	**Strain Rate (1/s)**	**Stress (MPa)**	**Strain Rate (1/min)**	**Strain Rate (1/s)**	**Stress (MPa)**	**Strain Rate (1/min)**	**Strain Rate (1/s)**
103.4	1.37E-02	2.28E-04	68.9	1.17E-05	1.94E-07	41.4	3.92E-02	6.53E-04	27.6	1.57E-03	2.61E-05
82.7	1.95E-02	3.25E-04				34.5	1.92E-02	3.19E-04	27.6	1.08E-03	1.81E-05
68.9	2.15E-03	3.58E-05				27.6	1.32E-03	2.20E-05			
68.9	3.07E-03	5.11E-05				20.7	7.62E-04	1.27E-05			
58.6	1.68E-03	2.81E-05				20.7	2.38E-04	3.97E-06			

Table C.3.8. *Steady-State Creep Rate Data for ASTAR-811C*

ASTAR-811C					
[77]					
3000-3400˚F Heat Treatment			3600-3800F Heat Treatment		
1426˚C					
Stress (MPa)	Strain Rate (1/min)	Strain Rate (1/s)	Stress (MPa)	Strain Rate (1/min)	Strain Rate (1/s)
33.5	1.31E-04	2.19E-06	68.1	2.43E-04	4.05E-06
33.5	2.52E-05	4.20E-07	85.8	4.61E-04	7.69E-06
51.7	2.14E-04	3.56E-06	85.2	5.62E-04	9.36E-06
51.1	1.55E-04	2.58E-06	85.2	6.15E-04	1.02E-05
51.1	4.08E-04	6.81E-06	86.4	6.62E-04	1.10E-05
68.7	3.26E-04	5.43E-06	102.8	1.06E-03	1.76E-05
68.1	4.97E-04	8.28E-06	104.0	1.47E-03	2.45E-05
69.4	6.74E-04	1.12E-05	104.6	1.56E-03	2.60E-05
69.4	8.98E-04	1.50E-05			
86.4	1.22E-03	2.04E-05			
87.6	1.41E-03	2.35E-05			
88.2	1.58E-03	2.64E-05			
87.6	1.83E-03	3.05E-05			
105.9	2.00E-03	3.33E-05			
88.8	2.81E-03	4.69E-05			
106.5	3.15E-03	5.26E-05			
3000-3400˚F Heat Treatment			3600-3800˚F Heat Treatment		
1204˚C					
Stress (MPa)	Strain Rate (1/min)	Strain Rate (1/s)	Stress (MPa)	Strain Rate (1/min)	Strain Rate (1/s)
154.5	1.37E-04	2.29E-06	155.1	4.29E-05	7.15E-07
172.2	1.84E-04	3.07E-06	157.6	3.70E-05	6.17E-07
172.2	4.02E-04	6.71E-06	159.4	6.65E-05	1.11E-06
172.2	4.50E-04	7.49E-06	170.3	2.55E-04	4.25E-06
172.8	4.73E-04	7.89E-06	173.4	2.43E-04	4.05E-06
172.8	5.79E-04	9.65E-06	169.1	3.26E-04	5.43E-06
			174.6	3.38E-04	5.63E-06

3000-3400˚F Heat Treatment			3600-3800˚F Heat Treatment		
1316˚C					
Stress (MPa)	Strain Rate (1/min)	Strain Rate (1/s)	Stress (MPa)	Strain Rate (1/min)	Strain Rate (1/s)
84.6	1.20E-04	1.99E-06	84.6	4.29E-05	7.15E-07
85.2	1.02E-04	1.70E-06	102.8	1.49E-04	2.48E-06
84.0	6.65E-05	1.11E-06	119.8	2.14E-04	3.56E-06
101.6	1.25E-04	2.09E-06	119.8	1.84E-04	3.07E-06
101.6	2.14E-04	3.56E-06	119.8	2.67E-04	4.45E-06
103.4	2.26E-04	3.76E-06	121.7	2.96E-04	4.94E-06
103.4	2.79E-04	4.64E-06	102.8	4.88E-05	8.13E-07
121.1	3.67E-04	6.12E-06	137.5	4.50E-04	7.49E-06
119.8	2.96E-04	4.94E-06	138.1	5.67E-04	9.46E-06
120.5	4.44E-04	7.39E-06	138.1	6.03E-04	1.00E-05
120.5	4.73E-04	7.89E-06	138.1	6.44E-04	1.07E-05
121.1	5.14E-04	8.57E-06	157.0	1.60E-03	2.66E-05
121.1	6.97E-04	1.16E-05	157.0	1.64E-03	2.73E-05
120.5	7.50E-04	1.25E-05	157.6	1.98E-03	3.30E-05
138.1	7.56E-04	1.26E-05	156.3	2.14E-03	3.57E-05
139.3	8.39E-04	1.40E-05	158.2	2.15E-03	3.58E-05
138.1	1.17E-03	1.95E-05			
138.7	1.20E-03	2.00E-05			
139.3	1.40E-03	2.33E-05			
138.7	1.52E-03	2.53E-05			
139.3	1.55E-03	2.59E-05			
139.9	1.62E-03	2.69E-05			
157.0	2.32E-03	3.86E-05			
158.2	2.81E-03	4.69E-05			
158.2	3.15E-03	5.25E-05			
158.8	3.30E-03	5.49E-05			

Table C.3.9. *Steady-State Creep Rate Data for Stress-Relieved (SR) and Recrystallized (Rx) TZM*

TZM SR			TZM Rx		
[79]					
Strain Rate (1/s)	**Stress (MPa)**	**T (˚C)**	**Strain Rate (1/s)**	**Stress (MPa)**	**T (˚C)**
1.97E-10	303.0	983	1.97E-10	303.0	983
2.31E-09	82.7	1093	2.31E-09	82.7	1093
9.72E-11	69.0	1093	9.72E-11	69.0	1093
5.56E-11	69.0	1093	5.56E-11	69.0	1093
1.22E-08	283.0	1093	1.22E-08	283.0	1093
1.72E-09	283.0	1093	1.72E-09	283.0	1093
[78]					
Strain Rate (1/s)	**Stress (MPa)**	**T (˚C)**	**Strain Rate (1/s)**	**Stress (MPa)**	**T (˚C)**
1.35E-09	110.0	1094	1.35E-09	110.0	1094
1.95E-08	110.0	1205	1.95E-08	110.0	1205
5.58E-08	55.8	1315	5.58E-08	55.8	1315
5.11E-08	45.8	1315	5.11E-08	45.8	1315
4.28E-08	40.7	1371	4.28E-08	40.7	1371
7.56E-08	27.1	1426	7.56E-08	27.1	1426
9.39E-08	27.1	1426	9.39E-08	27.1	1426
9.22E-08	17.5	1537	9.22E-08	17.5	1537
1.46E-08	8.7	1537	1.46E-08	8.7	1537
1.64E-08	8.7	1537	1.64E-08	8.7	1537
2.16E-08	11.4	1537	2.16E-08	11.4	1537
1.59E-08	8.8	1537	1.59E-08	8.8	1537
[36]					
Strain Rate (1/s)	**Stress (MPa)**	**T (˚C)**	**Strain Rate (1/s)**	**Stress (MPa)**	**T (˚C)**
3.61E-07	482.6	982	1.39E-08	255.1	982
9.17E-08	482.6	982	6.94E-06	275.8	982
8.33E-08	496.4	982	1.03E-07	275.8	982
2.50E-07	530.9	982	1.64E-07	186.2	1093
2.78E-09	344.7	1093	1.94E-07	227.5	1093

5.00E-08	413.7	1093	1.94E-07	24.1	1649
3.61E-07	448.2	982	6.11E-06	34.5	1649
			1.28E-07	241.3	982
			3.06E-06	275.8	982

[104]		
Strain Rate (1/s)	**Stress (MPa)**	**T (˚C)**
1.03E-05	732.7	21
1.02E-05	757.1	21
1.01E-04	779.6	21
1.03E-03	857.1	21
1.02E-02	908.2	21
1.04E-02	926.5	21
1.05E-01	991.8	21
1.00E-05	628.6	350
1.06E-03	624.5	350
1.02E-02	616.3	350
1.04E-01	632.7	350
1.01E-04	630.6	400
1.03E-03	598.0	400
1.06E-02	616.3	400
1.04E-01	618.4	400
1.05E-04	606.1	450
1.01E-03	559.2	450
1.02E-02	583.7	450
1.05E-01	598.0	450

Table C.3.10. *Steady-State Creep Rate Data for Ta-10W*

Ta-10W			
[88]			
Cold Rolled 1093˚C			
Stress (psi)	**Stress (MPa)**	**Strain Rate (1/hr)**	**Strain Rate (1/s)**
15900	109.6	6.40E-06	1.78E-09
Cold Rolled 1204˚C			
Stress (psi)	**Stress (MPa)**	**Strain Rate (1/hr)**	**Strain Rate (1/s)**
8000	55.2	9.40E-06	2.61E-09

Table C.3.11. *Steady-State Creep Rate Data for Haynes 230*

Haynes 230			
[80]			
800˚C		**900˚C**	
Stress (MPa)	**Strain Rate (1/s)**	**Stress (MPa)**	**Strain Rate (1/s)**
7.6	1.52E-08	20.0	2.21E-08
15.7	1.86E-06	30.0	2.29E-07
26.7	1.10E-06	50.2	2.29E-07
40.2	2.27E-06	69.6	2.72E-06
55.7	3.09E-05	79.7	2.43E-06
		98.5	2.11E-06
		99.5	4.27E-06

Table C.3.12. *Steady-State Creep Rate Data for In-625*

In-625					
[173]					
Deposited 600˚C			**Deposited 700˚C**		
Stress (MPa)	**Strain Rate (1/hr)**	**Strain Rate (1/s)**	**Stress (MPa)**	**Strain Rate (1/hr)**	**Strain Rate (1/s)**
400	1.12E-03	3.11E-07	200	9.03E-03	2.51E-06
450	3.14E-02	8.72E-06	250	3.01E-02	8.36E-06
500	1.16E-02	3.22E-06	350	4.58E-01	1.27E-04
			400	3.34E-01	9.28E-05
Deposited 800˚C			**Deposited 900˚C**		
Stress (MPa)	**Strain Rate (1/hr)**	**Strain Rate (1/s)**	**Stress (MPa)**	**Strain Rate (1/hr)**	**Strain Rate (1/s)**
80	1.34E-03	3.72E-07	50	2.58E-01	7.17E-05
100	1.70E-02	4.72E-06	60	6.36E-01	1.77E-04
150	1.09E-01	3.03E-05	80	2.04E-01	5.67E-05
200	3.89E-01	1.08E-04			

Table C.3.13. *Steady-State Creep Rate Data for MAR-M247*

MAR-M247							
[81]							
Heat Treatment #1 800˚C		**Heat Treatment #1 900˚C**		**Heat Treatment #1 950˚C**		**Heat Treatment #1 1000˚C**	
Stress (MPa)	**Strain Rate (1/s)**	**Stress (MPa)**	**Strain Rate (1/s)**	**Stress (MPa)**	**Strain Rate (1/s)**	**Stress (MPa)**	**Strain Rate (1/s)**
300	2.50E-10	200	1.20E-09	150	1.80E-09	100	1.70E-09
400	1.40E-09	250	5.50E-09	200	9.80E-09	150	3.60E-08
400	1.60E-09	300	2.10E-08	250	7.70E-08	200	2.60E-07
450	4.70E-09	400	2.20E-07	300	3.00E-07	250	1.50E-06
500	1.30E-08	450	1.20E-06	400	3.60E-06	300	1.30E-05
550	3.20E-08	500	2.60E-06	450	1.60E-05		
600	1.20E-07	550	5.50E-06				
650	2.20E-07						
700	7.80E-07						
750	5.80E-06						
750	5.80E-06						
Heat Treatment #2 800˚C		**Heat Treatment #2 900˚C**		**Heat Treatment #2 950˚C**		**Heat Treatment #2 1000˚C**	
Stress (MPa)	**Strain Rate (1/s)**	**Stress (MPa)**	**Strain Rate (1/s)**	**Stress (MPa)**	**Strain Rate (1/s)**	**Stress (MPa)**	**Strain Rate (1/s)**
300	9.2E-11	250	1.00E-08	150	3.20E-09	100	1.30E-09
400	1.1E-09	300	3.50E-08	200	1.70E-08	100	2.80E-09
450	4.00E-09	400	3.90E-07	200	2.00E-08	150	3.20E-08
600	8.20E-08	450	6.50E-07	250	8.90E-08	200	2.80E-07
700	1.50E-06	500	2.40E-06	300	4.20E-07	250	1.60E-06
		550	1.10E-05	400	5.90E-06	300	7.30E-06
				450	1.40E-05		

C.4 Specific Heat Capacity Data

Table C.4.1. *Specific Heat Capacity Data for C-129(Y)*

C-129(Y)	
[28]	
Test Temp (˚C)	**Cp (J/gK)**
871	0.26
1088	0.27
1316	0.29

Table C.4.2. *Specific Heat Capacity Data for Cb-752*

Cb-752	
[130]	
Test Temp (˚C)	**Cp (J/gK)**
0	0.25
38	0.25
93	0.26
204	0.26
316	0.27
427	0.28
538	0.28
649	0.28
760	0.28
871	0.28
982	0.28
1093	0.28
1204	0.28
[29]	
Test Temp (˚C)	**Cp (J/gK)**
0	0.25
538	0.28
1371	0.28

Table C.4.3. *Specific Heat Capacity Data for D-43*

D-43	
[30].	
Test Temp (˚C)	**Cp (J/gK)**
260	0.2514
1371	0.3771

Table C.4.4. *Thermo-Calc Generated Specific Heat Capacity Data for C103, WC-3009, and C-129(Y)*

C103		WC-3009		C-129(Y)	
Test Temp (˚C)	**Cp (J/gK)**	**Test Temp (˚C)**	**Cp (J/gK)**	**Test Temp (˚C)**	**Cp (J/gK)**
20	0.28	20	0.240	20	0.26
49.8	0.28	49.8	0.244	49.8	0.26
79.6	0.29	79.6	0.247	79.6	0.26
109.4	0.29	109.4	0.249	109.4	0.27
139.2	0.29	139.2	0.251	139.2	0.27
169	0.29	169	0.253	169	0.27
198.8	0.30	198.8	0.255	198.8	0.27
228.6	0.30	228.6	0.256	228.6	0.28
258.4	0.30	258.4	0.257	258.4	0.28
288.2	0.30	288.2	0.259	288.2	0.28
318	0.30	318	0.260	318	0.28
347.8	0.30	347.8	0.261	347.8	0.28
377.6	0.30	377.6	0.263	377.6	0.28
407.4	0.31	407.4	0.264	407.4	0.28
437.2	0.31	437.2	0.265	437.2	0.29
467	0.31	467	0.266	467	0.29
496.8	0.31	496.8	0.268	496.8	0.29
526.6	0.31	526.6	0.269	526.6	0.29
556.4	0.31	556.4	0.270	556.4	0.29
586.2	0.32	586.2	0.271	586.2	0.29
616	0.32	616	0.273	616	0.29
645.8	0.32	645.8	0.274	645.8	0.30
675.6	0.32	675.6	0.275	675.6	0.30
705.4	0.32	705.4	0.277	705.4	0.30
735.2	0.32	735.2	0.278	735.2	0.30
765	0.32	765	0.279	765	0.30
794.8	0.33	794.8	0.281	794.8	0.30
824.6	0.33	824.6	0.282	824.6	0.30

854.4	0.33	854.4	0.284	854.4	0.31
884.2	0.33	884.2	0.285	884.2	0.31
914	0.33	914	0.287	914	0.31
943.8	0.34	943.8	0.288	943.8	0.31
973.6	0.34	973.6	0.290	973.6	0.31
1003.4	0.34	1003.4	0.291	1003.4	0.31
1033.2	0.34	1033.2	0.293	1033.2	0.32
1063	0.34	1063	0.295	1063	0.32
1092.8	0.35	1092.8	0.297	1092.8	0.32
1122.6	0.35	1122.6	0.298	1122.6	0.32
1152.4	0.35	1152.4	0.300	1152.4	0.32
1182.2	0.35	1182.2	0.302	1182.2	0.33
1212	0.36	1212	0.304	1212	0.33
1241.8	0.36	1241.8	0.306	1241.8	0.33
1271.6	0.36	1271.6	0.308	1271.6	0.33
1301.4	0.36	1301.4	0.310	1301.4	0.34
1331.2	0.36	1331.2	0.312	1331.2	0.34
1361	0.37	1361	0.314	1361	0.34
1390.8	0.37	1390.8	0.316	1390.8	0.34
1420.6	0.37	1420.6	0.318	1420.6	0.34
1450.4	0.38	1450.4	0.321	1450.4	0.35
1480.2	0.38	1480.2	0.323	1480.2	0.35
1510	0.38	1510	0.325	1510	0.35
1539.8	0.38	1539.8	0.328	1539.8	0.35
1569.6	0.39	1569.6	0.330	1569.6	0.36
1599.4	0.39	1599.4	0.332	1599.4	0.36
1629.2	0.39	1629.2	0.335	1629.2	0.36
1659	0.40	1659	0.338	1659	0.37
1688.8	0.40	1688.8	0.340	1688.8	0.37
1718.6	0.40	1718.6	0.343	1718.6	0.37
1748.4	0.41	1748.4	0.346	1748.4	0.37
1778.2	0.41	1778.2	0.348	1778.2	0.38
1808	0.41	1808	0.351	1808	0.38

1837.8	0.42	1837.8	0.354	1837.8	0.38
1867.6	0.42	1867.6	0.357	1867.6	0.39
1897.4	0.42	1897.4	0.360	1897.4	0.39
1927.2	0.43	1927.2	0.363	1927.2	0.39
1957	0.43	1957	0.367	1957	0.40
1986.8	0.43	1986.8	0.370	1986.8	0.40
2016.6	0.44	2016.6	0.373	2016.6	0.40
2046.4	0.44	2046.4	0.376	2046.4	0.41
2076.2	0.45	2076.2	0.380	2076.2	0.41
2106	0.45	2106	0.383	2106	0.41
2135.8	0.45	2135.8	0.387	2135.8	0.42
2165.6	0.46	2165.6	0.390	2165.6	0.42
2195.4	0.46	2195.4	0.394	2195.4	0.42
2225.2	0.47	2225.2	0.398	2225.2	0.43
2255	0.47	2255	0.402	2255	0.43
2284.8	0.47	2284.8	0.406	2284.8	0.44
2314.6	0.48	2314.6	0.409	2314.6	0.44
2344.4	0.48	2344.4	0.413	2344.4	0.44
2374.2	0.49	2374.2	0.417	2374.2	0.45
2404	0.49	2404	0.422	2404	0.45
2433.8	0.50	2433.8	0.426	2433.8	0.46
2463.6	0.50	2463.6	0.430		
2493.4	0.50	2493.4	0.432		
2523.2	0.50	2523.2	0.434		
2553	0.51	2553	0.436		
2582.8	0.51	2582.8	0.437		
2612.6	0.51	2612.6	0.439		
2642.4	0.51	2642.4	0.440		
2672.2	0.51	2672.2	0.441		
2702	0.51	2702	0.443		
2731.8	0.51	2731.8	0.443		
2761.6	0.51	2761.6	0.444		
2791.4	0.51	2791.4	0.445		

2821.2	0.51	2821.2	0.445
2851	0.51	2851	0.446
2880.8	0.52	2880.8	0.446
2910.6	0.52	2910.6	0.446
2940.4	0.52	2940.4	0.446
2970.2	0.52	2970.2	0.445
3000	0.52	3000	0.445

Table C.4.5. *Thermo-Calc Generated Specific Heat Capacity Data for Cb-752, D-43, FS-5, and Nb-1Zr*

Cb-752		D-43		FS-85		Nb-1Zr	
Test Temp (˚C)	**Cp (J/gK)**	**Test Temp (˚C)**	**Cp (J/gK)**	**Test Temp (˚C)**	**Cp (J/gK)**	**Test Temp (˚C)**	**Cp (J/gK)**
20	0.27	20	0.27	20	0.23	20	0.28
49.8	0.27	49.8	0.27	49.8	0.23	49.8	0.29
79.6	0.28	79.6	0.27	79.6	0.24	79.6	0.29
109.4	0.28	109.4	0.28	109.4	0.24	109.4	0.30
139.2	0.28	139.2	0.28	139.2	0.24	139.2	0.30
169	0.28	169	0.28	169	0.24	169	0.30
198.8	0.29	198.8	0.28	198.8	0.24	198.8	0.30
228.6	0.29	228.6	0.29	228.6	0.25	228.6	0.31
258.4	0.29	258.4	0.29	258.4	0.25	258.4	0.31
288.2	0.29	288.2	0.29	288.2	0.25	288.2	0.31
318	0.29	318	0.29	318	0.25	318	0.31
347.8	0.29	347.8	0.29	347.8	0.25	347.8	0.31
377.6	0.30	377.6	0.29	377.6	0.25	377.6	0.31
407.4	0.30	407.4	0.30	407.4	0.25	407.4	0.32
437.2	0.30	437.2	0.30	437.2	0.25	437.2	0.32
467	0.30	467	0.30	467	0.26	467	0.32
496.8	0.30	496.8	0.30	496.8	0.26	496.8	0.32
526.6	0.30	526.6	0.30	526.6	0.26	526.6	0.32
556.4	0.30	556.4	0.30	556.4	0.26	556.4	0.32
586.2	0.31	586.2	0.30	586.2	0.26	586.2	0.32
616	0.31	616	0.31	616	0.26	616	0.33
645.8	0.31	645.8	0.31	645.8	0.26	645.8	0.33
675.6	0.31	675.6	0.31	675.6	0.26	675.6	0.33
705.4	0.31	705.4	0.31	705.4	0.27	705.4	0.33
735.2	0.31	735.2	0.31	735.2	0.27	735.2	0.33
765	0.32	765	0.31	765	0.27	765	0.33
794.8	0.32	794.8	0.32	794.8	0.27	794.8	0.34
824.6	0.32	824.6	0.32	824.6	0.27	824.6	0.34
854.4	0.32	854.4	0.32	854.4	0.27	854.4	0.34

884.2	0.32	884.2	0.32	884.2	0.27	884.2	0.34
914	0.32	914	0.32	914	0.28	914	0.34
943.8	0.33	943.8	0.32	943.8	0.28	943.8	0.35
973.6	0.33	973.6	0.33	973.6	0.28	973.6	0.35
1003.4	0.33	1003.4	0.33	1003.4	0.28	1003.4	0.35
1033.2	0.33	1033.2	0.33	1033.2	0.28	1033.2	0.35
1063	0.33	1063	0.33	1063	0.28	1063	0.35
1092.8	0.34	1092.8	0.33	1092.8	0.28	1092.8	0.36
1122.6	0.34	1122.6	0.34	1122.6	0.29	1122.6	0.36
1152.4	0.34	1152.4	0.34	1152.4	0.29	1152.4	0.36
1182.2	0.34	1182.2	0.34	1182.2	0.29	1182.2	0.36
1212	0.34	1212	0.34	1212	0.29	1212	0.37
1241.8	0.35	1241.8	0.35	1241.8	0.29	1241.8	0.37
1271.6	0.35	1271.6	0.35	1271.6	0.30	1271.6	0.37
1301.4	0.35	1301.4	0.35	1301.4	0.30	1301.4	0.37
1331.2	0.35	1331.2	0.35	1331.2	0.30	1331.2	0.38
1361	0.36	1361	0.35	1361	0.30	1361	0.38
1390.8	0.36	1390.8	0.36	1390.8	0.30	1390.8	0.38
1420.6	0.36	1420.6	0.36	1420.6	0.30	1420.6	0.38
1450.4	0.36	1450.4	0.36	1450.4	0.31	1450.4	0.39
1480.2	0.37	1480.2	0.37	1480.2	0.31	1480.2	0.39
1510	0.37	1510	0.37	1510	0.31	1510	0.39
1539.8	0.37	1539.8	0.37	1539.8	0.31	1539.8	0.40
1569.6	0.38	1569.6	0.37	1569.6	0.32	1569.6	0.40
1599.4	0.38	1599.4	0.38	1599.4	0.32	1599.4	0.40
1629.2	0.38	1629.2	0.38	1629.2	0.32	1629.2	0.41
1659	0.38	1659	0.38	1659	0.32	1659	0.41
1688.8	0.39	1688.8	0.38	1688.8	0.32	1688.8	0.41
1718.6	0.39	1718.6	0.39	1718.6	0.33	1718.6	0.41
1748.4	0.39	1748.4	0.39	1748.4	0.33	1748.4	0.42
1778.2	0.40	1778.2	0.39	1778.2	0.33	1778.2	0.42
1808	0.40	1808	0.40	1808	0.33	1808	0.42
1837.8	0.40	1837.8	0.40	1837.8	0.34	1837.8	0.43

1867.6	0.41	1867.6	0.40	1867.6	0.34	1867.6	0.43
1897.4	0.41	1897.4	0.41	1897.4	0.34	1897.4	0.44
1927.2	0.41	1927.2	0.41	1927.2	0.35	1927.2	0.44
1957	0.42	1957	0.41	1957	0.35	1957	0.44
1986.8	0.42	1986.8	0.42	1986.8	0.35	1986.8	0.45
2016.6	0.42	2016.6	0.42	2016.6	0.35	2016.6	0.45
2046.4	0.43	2046.4	0.42	2046.4	0.36	2046.4	0.45
2076.2	0.43	2076.2	0.43	2076.2	0.36	2076.2	0.46
2106	0.44	2106	0.43	2106	0.36	2106	0.46
2135.8	0.44	2135.8	0.44	2135.8	0.37	2135.8	0.47
2165.6	0.44	2165.6	0.44	2165.6	0.37	2165.6	0.47
2195.4	0.45	2195.4	0.44	2195.4	0.37	2195.4	0.47
2225.2	0.45	2225.2	0.45	2225.2	0.37	2225.2	0.48
2255	0.45	2255	0.45	2255	0.38	2255	0.48
2284.8	0.46	2284.8	0.46	2284.8	0.38	2284.8	0.49
2314.6	0.46	2314.6	0.46	2314.6	0.38	2314.6	0.49
2344.4	0.47	2344.4	0.46	2344.4	0.39	2344.4	0.50
2374.2	0.47	2374.2	0.47	2374.2	0.39	2374.2	0.50
2404	0.47	2404	0.47	2404	0.39	2404	0.50
2433.8	0.48	2433.8	0.48	2433.8	0.40	2433.8	0.51
2463.6	0.48	2463.6	0.48	2463.6	0.40	2463.6	0.51
2493.4	0.49	2493.4	0.48	2493.4	0.40	2493.4	0.52
2523.2	0.49	2523.2	0.48	2523.2	0.41	2523.2	0.52
2553	0.49	2553	0.49	2553	0.41	2553	0.52
2582.8	0.49	2582.8	0.49	2582.8	0.41	2582.8	0.52
2612.6	0.49	2612.6	0.49	2612.6	0.41	2612.6	0.52
2642.4	0.49	2642.4	0.49	2642.4	0.41	2642.4	0.52
2672.2	0.49	2672.2	0.49	2672.2	0.41	2672.2	0.52
2702	0.49	2702	0.49	2702	0.42	2702	0.52
2731.8	0.49	2731.8	0.49	2731.8	0.42	2731.8	0.52
2761.6	0.50	2761.6	0.49	2761.6	0.42	2761.6	0.53
2791.4	0.50	2791.4	0.49	2791.4	0.42	2791.4	0.53
2821.2	0.50	2821.2	0.49	2821.2	0.42	2821.2	0.53

2851	0.50	2851	0.50	2851	0.42	2851	0.53
2880.8	0.50	2880.8	0.50	2880.8	0.43	2880.8	0.53
2910.6	0.50	2910.6	0.50	2910.6	0.43	2910.6	0.53
2940.4	0.50	2940.4	0.50	2940.4	0.43	2940.4	0.53
2970.2	0.50	2970.2	0.50	2970.2	0.43	2970.2	0.53
3000	0.50	3000	0.50	3000	0.43	3000	0.53

Table C.4.6. *Thermo-Calc Generated Specific Heat Capacity Data for ASTAR-811C, TZM, T-111, and Ta-10W*

ASTAR-811C		TZM		T-111		Ta-10W	
Test Temp (˚C)	**Cp (J/gK)**	**Test Temp (˚C)**	**Cp (J/gK)**	**Test Temp (˚C)**	**Cp (J/gK)**	**Test Temp (˚C)**	**Cp (J/gK)**
20	0.15	20	0.25	20	0.15	20	0.15
37.4	0.15	37.4	0.25	37.4	0.15	37.4	0.15
54.8	0.15	54.8	0.25	54.8	0.15	54.8	0.15
72.2	0.15	72.2	0.26	72.2	0.15	72.2	0.15
89.6	0.15	89.6	0.26	89.6	0.15	89.6	0.15
107	0.15	107	0.26	107	0.15	107	0.15
124.4	0.15	124.4	0.26	124.4	0.15	124.4	0.15
141.8	0.15	141.8	0.26	141.8	0.15	141.8	0.15
159.2	0.15	159.2	0.27	159.2	0.15	159.2	0.15
176.6	0.15	176.6	0.27	176.6	0.15	176.6	0.15
194	0.15	194	0.27	194	0.16	194	0.15
211.4	0.15	211.4	0.27	211.4	0.16	211.4	0.15
228.8	0.16	228.8	0.27	228.8	0.16	228.8	0.15
246.2	0.16	246.2	0.27	246.2	0.16	246.2	0.16
263.6	0.16	263.6	0.27	263.6	0.16	263.6	0.16
281	0.16	281	0.27	281	0.16	281	0.16
298.4	0.16	298.4	0.28	298.4	0.16	298.4	0.16
315.8	0.16	315.8	0.28	315.8	0.16	315.8	0.16
333.2	0.16	333.2	0.28	333.2	0.16	333.2	0.16
350.6	0.16	350.6	0.28	350.6	0.16	350.6	0.16
368	0.16	368	0.28	368	0.16	368	0.16
385.4	0.16	385.4	0.28	385.4	0.16	385.4	0.16
402.8	0.16	402.8	0.28	402.8	0.16	402.8	0.16
420.2	0.16	420.2	0.28	420.2	0.16	420.2	0.16
437.6	0.16	437.6	0.28	437.6	0.16	437.6	0.16
455	0.16	455	0.28	455	0.16	455	0.16
472.4	0.16	472.4	0.29	472.4	0.16	472.4	0.16
489.8	0.16	489.8	0.29	489.8	0.16	489.8	0.16
507.2	0.16	507.2	0.29	507.2	0.16	507.2	0.16

524.6	0.16	524.6	0.29	524.6	0.16	524.6	0.16
542	0.16	542	0.29	542	0.16	542	0.16
559.4	0.16	559.4	0.29	559.4	0.16	559.4	0.16
576.8	0.16	576.8	0.29	576.8	0.17	576.8	0.16
594.2	0.17	594.2	0.29	594.2	0.17	594.2	0.16
611.6	0.17	611.6	0.29	611.6	0.17	611.6	0.16
629	0.17	629	0.29	629	0.17	629	0.17
646.4	0.17	646.4	0.29	646.4	0.17	646.4	0.17
663.8	0.17	663.8	0.30	663.8	0.17	663.8	0.17
681.2	0.17	681.2	0.30	681.2	0.17	681.2	0.17
698.6	0.17	698.6	0.30	698.6	0.17	698.6	0.17
716	0.17	716	0.30	716	0.17	716	0.17
733.4	0.17	733.4	0.30	733.4	0.17	733.4	0.17
750.8	0.17	750.8	0.30	750.8	0.17	750.8	0.17
768.2	0.17	768.2	0.30	768.2	0.17	768.2	0.17
785.6	0.17	785.6	0.30	785.6	0.17	785.6	0.17
803	0.17	803	0.30	803	0.17	803	0.17
820.4	0.17	820.4	0.30	820.4	0.17	820.4	0.17
837.8	0.17	837.8	0.30	837.8	0.17	837.8	0.17
855.2	0.17	855.2	0.31	855.2	0.17	855.2	0.17
872.6	0.17	872.6	0.31	872.6	0.17	872.6	0.17
890	0.17	890	0.31	890	0.17	890	0.17
907.4	0.17	907.4	0.31	907.4	0.17	907.4	0.17
924.8	0.17	924.8	0.31	924.8	0.17	924.8	0.17
942.2	0.17	942.2	0.31	942.2	0.17	942.2	0.17
959.6	0.17	959.6	0.31	959.6	0.17	959.6	0.17
977	0.17	977	0.31	977	0.17	977	0.17
994.4	0.17	994.4	0.31	994.4	0.17	994.4	0.17
1011.8	0.17	1011.8	0.32	1011.8	0.18	1011.8	0.17
1029.2	0.17	1029.2	0.32	1029.2	0.18	1029.2	0.17
1046.6	0.18	1046.6	0.32	1046.6	0.18	1046.6	0.17
1064	0.18	1064	0.32	1064	0.18	1064	0.17
1081.4	0.18	1081.4	0.32	1081.4	0.18	1081.4	0.18

1098.8	0.18	1098.8	0.32	1098.8	0.18	1098.8	0.18
1116.2	0.18	1116.2	0.32	1116.2	0.18	1116.2	0.18
1133.6	0.18	1133.6	0.32	1133.6	0.18	1133.6	0.18
1151	0.18	1151	0.32	1151	0.18	1151	0.18
1168.4	0.18	1168.4	0.33	1168.4	0.18	1168.4	0.18
1185.8	0.18	1185.8	0.33	1185.8	0.18	1185.8	0.18
1203.2	0.18	1203.2	0.33	1203.2	0.18	1203.2	0.18
1220.6	0.18	1220.6	0.33	1220.6	0.18	1220.6	0.18
1238	0.18	1238	0.33	1238	0.18	1238	0.18
1255.4	0.18	1255.4	0.33	1255.4	0.18	1255.4	0.18
1272.8	0.18	1272.8	0.33	1272.8	0.18	1272.8	0.18
1290.2	0.18	1290.2	0.34	1290.2	0.18	1290.2	0.18
1307.6	0.18	1307.6	0.34	1307.6	0.18	1307.6	0.18
1325	0.18	1325	0.34	1325	0.18	1325	0.18
1342.4	0.18	1342.4	0.34	1342.4	0.18	1342.4	0.18
1359.8	0.18	1359.8	0.34	1359.8	0.18	1359.8	0.18
1377.2	0.18	1377.2	0.34	1377.2	0.18	1377.2	0.18
1394.6	0.18	1394.6	0.34	1394.6	0.18	1394.6	0.18
1412	0.18	1412	0.35	1412	0.18	1412	0.18
1429.4	0.18	1429.4	0.35	1429.4	0.18	1429.4	0.18
1446.8	0.18	1446.8	0.35	1446.8	0.18	1446.8	0.18
1464.2	0.18	1464.2	0.35	1464.2	0.18	1464.2	0.18
1481.6	0.18	1481.6	0.35	1481.6	0.19	1481.6	0.18
1499	0.18	1499	0.35	1499	0.19	1499	0.18
1516.4	0.19	1516.4	0.36	1516.4	0.19	1516.4	0.18
1533.8	0.19	1533.8	0.36	1533.8	0.19	1533.8	0.18
1551.2	0.19	1551.2	0.36	1551.2	0.19	1551.2	0.19
1568.6	0.19	1568.6	0.36	1568.6	0.19	1568.6	0.19
1586	0.19	1586	0.36	1586	0.19	1586	0.19
1603.4	0.19	1603.4	0.37	1603.4	0.19	1603.4	0.19
1620.8	0.19	1620.8	0.37	1620.8	0.19	1620.8	0.19
1638.2	0.19	1638.2	0.37	1638.2	0.19	1638.2	0.19
1655.6	0.19	1655.6	0.37	1655.6	0.19	1655.6	0.19

1673	0.19	1673	0.37	1673	0.19	1673	0.19
1690.4	0.19	1690.4	0.38	1690.4	0.19	1690.4	0.19
1707.8	0.19	1707.8	0.38	1707.8	0.19	1707.8	0.19
1725.2	0.19	1725.2	0.38	1725.2	0.19	1725.2	0.19
1742.6	0.19	1742.6	0.38	1742.6	0.19	1742.6	0.19
1760	0.19	1760	0.38	1760	0.19	1760	0.19
1777.4	0.19	1777.4	0.39	1777.4	0.19	1777.4	0.19
1794.8	0.19	1794.8	0.39	1794.8	0.19	1794.8	0.19
1812.2	0.19	1812.2	0.39	1812.2	0.20	1812.2	0.19
1829.6	0.20	1829.6	0.39	1829.6	0.20	1829.6	0.19
1847	0.20	1847	0.40	1847	0.20	1847	0.20
1864.4	0.20	1864.4	0.40	1864.4	0.20	1864.4	0.20
1881.8	0.20	1881.8	0.40	1881.8	0.20	1881.8	0.20
1899.2	0.20	1899.2	0.40	1899.2	0.20	1899.2	0.20
1916.6	0.20	1916.6	0.41	1916.6	0.20	1916.6	0.20
1934	0.20	1934	0.41	1934	0.20	1934	0.20
1951.4	0.20	1951.4	0.41	1951.4	0.20	1951.4	0.20
1968.8	0.20	1968.8	0.42	1968.8	0.20	1968.8	0.20
1986.2	0.20	1986.2	0.42	1986.2	0.20	1986.2	0.20
2003.6	0.20	2003.6	0.42	2003.6	0.20	2003.6	0.20
2021	0.20	2021	0.42	2021	0.20	2021	0.20
2038.4	0.20	2038.4	0.43	2038.4	0.21	2038.4	0.20
2055.8	0.20	2055.8	0.43	2055.8	0.21	2055.8	0.20
2073.2	0.21	2073.2	0.43	2073.2	0.21	2073.2	0.21
2090.6	0.21	2090.6	0.44	2090.6	0.21	2090.6	0.21
2108	0.21	2108	0.44	2108	0.21	2108	0.21
2125.4	0.21	2125.4	0.44	2125.4	0.21	2125.4	0.21
2142.8	0.21	2142.8	0.45	2142.8	0.21	2142.8	0.21
2160.2	0.21	2160.2	0.45	2160.2	0.21	2160.2	0.21
2177.6	0.21	2177.6	0.45	2177.6	0.21	2177.6	0.21
2195	0.21	2195	0.46	2195	0.21	2195	0.21
2212.4	0.21	2212.4	0.46	2212.4	0.21	2212.4	0.21
2229.8	0.21	2229.8	0.46	2229.8	0.22	2229.8	0.21

2247.2	0.21	2247.2	0.47	2247.2	0.22	2247.2	0.21
2264.6	0.22	2264.6	0.47	2264.6	0.22	2264.6	0.22
2282	0.22	2282	0.47	2282	0.22	2282	0.22
2299.4	0.22	2299.4	0.48	2299.4	0.22	2299.4	0.22
2316.8	0.22	2316.8	0.48	2316.8	0.22	2316.8	0.22
2334.2	0.22	2334.2	0.48	2334.2	0.22	2334.2	0.22
2351.6	0.22	2351.6	0.49	2351.6	0.22	2351.6	0.22
2369	0.22	2369	0.49	2369	0.22	2369	0.22
2386.4	0.22	2386.4	0.50	2386.4	0.22	2386.4	0.22
2403.8	0.22	2403.8	0.50	2403.8	0.23	2403.8	0.22
2421.2	0.23	2421.2	0.50	2421.2	0.23	2421.2	0.22
2438.6	0.23	2438.6	0.51	2438.6	0.23	2438.6	0.23
2456	0.23	2456	0.51	2456	0.23	2456	0.23
2473.4	0.23	2473.4	0.52	2473.4	0.23	2473.4	0.23
2490.8	0.23	2490.8	0.52	2490.8	0.23	2490.8	0.23
2508.2	0.23	2508.2	0.53	2508.2	0.23	2508.2	0.23
2525.6	0.23	2525.6	0.53	2525.6	0.24	2525.6	0.23
2543	0.24	2543	0.54	2543	0.24	2543	0.23
2560.4	0.24	2560.4	0.54	2560.4	0.24	2560.4	0.24
2577.8	0.24	2577.8	0.55	2577.8	0.24	2577.8	0.24
2595.2	0.24	2595.2	0.55	2595.2	0.24	2595.2	0.24
2612.6	0.24	2612.6	0.56	2612.6	0.24	2612.6	0.24
2630	0.24	2630	0.56	2630	0.24	2630	0.24
2647.4	0.24	2647.4	0.55	2647.4	0.25	2647.4	0.24
2664.8	0.25	2664.8	0.55	2664.8	0.25	2664.8	0.25
2682.2	0.25	2682.2	0.54	2682.2	0.25	2682.2	0.25
2699.6	0.25	2699.6	0.54	2699.6	0.25	2699.6	0.25
2717	0.25	2717	0.53	2717	0.25	2717	0.25
2734.4	0.25	2734.4	0.53	2734.4	0.25	2734.4	0.25
2751.8	0.25	2751.8	0.52	2751.8	0.26	2751.8	0.25
2769.2	0.26	2769.2	0.52	2769.2	0.26	2769.2	0.26
2786.6	0.26	2786.6	0.52	2786.6	0.26	2786.6	0.26
2804	0.26	2804	0.52	2804	0.26	2804	0.26

2821.4	0.26	2821.4	0.51	2821.4	0.26	2821.4	0.26
2838.8	0.26	2838.8	0.51	2838.8	0.27	2838.8	0.26
2856.2	0.27	2856.2	0.51	2856.2	0.27	2856.2	0.27
2873.6	0.27	2873.6	0.51	2873.6	0.27	2873.6	0.27
2891	0.27	2891	0.50	2891	0.27	2891	0.27
2908.4	0.27	2908.4	0.50	2908.4	0.27	2908.4	0.27
2925.8	0.27	2925.8	0.50	2925.8	0.28	2925.8	0.27
2943.2	0.28	2943.2	0.50	2943.2	0.28	2943.2	0.28
2960.6	0.28	2960.6	0.50	2960.6	0.28	2960.6	0.28
2978	0.28	2978	0.49	2978	0.28	2978	0.28
2995.4	0.28	2995.4	0.49	2995.4	0.28	2995.4	0.28
3012.8	0.28	3012.8	0.49	3012.8	0.28	3012.8	0.28
3030.2	0.29	3030.2	0.49	3030.2	0.29	3030.2	0.29
3047.6	0.29	3047.6	0.49	3047.6	0.29	3047.6	0.29
3065	0.29	3065	0.49	3065	0.29	3065	0.29
3082.4	0.29	3082.4	0.49	3082.4	0.29	3082.4	0.29
3099.8	0.29	3099.8	0.49	3099.8	0.29	3099.8	0.29
3117.2	0.29	3117.2	0.49	3117.2	0.30	3117.2	0.29
3134.6	0.30	3134.6	0.49	3134.6	0.30	3134.6	0.30
3152	0.30	3152	0.49	3152	0.30	3152	0.30
3169.4	0.30	3169.4	0.49	3169.4	0.30	3169.4	0.30
3186.8	0.30	3186.8	0.49	3186.8	0.30	3186.8	0.30
3204.2	0.30	3204.2	0.49	3204.2	0.30	3204.2	0.30
3221.6	0.30	3221.6	0.48	3221.6	0.30	3221.6	0.30
3239	0.30	3239	0.48	3239	0.31	3239	0.31
3256.4	0.31	3256.4	0.48	3256.4	0.31	3256.4	0.31
3273.8	0.31	3273.8	0.48	3273.8	0.31	3273.8	0.31
3291.2	0.31	3291.2	0.48	3291.2	0.31	3291.2	0.31
3308.6	0.31	3308.6	0.48	3308.6	0.31	3308.6	0.31
3326	0.31	3326	0.48	3326	0.31	3326	0.31
3343.4	0.31	3343.4	0.48	3343.4	0.31	3343.4	0.31
3360.8	0.31	3360.8	0.48	3360.8	0.31	3360.8	0.31
3378.2	0.31	3378.2	0.48	3378.2	0.31	3378.2	0.31

3395.6	0.31	3395.6	0.48	3395.6	0.31	3395.6	0.32
3413	0.31	3413	0.48	3413	0.31	3413	0.32
3430.4	0.31	3430.4	0.48	3430.4	0.32	3430.4	0.32
3447.8	0.32	3447.8	0.49	3447.8	0.32	3447.8	0.32
3465.2	0.32	3465.2	0.49	3465.2	0.32	3465.2	0.32
3482.6	0.32	3482.6	0.49	3482.6	0.32	3482.6	0.32

C.5 Thermal Conductivity Data

Table C.5.1. *Thermal Conductivity Data for C103*

C103	
[16]	
Test Temp (˚C)	**κ (W/mC)**
800	37.4
1200	42.4
[145]	
Test Temp (˚C)	**κ (W/mC)**
19	52.3
871	38.1
1113	40.6
1304	44.6

Table C.5.2. *Thermal Conductivity Data for C-129(Y)*

C-129(Y)				
[28]				
Test Temp (˚F)	**Test Temp (˚C)**	**k (BTU/ft^2/ft/hr/F)**	**k (BTU/ft^2/in/hr/F)**	**κ (W/mK)**
1625	885	38.3	459.6	66.2
2020	1104	40.8	489.6	70.5
2445	1341	44.4	532.8	76.7

[174]		
Test Temp (˚C)	**κ (W/cmK)**	**κ (W/mK)**
1371	0.74	74

Table C.5.3. *Thermal Conductivity Data for Cb-752*

Cb-752			
[130]			
Test Temp (˚F)	**Test Temp (˚C)**	**k (BTU ft/(hr ft2 F))**	**κ (W/mK)**
500	260	22.0	38.1
600	316	23.0	39.8
700	371	23.8	41.2
800	427	24.5	42.4
900	482	25.2	43.6
1000	538	25.8	44.6
1100	593	26.4	45.7
1200	649	26.8	46.4
1300	704	27.2	47.0
1400	760	27.6	47.7
1500	816	28.0	48.4
1600	871	28.3	48.9
1700	927	28.5	49.3
1800	982	28.6	49.5
1900	1038	28.7	49.6
2000	1093	28.8	49.8
2100	1149	28.9	50.0
2200	1204	29.0	50.2
2300	1260	29.1	50.3
2400	1316	29.2	50.5
[29]			
Test Temp (˚F)	**Test Temp (˚C)**	**k (BTU/ft^2-in-hr-F)**	**κ (W/mK)**
500	260	264.0	38.0
1500	816	336.0	48.4
2000	1093	345.6	49.8
2400	1316	350.4	50.5

Table C.5.4. *Thermal Conductivity Data for D-43*

D-43			
[135]			
Test Temp (˚F)	**Test Temp (˚C)**	**κ (BTU/hr-ft-F)**	**κ (W/mK)**
250	121	30.1	52.1
579	304	32.6	56.3
852	455	34.6	59.8
1194	646	36.5	63.1
1390	755	37.7	65.1
1621	883	39.8	68.9
1992	1089	41.3	71.4
2300	1260	42.4	73.4
2734	1501	43.4	75.1
3069	1687	45.5	78.7
3482	1917	46.1	79.7
3958	2181	47.6	82.3
[30]			
Test Temp (˚F)	**Test Temp (˚C)**	**κ (BTU/ft^2-in-hr-F)**	**κ (W/mK)**
500	260	420	60.5
2500	1371	432	62.4

Table C.5.5. *Thermal Conductivity Data for FS-85*

FS-85			
[135]			
Test Temp (˚F)	**Test Temp (˚C)**	**κ (BTU/hr-ft-F)**	**κ (W/mK)**
250	121	26.5	45.9
507	264	27.1	46.8
825	441	28.2	48.8
1103	595	29.1	50.4
1421	772	30.0	52.0
1719	937	31.8	55.0
2023	1106	32.8	56.8
2382	1305	33.4	57.8
2747	1508	34.5	59.6
3180	1749	37.0	64.0
3546	1952	37.6	65.0
3844	2118	38.2	66.0
4209	2321	39.1	67.6
[16]			
Test Temp (˚C)		**κ (W/mC)**	
800		52.8	
1200		56.7	

Table C.5.6. *Thermal Conductivity Data for ASTAR-811C*

ASTAR-811C (T-111)				
[175]				
Test Temp (˚F)	**Test Temp (˚C)**	**κ (BTU ft /(ft^2 hr F))**	**κ (BTU in /(ft^2 hr F))**	**κ (W/mK)**
89	32	27.0	324.2	46.7
107	42	26.4	316.8	45.6
586	308	28.3	339.7	48.9
764	406	26.7	320.5	46.2

757	403	29.4	353.0	50.8
932	500	27.5	330.1	47.5
1187	642	30.1	361.1	52.0
1389	754	28.3	339.7	48.9
1469	798	30.4	364.8	52.5
1662	906	30.5	365.5	52.6

Table C.5.7. *Thermal Conductivity Data for TZM*

TZM	
[176]	
Test Temp (˚C)	**κ (W/mK)**
12	128.8
48	127.7
99	126.3
146	125.0
206	123.4
263	121.9
316	120.5
379	118.7
448	116.9
501	115.2
573	113.3
627	111.8
684	110.4
728	108.9
776	107.7
824	106.4
878	104.9
931	103.5
1003	101.5
1087	99.2
1146	97.3
1224	95.2
1307	93.0
1391	90.5

Table C.5.8. *Thermal Conductivity Data for MAR-M247*

MAR-M247	
[31]	
Test Temp (˚C)	**κ (W/mK)**
529	16.6
701	18.1
899	20.4
1102	24.2
1263	33.5

Table C.5.9. *Thermal Conductivity Data for Haynes 230*

Haynes 230	
[32]	
Test Temp (˚C)	**κ (W/mK)**
25	8.9
100	10.4
200	12.4
300	14.4
400	16.4
500	18.4
600	20.4
700	22.4
800	24.4
900	26.4
960	27.6
1000	28.4

Table C.5.10. *Thermal Conductivity Data for Nb-1Zr*

Nb-1Zr	
[16]	
Test Temp (˚C)	**κ (W/mC)**
800	59
1200	63.1
[134]	
Test Temp (˚C)	**κ (W/mC)**
104	46.9
152	48.0
142	48.9
156	49.2
172	49.3
186	49.5
200	48.8
233	51.0
235	54.8
273	49.0
256	49.2
275	51.3
303	52.0
338	51.8
357	52.3
374	51.7
381	53.4
401	53.4
429	52.9
448	54.8
516	52.0
546	52.6

Table C.5.11. *Thermal Conductivity Data for Pure Nb*

Pure Nb	
[139]	
Test Temp (˚C)	**κ (W/mC)**
200	56.6
200	56.5
300	58.6
400	60.7
427	59.8
500	63.2
600	65.3
727	64.4
927	67.5
1227	72.1
1727	79.1

497	54.4
469	56.5
525	55.3
542	54.8
540	57.3
561	57.9
610	55.8
645	54.8
680	55.4
638	56.9
666	56.9
673	58.1
694	60.2
745	55.7
768	57.5
806	56.3
810	57.4
801	59.3
771	64.8
843	62.0
925	62.2
967	61.3
1002	60.4
1100	61.5
1147	65.9

C.6 Elastic Modulus

Table C.6.1. *Elastic Modulus Data for C103*

C103	
[144]	
Test Temp (˚C)	**E (GPa)**
21	86.9
1371	43.4
1482	24.8
1649	10.3
[16]	
Test Temp (˚C)	**E (GPa)**
20	90.0
1200	64.0

Table C.6.2. *Elastic Modulus Data for WC-3009*

WC-3009	
[16]	
Test Temp (˚C)	**E (GPa)**
20	123

Table C.6.4. *Elastic Modulus Data for Cb-752*

Cb-752	
[145]	
Test Temp (˚C)	**E (GPa)**
13	104.1
33	103.8
80	103.4
141	102.7
199	103.1
256	102.4
307	102.0
364	100.0
[143]	
Test Temp (˚C)	**E (GPa)**

Table C.6.5. *Elastic Modulus Data for D-43*

D-43	
[146]	
Test Temp (˚C)	**E (GPa)**
24	122.7
540	113.7
816	112.3
978	112.1
1091	113.8
1372	89.7

Table C.6.6. *Elastic Modulus Data for FS-85*

FS-85	
[147]	
Test Temp (˚C)	**E (GPa)**
21	137.9
982	124.1
1093	124.1
1204	110.3
1538	103.4
1593	82.7
1649	82.7
[16]	
Test Temp (˚C)	**E (GPa)**

20	110

20	140
1200	110

Table C.6.3. *Elastic Modulus Data for C-129(Y)*

C-129(Y)		
[144]		
Test Temp (˚C)	**E (psi)**	**E (GPa)**
25	16	110.3
1093	13	91.7
1371	12	84.1
1482	10	71.7
1649	8	55.8
[28]		
Test Temp (˚C)	**E (psi)**	**E (GPa)**
25	16	112.4
982	16	112.4
1093	14	97.2
1149	14	96.5
1343	9	60.7
1371	9	58.6
1649	5	31.7

Table C.6.7. *Elastic Modulus Data for ASTAR-811C*

ASTAR-811C	
[15]	
Test Temp (˚C)	**E (GPa)**
3	187.7
104	183.2

Table C.6.8. *Elastic Modulus Data for TZM*

TZM			
[36]			
Test Temp (˚F)	**Test Temp (˚C)**	**E (psi)**	**E (GPa)**
75	24	42000000	289.6
75	24	42000000	289.6

202	179.9
300	177.7
398	172.1
502	168.7
600	165.4
701	160.9
802	156.4
906	153.1
1004	147.5
1100	145.3
1201	140.8
1296	136.3
1397	131.8
1504	127.4
1599	125.1
1694	119.6
1801	114.0

100	38	33500000	231.0
1500	816	35000000	241.3
1500	816	32000000	220.6
2000	1093	30000000	206.8
2000	1093	26500000	182.7
2500	1371	24000000	165.5
2500	1371	23000000	158.6
2500	1371	21000000	144.8
3000	1649	14200000	97.9
3000	1649	13100000	90.3

Table C.6.9. *Elastic Modulus Data for MAR-M247*

MAR-M247	
[162]	
Test Temp (˚C)	**E (GPa)**
38	194
99	187
128	184
152	181
196	176
256	170
305	165
353	160
421	153
494	145
551	139
598	134
647	129
721	121
753	118
803	111
859	105
895	101

Table C.6.10. *Elastic Modulus Data for Haynes 230*

Haynes 230	
[32]	
Test Temp (˚C)	**E (GPa)**
25	209
100	207
200	200
300	193
400	186
500	181
600	175
700	168
800	159
900	150
960	145
1000	141

Table C.6.11. *Elastic Modulus Data for Nb-1Zr*

Nb-1Zr	
[100]	
Test Temp (˚C)	**E (GPa)**
21	79.3
1371	18.6
1482	13.8
1649	5.5
25	78.3
1374	19.2
[16]	
Test Temp (˚C)	**E (GPa)**
20	80
1200	28
[161]	
Test Temp (˚C)	**E (GPa)**
20	110.3
300	108.3

C.7 Linear Coefficient of Thermal Expansion

Table C.7.1. *CTE Data for C103*

C103	
[16]	
Test Temp (˚C)	**CTE * 10^{-6} (1/˚C)**
95	6.88

Table C.7.2. *CTE Data for WC-3009*

WC-3009	
[16]	
Test Temp (˚C)	**CTE * 10^{-6} (1/˚C)**
100	7.51

Table C.7.3. *CTE Data for FS-85*

FS-85	
[16]	
Test Temp (˚C)	**CTE * 10^{-6} (1/˚C)**
200	7.14

200	7.01
317	7.10
426	7.19
537	7.28
645	7.38
759	7.46
871	7.55
982	7.73
1093	7.91
1200	8.08

200	7.80
300	8.01
400	8.11
600	8.40
800	8.69
1000	8.99
1200	9.39
1300	9.48

314	7.19
423	7.26
534	7.34
648	7.42
759	7.61
871	7.79
982	7.96
1090	8.13
1200	8.32
1316	8.49

Table C.7.4. *CTE Data for C-129(Y)*

C-129(Y)			
[28]			
Test Temp (˚F)	**Test Temp (˚C)**	**CTE * 10^{-6} (1/˚F)**	**CTE * 10^{-6} (1/˚C)**
200	93	3.80E-06	6.84E-06
400	204	3.90E-06	7.02E-06
600	316	3.90E-06	7.02E-06
800	427	4.00E-06	7.20E-06
1000	538	4.00E-06	7.20E-06
1200	649	4.10E-06	7.38E-06
1400	760	4.10E-06	7.38E-06
1600	871	4.20E-06	7.56E-06
1800	982	4.30E-06	7.74E-06
2000	1093	4.40E-06	7.92E-06
2200	1204	4.50E-06	8.10E-06

Table C.7.5. *CTE Data for Cb-752*

Cb-752			
[29]			
Test Temp (˚F)	**Test Temp (˚C)**	**CTE * 10^{-6} (1/˚F)**	**CTE * 10^{-6} (1/˚C)**
200	93	3.8	6.84
1000	538	4.0	7.20
1600	871	4.2	7.56
2200	1204	4.5	8.10

Table C.7.6. *CTE Data for D-43*

D-43			
[30]			
Test Temp (˚F)	**Test Temp (˚C)**	**CTE * 10^{-6} (1/˚F)**	**CTE * 10^{-6} (1/˚C)**
1000-2500	538-1371	4.30	7.74

Table C.7.9. *CTE Data for MAR-M247*

MAR-M247	
[177]	
Test Temp (˚C)	**CTE * 10^{-6} (1/˚C)**
800	14.23
820	14.34
840	14.46
860	14.58
880	14.71
900	14.84
920	14.98
940	15.12
960	15.28
980	15.44

Table C.7.10. *CTE Data for Haynes 230*

Haynes 230	
[32]	
Test Temp (˚C)	**CTE * 10^{-6} (1/˚C)**
100	11.80
200	12.40
300	12.80
400	13.20
500	13.60
600	14.10
700	14.70
800	15.20
900	15.70
960	15.94

Table C.7.11. *CTE Data for Nb-1Zr*

Nb-1Zr	
[16]	
Test Temp (˚C)	**CTE * 10-6 (1/˚C)**
100	6.80
203	6.87
317	6.92
428	7.01
540	7.11
648	7.19
762	7.30
871	7.40
985	7.53
1093	7.64

1000	15.61	1000	16.10	1207	7.78
				1318	7.91

Table C.7.7. *Thermo-Calc Generated CTE Data for C103, WC-3009, and C-129(Y)*

C103		**WC-3009**		**C-129(Y)**	
Test Temp (˚C)	**CTE * 10^{-6} (1/˚C)**	**Test Temp (˚C)**	**CTE * 10^{-6} (1/˚C)**	**Test Temp (˚C)**	**CTE * 10^{-6} (1/˚C)**
25	7.44	25	7.08	800	7.76
120	7.57	116	7.20	820	7.77
215	7.68	207	7.30	840	7.79
310	7.77	298	7.39	860	7.81
405	7.87	389	7.48	880	7.83
500	7.96	480	7.56	900	7.84
595	8.05	571	7.64	920	7.86
690	8.14	662	7.73	940	7.88
785	8.22	753	7.81	960	7.89
880	8.31	844	7.89	980	7.91
975	8.39	935	7.97	1000	7.93
1070	8.48	1026	8.05	1020	7.95
1165	8.56	1117	8.13	1040	7.96
1260	8.65	1208	8.21	1060	7.98
1355	8.73	1299	8.29	1080	8.00
1450	8.81	1390	8.37	1100	8.01
1545	8.90	1481	8.45	1120	8.03
1640	8.98	1572	8.53	1140	8.05
1735	9.06	1663	8.61	1160	8.07
1830	9.15	1754	8.70	1180	8.08
1925	9.23	1845	8.78	1200	8.10
2020	9.31	1936	8.86	1220	8.12
2115	9.40	2027	8.94	1240	8.13
2210	9.48	2118	9.02	1260	8.15
2305	9.57	2209	9.10	1280	8.17

2400	9.65	2300	9.19	1300	8.18
				1320	8.20
				1340	8.22
				1360	8.23
				1380	8.25
				1400	8.27
				1420	8.29
				1440	8.30
				1460	8.32
				1480	8.34
				1500	8.35
				1520	8.37
				1540	8.39
				1560	8.40
				1580	8.42
				1600	8.44
				1620	8.45
				1640	8.47
				1660	8.49
				1680	8.50
				1700	8.52

Table C.7.8. *Thermo-Calc Generated CTE Data for Cb-752, FS-85, D-43, and Nb-1Zr*

Cb-752		**D-43**		**FS-85**		**Nb-1Zr**	
Test Temp (˚C)	**CTE * 10^{-6} (1/˚C)**	**Test Temp (˚C)**	**CTE * 10^{-6} (1/˚C)**	**Test Temp (˚C)**	**CTE * 10^{-6} (1/˚C)**	**Test Temp (˚C)**	**CTE * 10^{-6} (1/˚C)**
25	7.35	25	7.35	25	7.18	25	7.50
124	7.47	124	7.47	128	7.29	124	7.63
223	7.58	223	7.57	231	7.39	223	7.74
322	7.67	322	7.67	334	7.48	322	7.84
421	7.76	421	7.76	437	7.57	421	7.93
520	7.85	520	7.84	540	7.65	520	8.02
619	7.93	619	7.93	643	7.73	619	8.11
718	8.01	718	8.01	746	7.81	718	8.19
817	8.10	817	8.09	849	7.89	817	8.27
916	8.18	916	8.17	952	7.97	916	8.35
1015	8.26	1015	8.25	1055	8.05	1015	8.44
1114	8.34	1114	8.33	1158	8.13	1114	8.52
1213	8.42	1213	8.41	1261	8.21	1213	8.60
1312	8.50	1312	8.49	1364	8.28	1312	8.68
1411	8.58	1411	8.57	1467	8.36	1411	8.76
1510	8.66	1510	8.65	1570	8.44	1510	8.84
1609	8.74	1609	8.73	1673	8.52	1609	8.92
1708	8.82	1708	8.81	1776	8.60	1708	9.00
1807	8.90	1807	8.89	1879	8.68	1807	9.08
1906	8.98	1906	8.97	1982	8.76	1906	9.16
2005	9.07	2005	9.05	2085	8.84	2005	9.24
2104	9.15	2104	9.13	2188	8.92	2104	9.32
2203	9.23	2203	9.21	2291	9.00	2203	9.40
2302	9.31	2302	9.30	2394	9.08	2302	9.48
2401	9.39	2401	9.38	2497	9.16	2401	9.56
2500	9.48	2500	9.46	2600	9.24	2500	9.65

Appendix D: Sellars-Tegart Modeling of Ni-, Mo-, and Ta-based Alloys

All creep and tensile test data collected for Ni, Mo-, and Ta-based reference alloys collapse onto a singular curve when treated with the Zener-Holloman parameter, indicating that the ST model can be used to describe the flow strengths of the alloys.

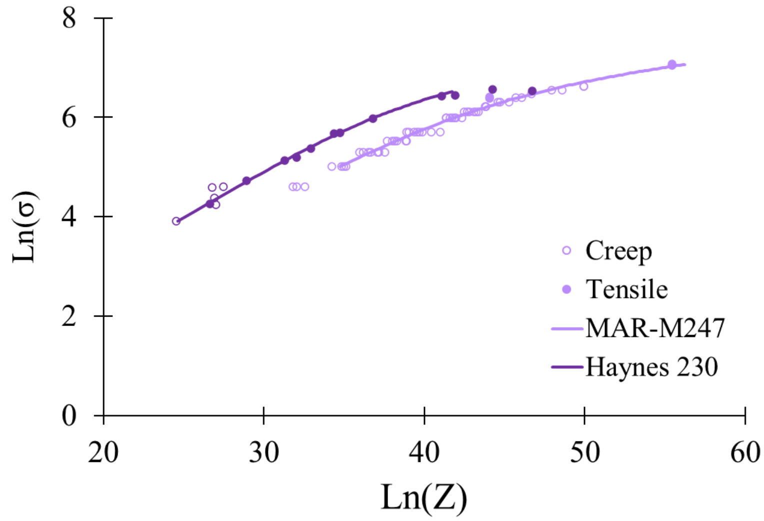

Figure D1. *Creep and tensile data for MAR-M247 and Haynes 230 collapse onto a singular curve that is described through the ST equation, indicating applicability of the model.*

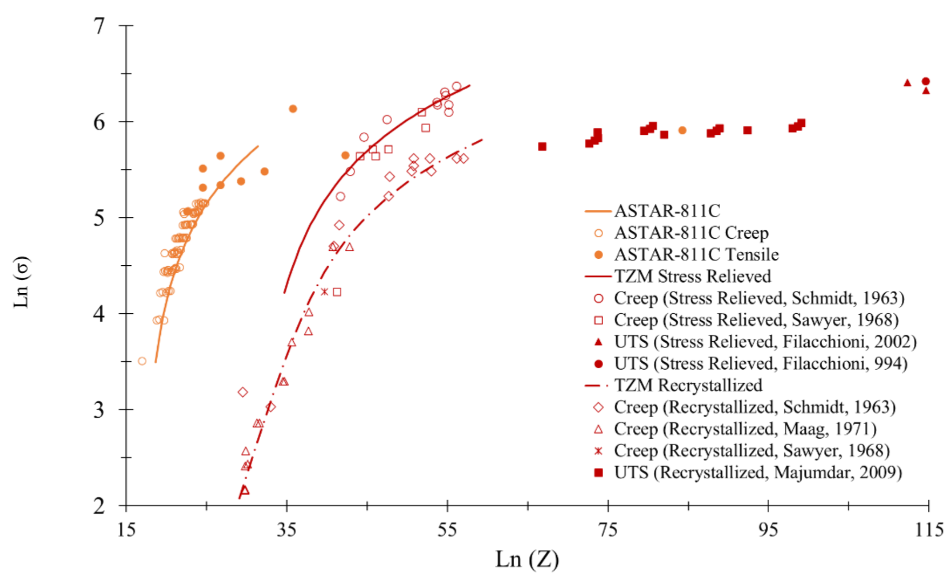

Figure D2. *TZM responses fall on distinct ST curves based on the samples' processing history, such as stress relief treatments or recrystallization. This phenomenon is not observed with the Nb-alloys or ASTAR-811C, rather the different processing techniques contribute to variability in the data.*

Appendix E: Elemental Thermophysical Properties

Table E1. *Melting Points of Refractory Metals that are Commonly Employed as Alloying Additions in Nb*

Alloy	T_m (˚C) in Literature
Ti	1660 [111]
Zr	1850 [111]
Hf	2230 [111]
Nb	2470 [111]
Ta	3000 [111]
W	3410 [111]

Table E2. *Properties Used in RoM Calculations*

Element	E (GPa) at RT	ρ (g/cm^3) at RT
Nb	103 [178]	8.57 [111]
Ta	185 [178]	16.7 [111]
W	400 [178]	19.3 [111]
Hf	137 [179]	13.3 [111]
Zr	99.3 [180]	6.5 [111]
Ti	120 [181]	4.5 [111]

Table E3. *Young's Modulus Temperature Dependence Data from Frost and Ashby, and GRANTA**

Element	T_m (K)	E_0 (GPa)	G_0 (GPa)	$\frac{T_m}{G_0}\frac{dG}{dT}$ or $\frac{T_m}{E_0}\frac{dE}{dT}$ (MPa/K)	$\frac{d}{dT}$ Range (MPa/K)
Nb	2741	103	44.3	-0.44	(-7.11) – (-19.6)
Ta	3271	185	61.2	-0.42	(-7.86) – (-21.2)
W	3683	400	160	-0.38	(-16.5) – (-42.4)

* Frost and Ashby ([46]) reports $\frac{T_m}{G_0}\frac{dG}{dT}$ and GRANTA ([111]) reports $\frac{T_m}{E_0}\frac{dE}{dT}$; all other data are consistent

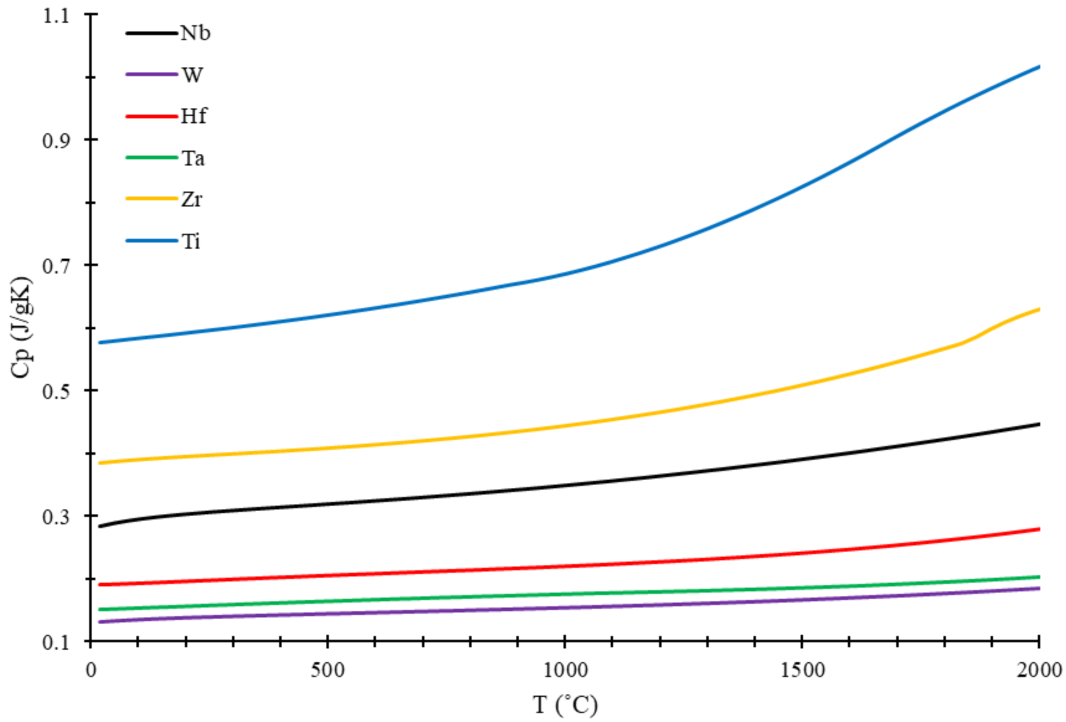

Figure E1. *Thermo-Calc determined specific heat capacities of common alloying elements in Nb.*

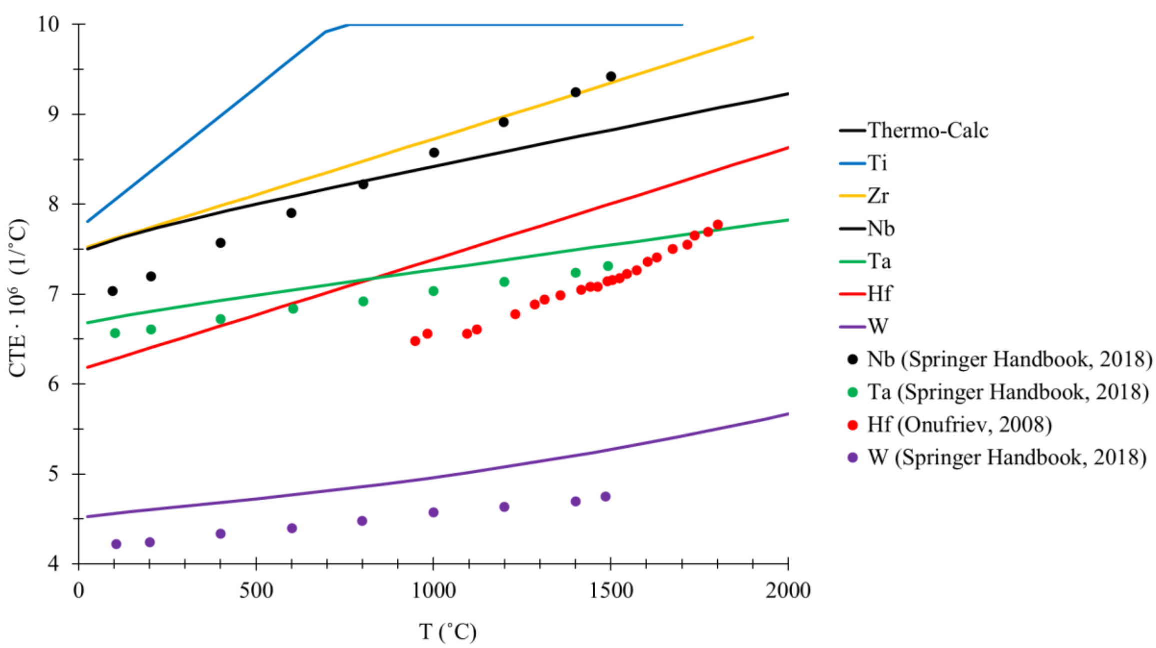

Figure E2. *Experimental and Thermo-Calc predicted CTE data common alloying elements in Nb.*

Appendix F: Density Calculations

Densities at room temperature (Table F1) and at elevated temperatures for these alloys calculated using experimental thermal expansion (CTE) data are presented in (Figure F1) via Equation F1; where ρ_0 is room temperature (T_0=25˚C) density and T is temperature in ˚C. Room temperature density measurements of a cast WC-3009 sample were conducted in accordance to the Archimedes method, ASTM B962-17 [156], resulting in a density of 10.25 g/cm^3, as discussed in Chapter 4.1.4. Densities were also gathered from Thermo-Calc's property model calculation mode for comparisons. The freeze-in temperature for each alloy was determined via rounding the alloy's solidus temperature down to the nearest hundred to ensure no liquid was within the alloy.

Table F1. *Room Temperature Density Values*

Alloy	**ρ_0 (g/cm^3)**
C103	8.85 [16]
WC-3009	10.25
C-129(Y)	9.49 [28]
Cb-752	9.02 [29]
D-43	9.09 (Thermo-Calc)
FS-85	10.60 [16]
MAR-M247	8.54 [182]
Haynes 230	8.97 [32]
ASTAR-811C	16.84 (Thermo-Calc)
TZM	10.23 (Thermo-Calc)

$$\rho(T) = \rho_0 \cdot \left[1 - \left(3 \cdot CTE \cdot (T - T_0)\right)\right] \qquad \text{Equation F1}$$

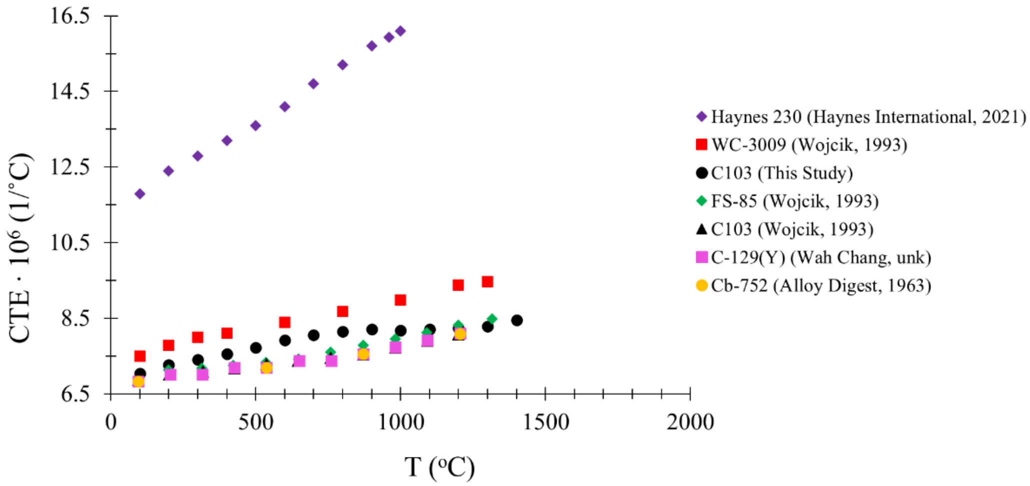

Figure F1. *Experimental CTE values used for calculating elevated temperature density*.

CTE data for polycrystalline MAR-M247 was not found in literature but was found in [177] for its single-crystal form CMSX-4 via Equation F2; the constants *a*, *b*, *c*, and *d*, were provided and *T* is temperature in ˚C. To determine CTE, the derivative of Equation F2 was taken with respect to temperature, as the coefficient of thermal expansion is the constant that relates strain to changes in temperature, which resulted in Equation F3. Equation F3 was used to model the coefficient of thermal expansion for MAR-M247 and therefore calculate its density via Equation F1.

$$\varepsilon(T) = a + bT + \left(c \cdot e^{dT}\right) \qquad \text{Equation F2}$$

$$CTE = b + \left(c \cdot d \cdot e^{dT}\right) \qquad \text{Equation F3}$$

Temperature dependent densities calculated from experimental data align well with those predicted via Thermo-Calc (Figure F2); therefore, its values for ASTAR-811C and TZM were used, as limited CTE data for these alloys exist in the literature (Figure F3).

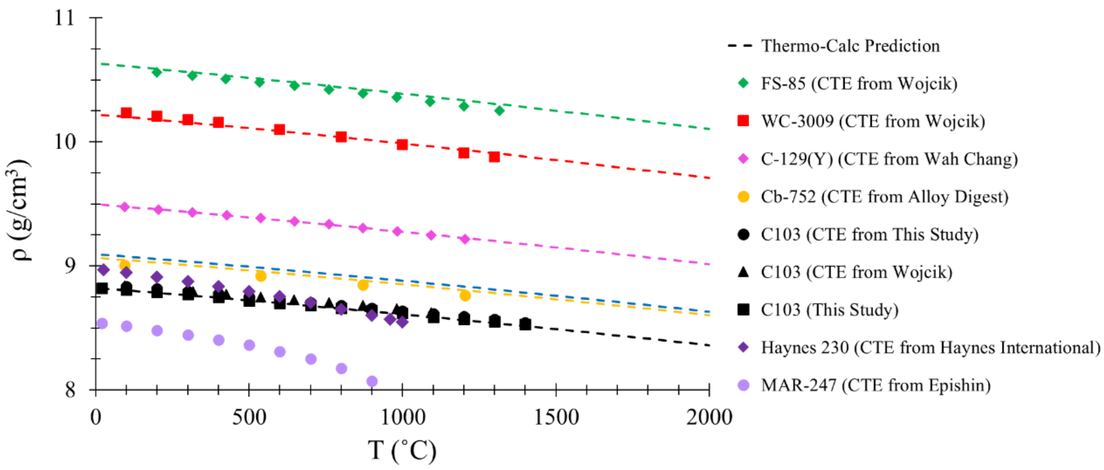

Figure F2. *Experimental data and Thermo-Calc model predictions of the temperature dependent density of six representative Nb-alloys, Haynes 230, and MAR-M247.*

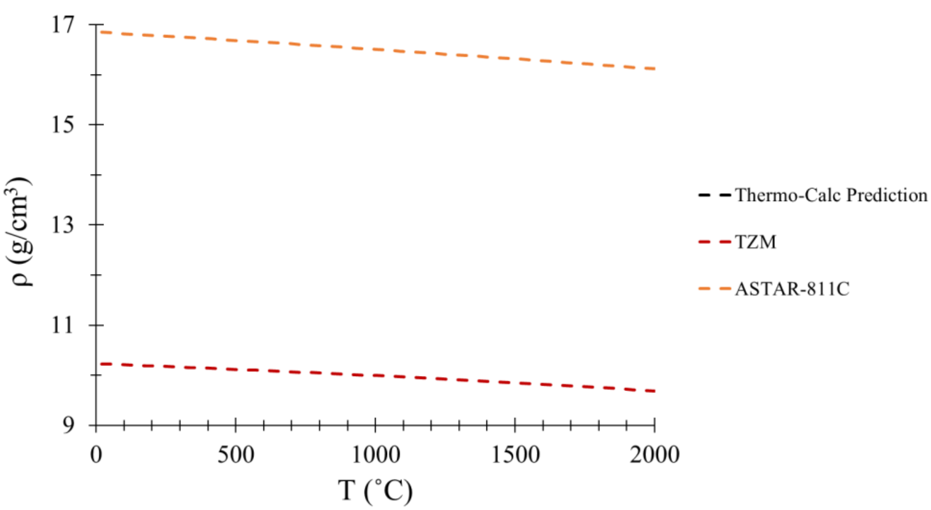

Figure F3. *Thermo-Calc model of the temperature dependent density of ASTAR-811C and TZM.*

Appendix G: Comparison of WC-3009 and D-43's Temperature and Strain Rate Sensitivities

Comparison curves between WC-3009 and D-43 were generated via their respective ST models. The strain rate sensitivity of WC-3009, and all other $n \approx 3$ alloys, is apparent in Figure G1, where the difference in strength of WC-3009 between two strain rates is significantly larger; a difference of 17× is observed for WC-3009 at 1400˚C between rates 10^{-7} and 10^{-3} s^{-1}, whereas D-43 experiences only a 5× at these conditions.

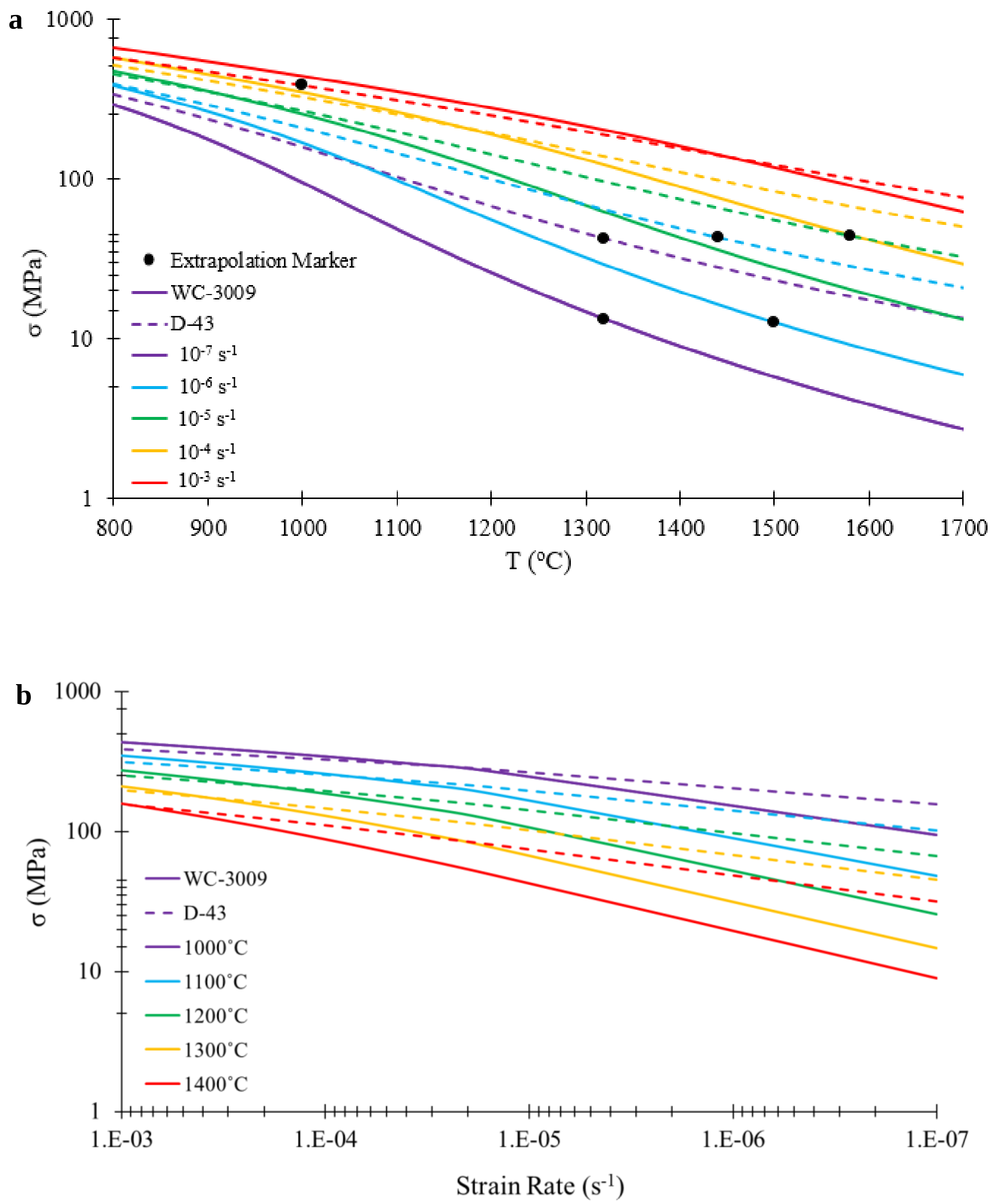

Figure G1. *Sellars-Tegart modeling of WC-3009 and D-43 flow stresses as a function of (a) temperature at constant strain rates and (b) strain rate at constant temperatures, demonstrating WC-3009's significant strain rate sensitivity. Extrapolations were determined via the bounds of experimental Zener-Holloman values; all data at either (a) higher temperatures or (b) lower rates than the marker are extrapolated; note there are no extrapolation in (b).*

Appendix H: Minimum Flow Stress Model Results for Ni-, Mo-, and Ta-based Alloys

At both strain rate regimes, MAR-M247 is stronger than the Nb-alloys at the lower temperatures (Figure H1), but this class of alloy is generally limited to applications with service temperatures below 1100˚C due to precipitate coarsening and incipient melting [7]. The inclusion of another Ni-superalloy, Haynes 230, demonstrates that nickel alloys are not universally stronger, even at lower temperatures (Figure H1). At temperatures of 1200˚C and higher, only the refractory alloys retain their strength. The Ta-based alloy, ASTAR-811C exhibits superior strength to the Nb-alloys at all but the highest temperatures and lowest strain rates, but subsequent analyses will show this alloy is not competitive for aerospace applications due to its relatively high density (16.8 g/cm^3 via Thermo-Calc), not to mention its high cost. Similarly, the Mo-alloy TZM demonstrates superior strength across both strain rates and processing histories considered (Figure H1). Based on this analysis alone, TZM is a top candidate for high-temperature structural applications, but what Mo-alloys have in strength, they lack in fabricability and oxidation resistance. When welded, Mo-alloys suffer from large grain size differences within the heat affected zone and, when recrystallized, demonstrate oxygen embrittlement (though carbon additions can alleviate these concerns to some degree) [12], [13] and a significant strength drop at tensile strain rates. These liabilities of alternatives suggest further consideration of Nb-based alloys, despite their lack of extreme strength.

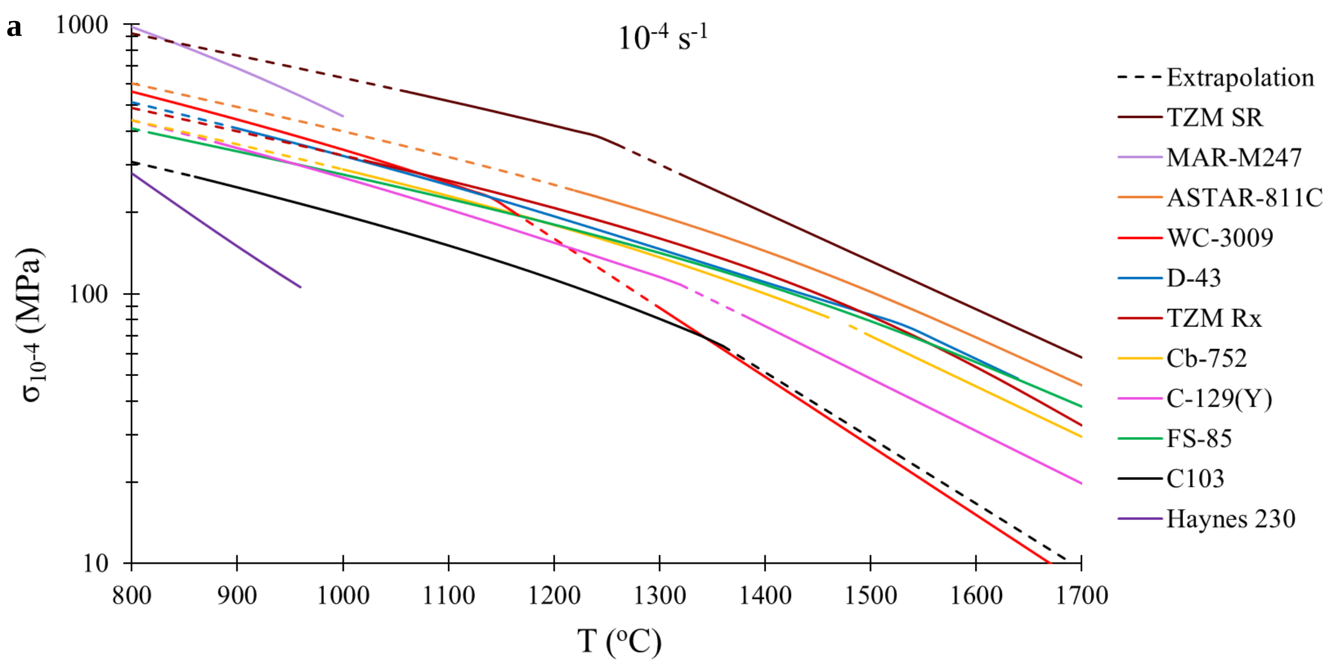

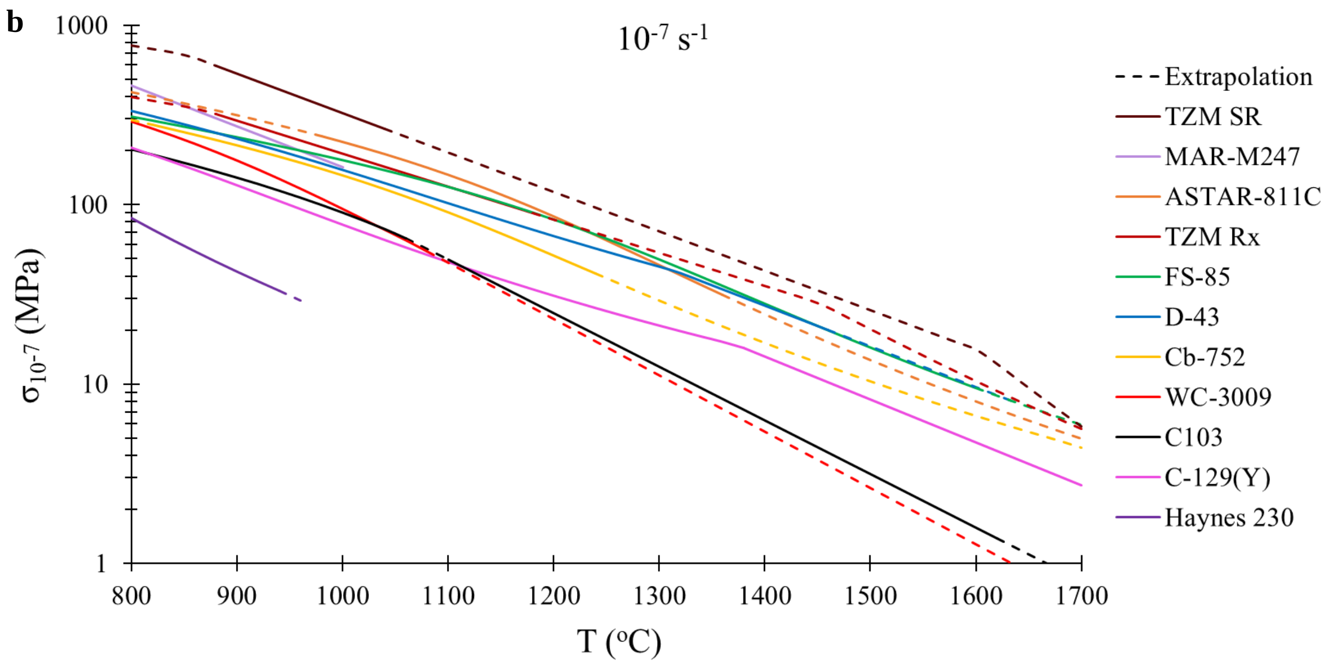

Figure H1. *Difficulties associated with processing TZM and high cost of ASTAR-811C restrict their applicability to aerospace applications, regardless of their high strength at elevated temperatures at (a) tensile rates and (b) creep rates. Extrapolations were determined via the bounds of experimental Zener-Holloman values and LMP*s.*

The high strength Ta-based alloy, ASTAR-811C, drops to one of the lowest preforming alloys when density factors are considered (Figure H2). For similar reasons, MAR-M247 remains superior at temperatures below its temperature barrier across both rates investigated, due to its slightly lower density than the Nb-alloys (Figure H2).

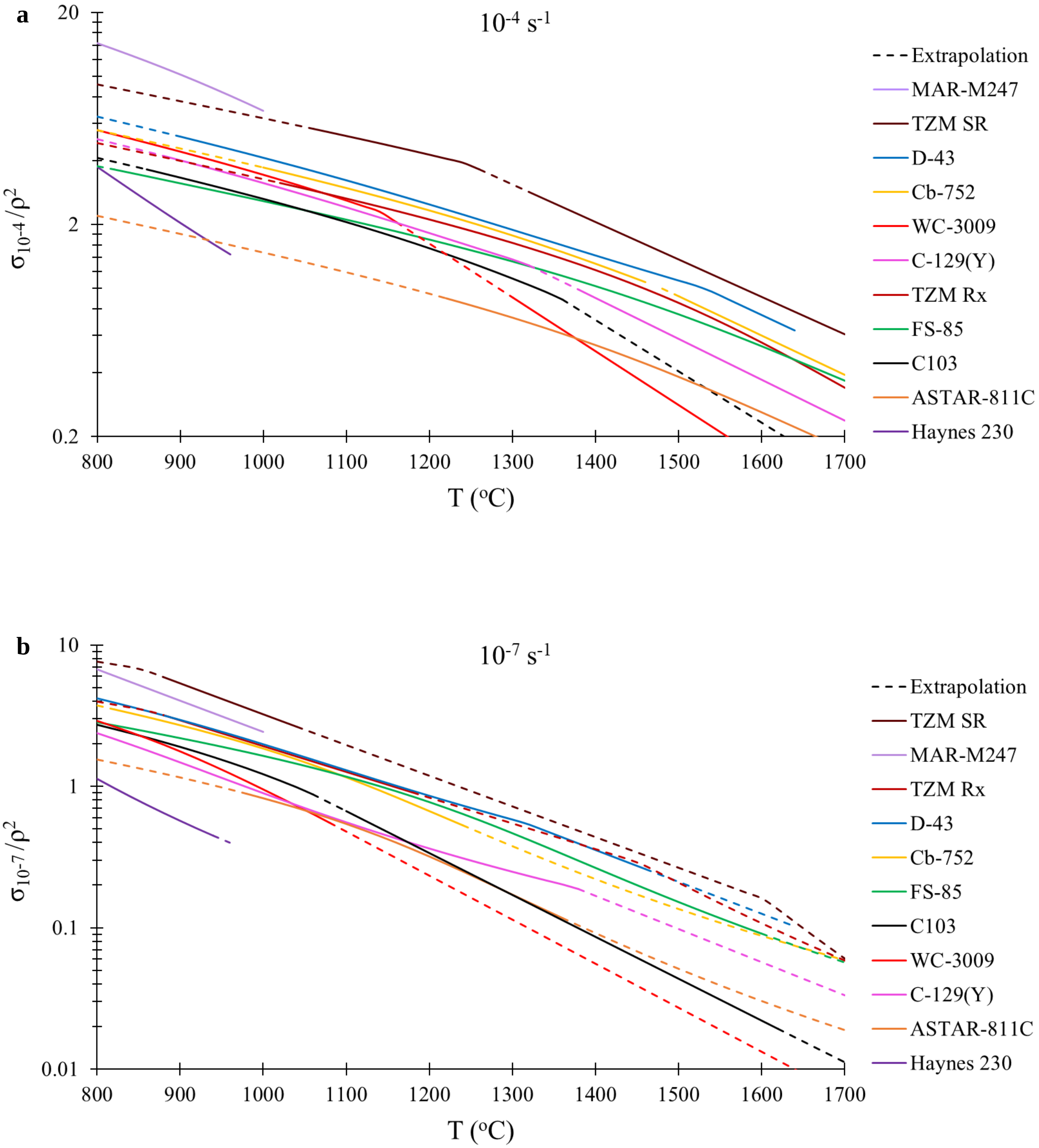

Figure H2. *Specific strength indices relevant to the design of lightweight panels reveal that the rank of ASTAR-811C falls in rank relative to the Nb-alloys at (a) tensile test and (b) creep-type rates. Extrapolations were determined via the bounds of experimental Zener-Holloman values and LMP*s.*

Appendix I: Supplemental TDTR Methods and Analysis

A Ti:Sapphire laser outputting 808 nm, 200 femtosecond pulses at an 80 MHz repetition rate was used to investigate thermal conductivity of WC-3009. Laser pulses were divided by a polarizing beam splitter to separate the pump and probe path. The pump-path passes through an electro-optic modulator (EOM) that sinusoidally modulates the pump beam at 8.4MHz, which allows lock-in detection of the pump-induced changes in temperature. 8.4MHz is important for an adequate signal-to-noise ratio; it has been validated to work for materials with relatively small phonon mean free paths and materials with electron dominated heat transport [183]. The modulated frequency is fed to a lock-in amplifier to isolate the pump-induced reflectance signal. The pump is then directed to the sample to generate a temperature change in the material. The probe path passes through a mechanical delay stage to temporally offset the probe signal from the pump and monitors the change in reflectance caused by the temperature rise in the material. To accurately measure the change in temperature by monitoring the change in reflection, the thermoreflectance coefficient (dR/dT) of the material must be known. In many materials of interest for TDTR application, this quantity is not known. To circumvent this, an 80 nm film of aluminum with a well-characterized dR/dT was deposited on the sample to accurately correlate the temperature gradient with reflectance changes [184]. Additionally, the aluminum layer ensures pump absorption at the surface, which is vital to accurately model heat diffusion. Thermal conductivity and thickness of the transducer was determined with 4-point probe and picosecond acoustics respectively [185]. The cylindrical heat equation was fit to the decay to extract thermal conductivity and thermal boundary conductance [136]. Information about the phase offset and magnitude of the pump-induced heating is captured by the lock-in amplifier in a real (in-phase) and imaginary (out-of-phase) signal. Fitting for the ratio of in-phase and out-of-phase signal provides a more reliable quantity than fitting for the in-phase signal exclusively (Figure I1) [186], [187].

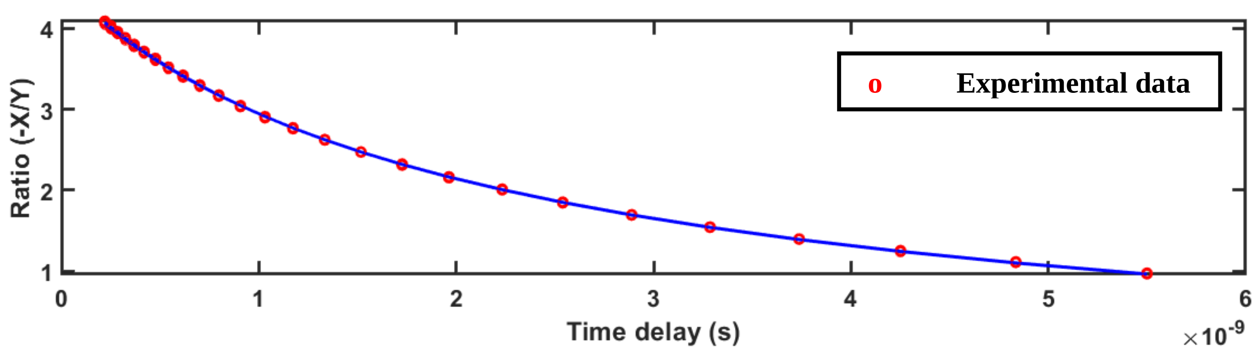

Figure I1. *Fit of the ratio of in-phase/out-of-phase signal from the cylindrical heat equation to experimental data.*

By taking the derivative of the ratio X/Y with respect to each parameter, a plot of sensitivities can be generated [188]. Parameters with deviations further from zero are more susceptible to system perturbations and are emphasized in uncertainty propagation. From the transient sensitivity, transducer thickness and heat capacity are relevant at earlier times. Thermal boundary conductance is relevant after the system equilibrates, and the thermal conductivity and heat capacity of the sample follows a similar time decaying trend to the transducer parameters. From the frequency dependent sensitivity, modulating at 8.4 MHz, transducer thickness and heat capacity as well as sample heat capacity and thermal conductivity are the most sensitive parameters with a weak dependence on thermal boundary conductance. All parameters must be known or fitted for before extracting sample thermal conductivity.

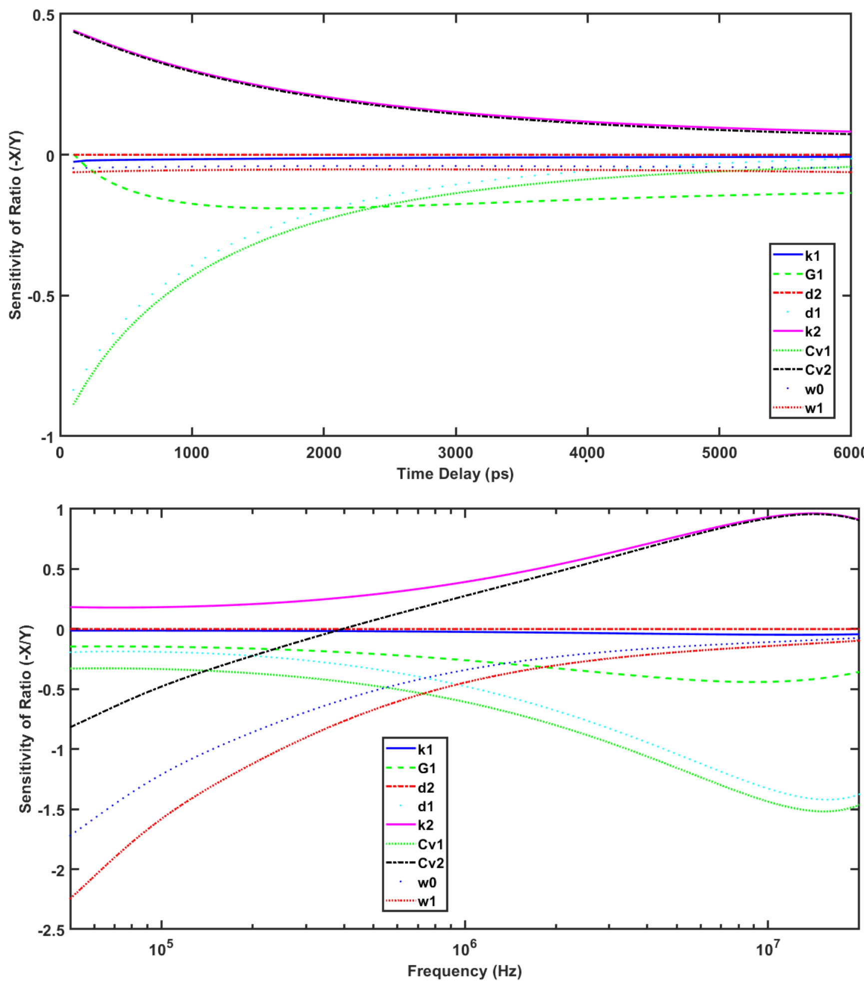

Figure I2. *Listed parameters in order are transducer thermal conductivity, thermal boundary conductance, thickness sample thickness, transducer thickness, sample thermal conductivity, transducer heat capacity, sample heat capacity, pump spot size, and probe spot size. Most sensitive parameters deviate further from zero.*

References

[1] J. Wadsworth, T. G. Nieh, and J. J. Stephens, "Recent advances in aerospace refractory metal alloys," *International materials reviews*, vol. 33, no. 1, pp. 131–150, 1988.

[2] D. L. Anton, D. B. Snow, and A. F. Giamei, "Dispersion Strengthening of High Temperature Niobium Alloys," *Advanced Materials and Processing Techniques for Structural Applications; Paris; France; 7-9 Sept. 1987*, pp. 119–128, 1987.

[3] S. C. Gülen, "Constant volume combustion: the ultimate gas turbine cycle," *Gas Turbine World*, vol. 43, no. 6, pp. 20–27, 2013.

[4] ARPA-E, "Ultrahigh Temperature Impervious Materials Advancing Turbine Efficiency."

[5] W. Xiong, A. X. Y. Guo, S. Zhan, C.-T. Liu, and S. C. Cao, "Refractory high-entropy alloys: A focused review of preparation methods and properties," *J Mater Sci Technol*, vol. 142, pp. 196–215, 2023.

[6] M. Sankar, V. V Satya Prasad, R. G. Baligidad, and A. A. Gokhale, "Melting, Processing and Characterization of Nb-10W-2.5 Zr (Cb-752) Alloy," *Transactions of the Indian Institute of Metals*, vol. 70, pp. 1055–1062, 2017.

[7] J. B. Wahl and K. Harris 3rd, "Improved 3rd Generation Single Crystal Superalloy CMSX-4® Plus (SLS)—A Study of Evolutionary Alloy Development," *Cannon-Muskegon: Muskegon, MI, USA*, 1984.

[8] B. L. Koff, "Gas turbine technology evolution: A designers perspective," *J Propuls Power*, vol. 20, no. 4, pp. 577–595, 2004.

[9] J. H. Perepezko, "The hotter the engine, the better," *Science (1979)*, vol. 326, no. 5956, pp. 1068–1069, 2009.

[10] L. J. Pionke and J. W. Davis, "Technical assessment of niobium alloys data base for fusion reactor applications," McDonnell Douglas Astronautics Co., St. Louis, MO (USA), 1979.

[11] N. R. Philips, M. Carl, and N. J. Cunningham, "New Opportunities in Refractory Alloys," *Metallurgical and Materials Transactions A*, vol. 51, no. 7, pp. 3299–3310, 2020, doi: 10.1007/s11661-020-05803-3.

[12] J. Wadsworth, G. R. Morse, and P. M. Chewey, “The microstructure and mechanical properties of a welded molybdenum alloy,” *Materials Science and Engineering*, vol. 59, no. 2, pp. 257–273, 1983.

[13] A. Kumar and B. L. Eyre, “Grain boundary segregation and intergranular fracture in molybdenum,” *Proceedings of the Royal Society of London. A. Mathematical and Physical Sciences*, vol. 370, no. 1743, pp. 431–458, 1980.

[14] L. L. Snead, D. T. Hoelzer, M. Rieth, and A. A. N. Nemith, “Refractory Alloys: Vanadium, niobium, molybdenum, tungsten,” in *Structural alloys for nuclear energy applications*, Elsevier, 2019, pp. 585–640.

[15] C. E. Duty, S. J. Zinkle, R. F. Luther, R. W. Buckman, R. E. Gold, and Y. A. Ballout, “The Potential of Tantalum Alloys for Space Nuclear Applications,” in *proceedings of American Nuclear Society Annual Meeting Embedded Topical: Space Nuclear Power*, 2005, pp. 294–302.

[16] C. C. Wojcik, “Processing, properties and applications of high-temperature niobium alloys,” *MRS Online Proceedings Library (OPL)*, vol. 322, 1993.

[17] O. N. Senkov, S. I. Rao, D. B. Miracle, A. E. Mann, and A. Yousefiani, “Effect of Re and Al additions on the microstructure and mechanical properties of Nb-18Ti-12W alloy,” *Materials Science and Engineering: A*, vol. 870, p. 144870, 2023.

[18] O. N. Senkov, S. I. Rao, T. M. Butler, and K. J. Chaput, “Ductile Nb alloys with reduced density and cost,” *J Alloys Compd*, vol. 808, p. 151685, 2019.

[19] O. N. Senkov, S. I. Rao, T. M. Butler, T. I. Daboiku, and K. J. Chaput, “Microstructure and properties of Nb-Mo-Zr based refractory alloys,” *Int J Refract Metals Hard Mater*, vol. 92, p. 105321, 2020.

[20] X.-Y. Ding, H.-Y. Zheng, P.-P. Zhang, L.-M. Luo, Y.-C. Wu, and J.-H. Yao, “Microstructure and Mechanical Properties of WTaVCrTi Refractory High-Entropy Alloy by Vacuum Levitation Melting for Fusion Applications,” *J Mater Eng Perform*, vol. 32, no. 17, pp. 7869–7878, 2023.

[21] J. Startt, A. Kustas, J. Pegues, P. Yang, and R. Dingreville, “Compositional effects on the mechanical and thermal properties of MoNbTaTi refractory complex concentrated alloys,” *Mater Des*, vol. 213, p. 110311, 2022.

[22] M. Yang, L. Shao, J.-M. Duan, X.-T. Chen, and B.-Y. Tang, "Temperature dependence of mechanical and thermodynamic properties of Ti (25+ x) Zr25Nb25Ta (25-x)(x≤ 20) refractory high entropy alloys: Influences of substitution of Ti for Ta," *Physica B Condens Matter*, vol. 606, p. 412851, 2021.

[23] H. Song, F. Tian, and D. Wang, "Thermodynamic properties of refractory high entropy alloys," *J Alloys Compd*, vol. 682, pp. 773–777, 2016.

[24] L. Hu, M. J. Lin, and B. Wei, "Hypercooling limit and physical properties of liquid MoNbReTaW refractory high-entropy alloy," *Philos Mag Lett*, vol. 101, no. 8, pp. 312–319, 2021.

[25] H. W. Yao, J. W. Qiao, J. A. Hawk, H. F. Zhou, M. W. Chen, and M. C. Gao, "Mechanical properties of refractory high-entropy alloys: Experiments and modeling," *J Alloys Compd*, vol. 696, pp. 1139–1150, 2017.

[26] P. Hidnert and W. H. Souder, *Thermal expansion of solids*, vol. 486. US Government Printing Office, 1950.

[27] L. Backman, J. Gild, J. Luo, and E. J. Opila, "Part I: Theoretical predictions of preferential oxidation in refractory high entropy materials," *Acta Mater*, vol. 197, pp. 20–27, 2020.

[28] Wah Chang Albany, "WC-129Y welded, spun, and deep drawn assembly for space application."

[29] "Haynes Alloy No. Cb-752: High Temperature Alloy," *Alloy Digest*, vol. 12, no. 11, 1963.

[30] "Columbium D-43: High Temperature Alloy," *Alloy Digest*, vol. 14, no. 6, p. Cb-9, Jun. 1965, doi: 10.31399/asm.ad.cb0009.

[31] A. J. Torroba *et al.*, "Investment casting of nozzle guide vanes from nickel-based superalloys: part I – thermal calibration and porosity prediction," *Integr Mater Manuf Innov*, vol. 3, no. 1, pp. 344–368, 2014, doi: 10.1186/s40192-014-0025-5.

[32] Haynes International, "Haynes® 230® alloy," 2021.

[33] R. R. Hickman, J. J. Martin, G. R. Schmidt, T. J. Godfroy, and A. J. Bryhan, "Cost Estimate for Molybdenum and Tantalum Refractory Metal Alloy Flow Circuit Concepts," 2010.

[34] American Elements, "TZM Molybdenum Alloy."

[35] D. L. Harrod and R. W. Buckman Jr, "Effect of Heat Treatment on Creep Properties of the Tantalum Base Alloy ASTAR-811C.," Westinghouse Electric Corp., Pittsburgh, Pa. Astronuclear Lab., 1970.

[36] F. F. Schmidt and H. R. Ogden, *The engineering properties of molybdenum and molybdenum alloys*, vol. 190. Defense Metals Information Center, Battelle Memorial Institute, 1963.

[37] C Craig Wojcik, "Thermomechanical processing and properties of niobium alloys," in *International Symposium Niobium*, 2001.

[38] C. L. Briant, "Tungsten: properties, processing, and applications," *Advanced materials & processes*, vol. 154, no. 5, p. 29, 1998.

[39] J. Davis, Ed., *Metals Handbook*, 2nd ed. ASM International, 1998.

[40] D. B. Miracle, O. N. Senkov, C. Frey, S. Rao, and T. M. Pollock, "Strength vs Temperature for Refractory Complex Concentrated Alloys (RCCAs): A critical comparison with refractory BCC elements and dilute alloys," *Acta Mater*, p. 119692, 2024.

[41] G. A. Meerson and T. Segorcheanu, "The affinity of niobium for oxygen," *Soviet Atomic Energy*, vol. 13, no. 6, pp. 1230–1233, 1963, doi: 10.1007/BF01312333.

[42] B. Vishwanadh, N. N. Kumar, G. Samyuktha, V. Kaushik, and R. Tewari, "Development of a new thermo-mechanical processing route for Nb-5Mo-1Zr-0.1 C (wt%) alloy," *J Alloys Compd*, vol. 942, p. 168860, 2023.

[43] J.M. Skelton, "In Preparation," *In Preparation*, 2024.

[44] M. E. Kassner, *Fundamentals of creep in metals and alloys*. Butterworth-Heinemann, 2015.

[45] R. W. Hertzberg, R. P. Vinci, and J. L. Hertzberg, *Deformation and fracture mechanics of engineering materials*. John Wiley & Sons, 2020.

[46] H. J. Frost and M. F. Ashby, "Deformation-mechanism maps: The plasticity and creep of metals and ceramics(Book)," *Oxford, Pergamon Press, 1982, 175 p*, 1982.

[47] H. R. Schober, W. Petry, and J. Trampenau, "Migration enthalpies in FCC and BCC metals," *Journal of Physics: Condensed Matter*, vol. 4, no. 47, p. 9321, 1992.

[48] P. S. Follansbee, “Fundamentals of strength,” *Wiley, New Jersey*, vol. 10, p. 9781118808412, 2014.

[49] F. Abe, T.-U. Kern, and R. Viswanathan, *Creep-resistant steels*. Elsevier, 2008.

[50] W. Chen and M. C. Chaturvedi, “The effect of grain boundary precipitates on the creep behavior of Inconel 718,” *Materials Science and Engineering: A*, vol. 183, no. 1–2, pp. 81–89, 1994.

[51] H. F. Jackson and W. E. Lee, “Properties and characteristics of ZrC,” *Comprehensive nuclear materials*, vol. 2, pp. 339–372, 2012.

[52] W. D. Callister *et al.*, *Materials science and engineering: an introduction*, vol. 7. John wiley & sons New York, 2007.

[53] Y. Lin *et al.*, “First-Principles Calculations of Thermal and Electrical Transport Properties of bcc and fcc Dilute Fe–X (X= Al, Co, Cr, Mn, Mo, Nb, Ni, Ti, V, and W) Binary Alloys,” *Metals (Basel)*, vol. 11, no. 12, p. 1988, 2021.

[54] H. Yang *et al.*, “High strength and high conductivity Cu alloys: A review,” *Sci China Technol Sci*, vol. 63, no. 12, pp. 2505–2517, 2020.

[55] E. I. Andritsos *et al.*, “The heat capacity of matter beyond the Dulong–Petit value,” *Journal of Physics: Condensed Matter*, vol. 25, no. 23, p. 235401, 2013.

[56] N. Lopanitsyna, C. Ben Mahmoud, and M. Ceriotti, “Finite-temperature materials modeling from the quantum nuclei to the hot electron regime,” *Phys Rev Mater*, vol. 5, no. 4, p. 043802, 2021.

[57] F. R. Larson and J. Miller, “A time-temperature relationship for rupture and creep stresses,” *Transactions of the American Society of Mechanical Engineers*, vol. 74, no. 5, pp. 765–771, 1952.

[58] Hollomon J. H. and Jaffe L. D., “Time-temperature Relations in Tempering Steel,” *American Institute of Mining and Metallurgical Engineers -- Technical Publications*, vol. 162, pp. 223–249, 1945.

[59] F. T. Furillo, S. Purushothaman, and J. K. Tien, “Understanding the larson-miller parameter,” *Scripta Metallurgica*, vol. 11, 1977.

[60] J. A. Horak and L. K. Egner, “Creep properties of Nb-1Zr and Nb-1Zr-0.1 C,” Oak Ridge National Lab., 1994.

[61] K. Leonard, J. Busby, D. Hoelzer, and S. J. Zinkle, “Nb-Base FS-85 Alloy as a Candidate Structural Material for Space Reactor Applications: Effects of Thermal Aging,” *Metallurgical and Materials Transactions A-physical Metallurgy and Materials Science - Metall Mater Trans A*, vol. 40, pp. 838–855, Apr. 2009, doi: 10.1007/s11661-008-9771-3.

[62] M. G. Hebsur and R. H. Titran, “Tensile and creep rupture behavior of P/M processed Nb-base alloy, WC-3009,” in *TMS-AIME Fall Meeting*, 1988.

[63] K. D. Sheffler, J. C. Sawyer, and E. A. Steigerwald, “Creep Behavior of Refractory Alloys in Ultrahigh Vacuum.,” TRW Equipment Labs., Cleveland, Ohio, 1970.

[64] R. L. Stephenson, “Application of the Larson-Miller parameter to niobium-base alloys,” in *Space Shuttle Materials. Vol. 3*, 1971.

[65] R. K. Penny and D. L. Marriott, *Design for creep*. Springer Science & Business Media, 2012.

[66] F. Garofalo, “An Empirical Relation Defining the Stress Dependence to Minimum Creep Rate in Metals,” *Trans. Metall. Soc. AIME*, vol. 227, p. 351, 1963.

[67] F. Garofalo, “Discussion of An Empirical Relation Defining the Stress Dependence to Minimum Creep Rate in Metals,” *Trans. Metall. Soc. AIME*, vol. 227, p. 351, 1963.

[68] C. M. Sellars and W. J. Tegart, “La relation entre la résistance et la structure dans la deformation à chaud,” *Mémoires scientifiques de la revue de métallurgie*, vol. 63, pp. 731–746, 1966.

[69] J. Wadsworth, S. E. Dougherty, T. G. Nieh, and P. A. Kramer, “Evidence for dislocation glide controlled creep in niobium-base alloys,” *Scripta Metallurgica et Materialia*, vol. 27, no. 1, pp. 71–76, 1992, [Online]. Available: http://inis.iaea.org/search/search.aspx?orig_q=RN:24014172

[70] Developed by Subcommittee: E28.04, “ASTM E8/E8M-22 Standard Test Methods for Tension Testing of Metallic Materials,” in *Book of Standards*, 1st ed., vol. 3, 2021.

[71] Developed by Subcommittee: E28.04, “ASTM E21-20 Standard Test Methods for Elevated Temperature Tension Tests of Metallic Materials,” in *Book of Standards*, 1st ed., vol. 3, ASTM, 2021.

[72] W. Hu, J. Xie, H. W. Chau, and B. C. Si, "Evaluation of parameter uncertainties in nonlinear regression using Microsoft Excel Spreadsheet," *Environmental Systems Research*, vol. 4, pp. 1–12, 2015.

[73] J. Wadsworth, C. A. Roberts, and E. H. Rennhack, "Creep behaviour of hot isostatically pressed niobium alloy powder compacts," *J Mater Sci*, vol. 17, pp. 2539–2546, 1982.

[74] N. L. Peterson, "Diffusion in refractory metals," Advanced Metals Research Corp Somerville MA, 1960.

[75] R. L. Stephenson, "The creep-rupture properties of some refractory metal alloys II. The properties of the niobium-base alloys FS-85 and Cb-752 and their response to heat treatment," *Journal of the Less Common Metals*, vol. 15, no. 4, pp. 403–414, 1968, doi: https://doi.org/10.1016/0022-5088(68)90106-9.

[76] R. L. Stephenson, "Comparative creep-rupture properties of D-43 and B-66 alloys," Oak Ridge National Lab., Tenn., 1964.

[77] D. L. Harrod and R. W. Buckman Jr, "Effect of Heat Treatment on Creep Properties of the Tantalum Base Alloy ASTAR-811C.," Westinghouse Electric Corp., Pittsburgh, Pa. Astronuclear Lab., 1970.

[78] W. L. Maag and W. F. Mattson, *Experimental biaxial creep data for tantalum, molybdenum, and alloys T-111, TZM, and TZC*, vol. 6149. National Aeronautics and Space Administration, 1971.

[79] W. L. Maag and W. F. Mattson, *Statistical Analysis of High-temperature Creep-rate Data for Alloys of Tantalum, Molybdenum, and Columbium*, vol. 5424. National Aeronautics and Space Administration, 1969.

[80] G. J. Pataky, H. Sehitoglu, and H. J. Maier, "Creep deformation and mechanisms in Haynes 230 at 800 C and 900 C," *Journal of nuclear materials*, vol. 443, no. 1–3, pp. 484–490, 2013.

[81] J.-H. Liao, H.-Y. Bor, C.-G. Chao, and T.-F. Liu, "Influence of Rhenium on the Grain Boundary Strength, Phase Evolution, and High Temperature Mechanical Properties of a Fine-Grain Nickel-Base Superalloy at 982 C," *Mater Trans*, vol. 52, no. 10, pp. 1989–1997, 2011.

[82] K. J. Leonard, C. E. Duty, S. J. Zinkle, R. F. Luther, R. E. Gold, and R. W. Buckman, “Niobium-base alloys for space nuclear applications,” in *Proc. Space Nuclear Conf., American Nuclear Society, San Diego, CA*, 2005, pp. 286–293.

[83] C. Wojcik, “Evaluation of powder metallurgy processed Nb-30Hf-9W (WC-3009),” in *Modern developments in powder metallurgy; Proceedings of the International Powder Metallurgy Conference, Orlando, FL; United States; 5-10 June 1988*, 1988, pp. 187–200.

[84] M. Kvapilova, J. Dvorak, P. Kral, K. Hrbacek, and V. Sklenicka, “Creep behaviour and life assessment of a cast nickel–base superalloy MAR–M247,” *High Temperature Materials and Processes*, vol. 38, no. 2019, pp. 590–600, 2019.

[85] L. W. Sink, G. S. Hoppin III, and M. Fujii, “Low-cost directionally-solidified turbine blades, volume 1,” 1979.

[86] D. Klarstrom, “Aerospace and High Performance Alloys Database”.

[87] R. H. Titran and W. D. Klopp, “Long-Time Creep Behavior of the Niobium Alloy C-103,” *National Aeronautics and Space Administration, pp. 11, 1980*, p. 11, 1980.

[88] R. H. Titran, R. W. Hall, and NASA LRC, “Ultrahigh-Vacuum Creep Behavior of Columbium and Tantalum Alloys at 2000 degs and 2200 degs F for Times Greater Than 1000 Hours,” 1966.

[89] R. L. Stephenson, “The creep-rupture properties of some refractory metal alloys I. Effect of heat treatment on the properties of the niobium-base alloy D-43,” *Journal of the Less Common Metals*, vol. 15, no. 4, pp. 395–402, 1968.

[90] K. D. Sheffler and R. R. Ebert, “Generation of long time creep data on refractory alloys at elevated temperatures,” 1973.

[91] R. E. Gold, “Investigation of high temperature fracture of T-111 and ASTAR-811C,” 1971.

[92] M. K. Kumawat *et al.*, “Tensile behavior of a slurry Fe-Cr-Si coated Nb-alloy evaluated by Gleeble testing,” *Surf Coat Technol*, vol. 349, pp. 695–706, 2018.

[93] S. S. Panwar, K. Prasad, T. U. Patro, K. Balasubramanian, and B. Venkataraman, “On the occurrence of dynamic strain aging in C-103 Nb based alloy,” *Materials Science and Engineering: A*, vol. 620, pp. 286–292, 2015.

[94] C. Himmelblau, M. Kibrick, J. Runkle, A. Joshi, J. Wadsworth, and J. Moncur, "Mechanical properties of HIP columbium C-103 Alloy," *Prog. Powder Metall.;(United States)*, vol. 39, no. CONF-8305226-, 1984.

[95] R. L. Stephenson, "Creep–Rupture Properties of C-129Y in Vacuum," *Journal of Vacuum Science and Technology*, vol. 7, no. 6, pp. S112–S115, 1970.

[96] E. S. Bartlett and J. A. VanEcho, *Creep of Columbium Alloys*, vol. 170. Battelle Memorial Institute, Defense Metals Information Center, 1963.

[97] R. G. Baggerly and R. T. Torgerson, "Evaluation Of Cb-752, Columbium Alloy (Cb-10 percent W-2.5 percent Zr)," Boeing Co., Seattle, 1963.

[98] G. E. Gazza and T. S. DeSisto, "Evaluation of Refractory Metal Sheet Alloys," in *Metallurgical Society Conferences*, Gordon and Breach, Science Publishers, 1966, p. 346.

[99] J. G. Bewley, "Strengthening of Columbium Alloy Cb-752 by Duplex-Annealing Process," *Gordon and Breach Sci. Publ*, pp. 369–386, 1968.

[100] F. F. Schmidt and H. R. Ogden, *The engineering properties of columbium and columbium alloys*, vol. 188. Defense Metals Information Center, Battelle Memorial Institute, 1963.

[101] G. G. Lessmann, "Determination of weldability and elevated temperature stability of refractory metal alloys. 1-Weldability of refractory metal alloys," NASA, 1970.

[102] J. W. Edington, "Improvement of Creep Strength and Low-temperature Ductility of Refractory Metals by Means of Mechanical Twinning Final Report," 1966.

[103] R. W. Buckman Jr and R. C. Goodspeed, "Precipitation strengthened tantalum base alloys," NASA, 1971.

[104] G. Filacchioni, E. Casagrande, U. De Angelis, G. De Santis, and D. Ferrara, "Effects of strain rate on tensile properties of TZM and Mo–5% Re," *Journal of nuclear materials*, vol. 307, pp. 705–709, 2002.

[105] S. Majumdar *et al.*, "A study of hot deformation behavior and microstructural characterization of Mo–TZM alloy," *Journal of nuclear materials*, vol. 385, no. 3, pp. 545–551, 2009.

[106] K. Hrutkay and D. Kaoumi, “Tensile deformation behavior of a nickel based superalloy at different temperatures,” *Materials Science and Engineering: A*, vol. 599, pp. 196–203, 2014.

[107] M. A. Ritzo, J. J. Bhattacharyya, R. A. Lebensohn, and S. R. Agnew, “An investigation into the role of dislocation climb during intermediate temperature flow of Mg alloys,” in *Magnesium Technology 2020*, Springer, 2020, pp. 115–122.

[108] P. Yavari, F. A. Mohamed, and T. G. Langdon, “Creep and substructure formation in an Al-5% Mg solid solution alloy,” *Acta Metallurgica*, vol. 29, no. 8, pp. 1495–1507, 1981.

[109] M. J. Davidson, M. Biberger, and A. K. Mukherjee, “Creep of niobium and solid solution strengthened Nb-1wt.% Zr,” *Scripta Metallurgica et Materialia;(United States)*, vol. 27, no. 12, 1992.

[110] J. Friedel, *Dislocations*. Pergamon, 1964.

[111] “Ansys GRANTA EduPack Software.” ANSYS, Inc., Cambridge, 2023.

[112] B. Verlinden, J. Driver, I. Samajdar, and R. D. Doherty, *Thermo-mechanical processing of metallic materials*. Elsevier, 2007.

[113] O. N. Senkov, S. Gorsse, and D. B. Miracle, “High temperature strength of refractory complex concentrated alloys,” *Acta Mater*, vol. 175, pp. 394–405, 2019.

[114] Y. H. Zhang and D. M. Knowles, “Prestraining effect on creep behaviour of nickel base C263 superalloy,” *Materials science and technology*, vol. 18, no. 8, pp. 917–923, 2002.

[115] S. Bahl, J. U. Rakhmonov, C. Kenel, D. C. Dunand, and A. Shyam, “Effect of grain-boundary θ-Al2Cu precipitates on tensile and compressive creep properties of cast Al–Cu–Mn–Zr alloys,” *Materials Science and Engineering: A*, vol. 840, p. 142946, 2022.

[116] F. Ostermann and F. Bollenrath, “ON THE PRECIPITATION BEHAVIOR OF NIOBIUM ALLOY D-43 (Nb--10W--1Zr--0.1 C).,” Air Force Materials Lab., Wright-Patterson AFB, Ohio. Technische Hochschule …, 1970.

[117] F. Ostermann and F. Bollenrath, *Investigation of precipitates in two carbon-containing columbium-base alloys*. Air Force Materials Laboratory, Research and Technology Division, Air Force …, 1966.

[118] T. K. Roche, “Aging of Columbium Alloy D-43,” United States, 1965.

[119] F. Ostermann, “Controlling carbide dispersions in niobium-base alloys,” *Journal of the Less Common Metals*, vol. 25, no. 3, pp. 243–256, 1971.

[120] P. G. Shewmon, *Diffusion in solids*, 2nd ed. Warrendale, Pa: Minerals, Metals & Materials Society, 1989.

[121] E. J. Delgrosso, C. E. Carlson, and J. J. Kaminsky, “Development of niobium-zirconium-carbon alloys,” *Journal of the less common metals*, vol. 12, no. 3, pp. 173–201, 1967.

[122] J.-H. Kang and P. E. J. Rivera-Díaz-del-Castillo, “Carbide dissolution in bearing steels,” *Comput Mater Sci*, vol. 67, pp. 364–372, 2013.

[123] Robert H.Titran and Robert W.Hall, “Ultrahigh-Vacuum Creep Behavior of Columbium and Tantalum Alloys at 2000 and 2200F for Times Greater than 1000 Hours,” 1966.

[124] M. Uz and R. H. Titran, “Effects of processing and prolonged high temperature exposure on the microstructure of Nb-1Zr-C sheet,” *MRS Online Proceedings Library (OPL)*, vol. 322, 1993.

[125] R. H. Titran and M. Uz, “Effects of thermomechanical processing on the microstructure and mechanical properties of Nb-1Zr-C alloys,” in *Specialist Conference on’’Nuclear Power Engineering in Space Materials Fuel’’*, 1996.

[126] D. M. Farkas and A. K. Mukherjee, “Creep behavior and microstructural correlation of a particle-strengthened Nb–1Zr–0.1 C alloy,” *J Mater Res*, vol. 11, no. 9, pp. 2198–2205, 1996.

[127] R. T. Begley and J. H. Bechtold, “Effect of alloying on the mechanical properties of Niobium,” *Journal of the Less Common Metals*, vol. 3, no. 1, pp. 1–12, 1961.

[128] M. E. Kassner and T. A. Hayes, “Creep cavitation in metals,” *Int J Plast*, vol. 19, no. 10, pp. 1715–1748, 2003.

[129] M. F. Ashby and D. Cebon, “Materials selection in mechanical design,” *MRS Bull*, vol. 30, no. 12, p. 995, 2005.

[130] J. Bewley, “Final Report on Development of Methods to Produce Columbium Alloy Cb-74 (Renumbered Haynes Alloy Cb-752) Sheet,” 1963.

[131] Developed by Subcommittee: B10.03, "ASTM B654 Standard Specification for Niobium-Hafnium Alloy Foil, Sheet, Strip, and Plate," in *Book of Standards*, 1st ed., vol. 2, 2018.

[132] B. Sundman, H. L. Lukas, and S. G. Fries, "Computational thermodynamics: the Calphad method." Cambridge university press Cambridge, 2007.

[133] "Thermo-Calc Software: Computational Materials Engineering," Thermo-Calc Software 2024 .

[134] D. J. Senor, J. K. Thomas, and K. L. Peddicord, "Transport property correlations for the niobium-1% zirconium alloy," *Journal of nuclear materials*, vol. 173, no. 3, pp. 274–283, 1990.

[135] J. C. Hedge, C. Kostenko, and J. I. Lang, "Thermal properties of refractory alloys," IIT RESEARCH INST CHICAGO IL, 1963.

[136] D. G. Cahill, "Analysis of heat flow in layered structures for time-domain thermoreflectance," *Review of scientific instruments*, vol. 75, no. 12, pp. 5119–5122, 2004.

[137] P. E. Hopkins, J. R. Serrano, L. M. Phinney, S. P. Kearney, T. W. Grasser, and C. T. Harris, "Criteria for cross-plane dominated thermal transport in multilayer thin film systems during modulated laser heating," *J Heat Transfer*, vol. 132, no. 8, 2010.

[138] T. W. Pfeifer *et al.*, "Measuring sub-surface spatially varying thermal conductivity of silicon implanted with krypton," *J Appl Phys*, vol. 132, no. 7, p. 075112, 2022.

[139] C. Y. Ho, R. W. Powell, and P. E. Liley, "Thermal conductivity of the elements," *J Phys Chem Ref Data*, vol. 1, no. 2, pp. 279–421, 1972.

[140] P. G. Klemens and R. K. Williams, "Thermal conductivity of metals and alloys," *International metals reviews*, vol. 31, no. 1, pp. 197–215, 1986.

[141] P. G. Klemens and R. K. Williams, "Thermal conductivity of metals and alloys," *International metals reviews*, vol. 31, no. 1, pp. 197–215, 1986.

[142] F.J. Blatt, "Matthiessen's rule," *AccessScience*, 2020.

[143] N. E. Prasad and R. J. H. Wanhill, *Aerospace materials and material technologies*, vol. 3. Springer, 2017.

[144] "Columbium and tantalum alloys for structural and nuclear applications," May 1962.

[145] Anon, "Columbium, Tantalum and Tungsten Alloys Technical Information. vol. 3 (Wah Chang, Albany, A," *Teledyne Co., Albany, Oregon*, 1968.

[146] "Some thermal and mechanical properties of columbium alloy D-43," Aug. 1963.

[147] W. O. Gentry and A. B. Michael, "Properties of some columbium-rich alloys in the Cb-Ta-W-Zr System," in *High Temperature Materials*, New York: Interstate Publishers, 1963.

[148] J. B. Wachtman Jr, W. E. Tefft, D. G. Lam Jr, and C. S. Apstein, "Exponential temperature dependence of Young's modulus for several oxides," *Physical review*, vol. 122, no. 6, p. 1754, 1961.

[149] Y. P. Varshni, "Temperature dependence of the elastic constants," *Phys Rev B*, vol. 2, no. 10, p. 3952, 1970.

[150] J. R. Davis, *ASM specialty handbook: tool materials*. ASM international, 1995.

[151] G. Laplanche, P. Gadaud, L. Perrière, I. Guillot, and J. P. Couzinié, "Temperature dependence of elastic moduli in a refractory HfNbTaTiZr high-entropy alloy," *J Alloys Compd*, vol. 799, pp. 538–545, 2019, doi: https://doi.org/10.1016/j.jallcom.2019.05.322.

[152] D. C. Wallace and H. Callen, "Thermodynamics of crystals," *Am J Phys*, vol. 40, no. 11, pp. 1718–1719, 1972.

[153] F. D. Stacey and J. H. Hodgkinson, "Thermodynamics with the Grüneisen parameter: Fundamentals and applications to high pressure physics and geophysics," *Physics of the Earth and Planetary Interiors*, vol. 286, pp. 42–68, 2019.

[154] S. P. Kramynin and E. N. Akhmedov, "Equation of state and properties of Nb at high temperature and pressure," *Journal of Physics and Chemistry of Solids*, vol. 135, p. 109108, 2019.

[155] N. Soga, E. Schreiber, and O. L. Anderson, "Estimation of bulk modulus and sound velocities of oxides at very high temperatures," *J Geophys Res*, vol. 71, no. 22, pp. 5315–5320, 1966.

[156] Developed by Subcommittee: B09.04, "ASTM B962-17 Standard Test Methods for Density of Compacted or Sintered Powder Metallurgy (PM) Products Using Archimedes' Principle," in *Book of Standards Volume*, 5th ed., vol. 2, 2017.

[157] N. Philips, “Private Communication.” 2023.

[158] T. Balcerzak, K. Szałowski, and M. Jaščur, “A simple thermodynamic description of the combined Einstein and elastic models,” *Journal of Physics: Condensed Matter*, vol. 22, no. 42, p. 425401, 2010.

[159] Developed by Subcommittee: E01.06, “ASTM E1447-22 Standard Test Method for Determination of Hydrogen in Reactive Metals and Reactive Metal Alloys by Inert Gas Fusion with Detection by Thermal Conductivity or Infrared Spectrometry,” in *Book of Standards*, 5th ed., vol. 3, 2022.

[160] S. R. Agnew, F. Zeng, and G. R. Myneni, “Ultrasonic velocity and texture of high RRR niobium,” *Materiaux & Techniques*, vol. 91, no. 7-8–9, pp. 38–44, 2003.

[161] S. L. Dickerson and J. C. Gibeling, “Low cycle fatigue of niobium–zirconium and niobium–zirconium–carbon alloys,” *Materials Science and Engineering: A*, vol. 278, no. 1–2, pp. 121–134, 2000.

[162] M. Kopec, D. Kukla, X. Yuan, W. Rejmer, Z. L. Kowalewski, and C. Senderowski, “Aluminide thermal barrier coating for high temperature performance of MAR 247 nickel based superalloy,” *Coatings*, vol. 11, no. 1, p. 48, 2021.

[163] J. A. Wilson *et al.*, “Predicting the thermal expansion of body-centred cubic (BCC) high entropy alloys in the Mo–Nb–Ta–Ti–W system,” *Journal of Physics: Energy*, vol. 4, no. 3, p. 034002, 2022.

[164] E. Osei-Agyemang and G. Balasubramanian, “Effect of oxidation on the thermal expansion of a refractory multicomponent alloy,” *Philos Mag Lett*, vol. 101, no. 4, pp. 173–182, 2021.

[165] R. J. Farraro and R. B. McLellan, “High temperature elastic properties of polycrystalline niobium, tantalum, and vanadium,” *Metallurgical Transactions A*, vol. 10, pp. 1699–1702, 1979.

[166] H. Jiang, J. Yang, J. Dong, M. Zhang, Z. Yao, and X. Xie, “Stress Relaxation Behavior Comparison of Typical Nickel-Base Superalloys for Fasteners,” in *Proceedings of the 9th International Symposium on Superalloy 718 & Derivatives: Energy, Aerospace, and Industrial Applications*, Springer, 2018, pp. 789–804.

[167] Y. Wang, J. Dong, M. Zhang, and Z. Yao, "Stress relaxation behavior and mechanism of AEREX350 and Waspaloy superalloys," *Materials Science and Engineering: A*, vol. 678, pp. 10–22, 2016.

[168] D. C. Harris, *Materials for infrared windows and domes: properties and performance*, vol. 158. SPIE press, 1999.

[169] D. P. H. Hasselman, "Figures-of-merit for the thermal stress resistance of high-temperature brittle materials: a review," *Ceramurgia International*, vol. 4, no. 4, pp. 147–150, 1978.

[170] C. Belleau, W. L. Ehlers, and F. A. Hagen, "Materials review for improved automotive gas turbine engine," 1978.

[171] L. B. J. S. Center and M. L. Chazen, "Final Report. Study the Effects of Fuel Vortex Film Cooling on High Temperature Coating Durability," 1974.

[172] A. N. Behera and R. Kapoor, "Creep behaviour of Nb-1Zr and Nb-1Zr-0.1 C alloys from 800 to 1000° C at different stress levels," Bhabha Atomic Research Centre, 2021.

[173] Z. Dai *et al.*, "Study on the high temperature creep deformation and fracture behaviors of Inconel 625 deposited metal," *Materials Science and Engineering: A*, vol. 854, p. 143626, 2022.

[174] A. A. Tavassoli, "Metallic materials for the space shuttle," *The Aeronautical Journal*, vol. 76, no. 735, pp. 152–156, 1972.

[175] P. E. Kueser, "Research and Development Program on Magnetic, Electrical Conductor, Electrical Insulation, and Bore Seal Materials," *Rep. No. WAED*, vol. 64, 1965.

[176] I. Council, "Final Report of the ITER Engineering Design Activities," *IAEA EDA Document Series*, no. 21, 2001.

[177] A. Epishin *et al.*, "Investigation of elastic properties of the single-crystal nickel-base superalloy CMSX-4 in the temperature interval between room temperature and 1300 C," *Crystals (Basel)*, vol. 11, no. 2, p. 152, 2021.

[178] J. B. Lambert, "Refractory metals and alloys," 1990.

[179] Allegheny Technologies Incorporated, "Hafnium Alloy Addition (UNS R02001)," 2014.

[180] Allegheny Technologies Incorporated, "Reactor Grade Zirconium," 2015.

[181] S. Lampman, "Titanium and its alloys for biomedical implants," 2012.

[182] K. Harris, G. L. Erickson, and R. E. Schwer, "MAR-M247 derivations—CM247 LC DS alloy, CMSX single crystal alloys, properties and performance," *Superalloys*, vol. 1984, pp. 221–230, 1984.

[183] K. T. Regner, D. P. Sellan, Z. Su, C. H. Amon, A. J. H. McGaughey, and J. A. Malen, "Broadband phonon mean free path contributions to thermal conductivity measured using frequency domain thermoreflectance," *Nat Commun*, vol. 4, no. 1, p. 1640, 2013.

[184] R. B. Wilson, B. A. Apgar, L. W. Martin, and D. G. Cahill, "Thermoreflectance of metal transducers for optical pump-probe studies of thermal properties," *Opt Express*, vol. 20, no. 27, pp. 28829–28838, 2012.

[185] O. B. Wright, "Thickness and sound velocity measurement in thin transparent films with laser picosecond acoustics," *J Appl Phys*, vol. 71, no. 4, pp. 1617–1629, 1992.

[186] D. G. Cahill, K. Goodson, and A. Majumdar, "Thermometry and thermal transport in micro/nanoscale solid-state devices and structures," *J. Heat Transfer*, vol. 124, no. 2, pp. 223–241, 2002.

[187] W. S. Capinski and H. J. Maris, "Improved apparatus for picosecond pump-and-probe optical measurements," *Review of Scientific Instruments*, vol. 67, no. 8, pp. 2720–2726, 1996.

[188] R. M. Costescu, M. A. Wall, and D. G. Cahill, "Thermal conductance of epitaxial interfaces," *Phys Rev B*, vol. 67, no. 5, p. 054302, 2003.